UNIVERSITÉ DE MONTRÉAL

STUDY OF HUMAN CORTICAL MICROSTRUCTURE USING MAGNETIZATION TRANSFER AND T_2* MAPPING WITH APPLICATION IN MULTIPLE SCLEROSIS

GABRIEL MANGEAT

INSTITUT DE GÉNIE BIOMÉDICAL

ÉCOLE POLYTECHNIQUE DE MONTRÉAL

MÉMOIRE PRÉSENTÉ EN VUE DE L'OBTENTION

DU DIPLÔME DE MAÎTRISE ÈS SCIENCES APPLIQUÉES

(GÉNIE BIOMÉDICAL)

AVRIL 2016

UNIVERSITÉ DE MONTRÉAL

ÉCOLE POLYTECHNIQUE DE MONTRÉAL

Ce mémoire est intitulé:

STUDY OF HUMAN CORTICAL MICROSTRUCTURE USING MAGNETIZATION TRANSFER AND T_2* MAPPING WITH APPLICATION IN MULTIPLE SCLEROSIS

présenté par: MANGEAT Gabriel

en vue de l'obtention du diplôme de : Maîtrise ès sciences appliquées

a été dûment accepté par le jury d'examen constitué de :

M. STIKOV Nikola, Ph. D., président

M. COHEN-ADAD Julien, Ph. D., membre et directeur de recherche

Mme MAINERO Caterina, M. D., Ph. D., membre et codirectrice de recherche

M. BELLEC Pierre, Ph. D., membre

DEDICATION

À Jojoh, Aline et Thom!

ACKNOWLEDGEMENTS

First of all, I would like to thank my research supervisor Julien Cohen-Adad and co-supervisor Caterina Mainero. I have been realizing many times how lucky I was to have them as directors. Julien has a very appreciated perspective of work in research. He knows that the productivity of his students comes from their personal motivation and thus does a lot to make them love their work (schedule flexibility, research topic flexibility, encouraging to publish and participate to conferences, and so on). Caterina has an admirable sense of finding the pertinent questions to work on and the points to deepen. Her welcoming open-mindedness made it very agreeable to work with her. They both have a considerable experience in their field of research, which permitted me to learn how to conduct a research project in biomedical sciences. During these two years of master, they knew how to listen to me, discuss my problems, congrats me and assist me when needed. I feel to have significantly widen my knowledges and experience thanks to them.

I would like to acknowledge Nikola Stikov and Pierre Bellec, whom with it is always enjoyable to discuss various research ideas and who accepted to be part of the jury.

I thank my colleagues at NeuroPoly, Benjamin De Leener, Tanguy Duval, Ryan Topfer, Sarah Dupont, Simon Levy, Ariane Saliani, Grégoire Germain, Alexandru Foias, Nibardo Lopez Rios, Arul Venugopal, Manh-Tung Vuong and all the others, as well as Yves Goussard and Corentin Friedrich whom with I shared and I share an enjoyable and humorous everyday life at work. I wish not to forget all people who have left NeuroPoly at this day and whom with I had great work (and non-work) times.

Many thanks to my colleagues and collaborators at the Martinos Center, particularly Sindhuja Govindarajan, whom with I have started to collaborate more that 3 years ago, Elena Herranz, who experienced with me all the “beginner steps” of the Martinos, Céline Louapre, who namely explained me how to operate an MRI scanner, and many details about MS, Andrada Treaba, Costanza Gianni and Christian Langkammer whom with I had the chance to share research topics, of course, Tobias Granberg and Russell Ouellette, who maintain a gainful motivation to work and whom I really enjoy to share some projects. As well as my Lab-mates Nicolo Fuin, Reza Atefi, Stefano Pedemonte, David Izquierdo, Wei Tang and others. All these person went with me during my first steps in clinical research and significantly contributed to the experience I have acquired today.

I also want to thank some friends, namely Maël Richard, who never hesitated to explain me many medical details and who enjoyed to speak about my research project, as well as Gaëlle Seret and Jérémie Pilon whom with I discussed about some statistical issues.

My thanks are certainly going to my family, Johanna, Aline, Thomas, Frédérique and Frédéric who have been supporting me to continue my projects even though it implied to live 6000km away from them. Finally, my girlfriend Blanche Normand merits a special acknowledgement for supporting me before various deadlines, namely, the last two weeks.

Finally, I want to thanks the MEDITIS program (NSERC), the QBIN fellow program and the NeuroPoly laboratory for financial support.

RÉSUMÉ

Description du problème: La sclérose en plaques (SEP) est une maladie dévastatrice touchant plus de 100.000 personnes au Canada (MS Society of Canada). Les déficits fonctionnels engendrés par la maladie peuvent se traduire en troubles moteurs, cognitifs et sensoriels ayant un grand impact sur les activités sociales et professionnelles des patients. Le coût socio-économique de la SEP est colossal. Premièrement, la qualité de vie des patients ainsi que celle de leur familles peut se voir considérablement altérée. Deuxièmement, les traitements diminuant les effets handicapant de la SEP sont extrêmement dispendieux, leur coût annuel est estimé à plusieurs milliards de dollars au Canada (Karampampa et al. 2012) ainsi qu'aux USA (Hartung et al. 2015). De nos jours, la SEP ne se soigne pas et les détails de sa pathophysiologie restent obscures.

La SEP est une maladie du système nerveux central, chronique, inflammatoire et démyélinisante. Elle est caractérisé par la formation de lésions inflammatoires et démyélinisantes prenant place dans la moelle épinière et dans les matières blanche et grise du cerveau.

Bien que l'Imagerie par Résonance Magnétique (IRM) soit resté l'outil principal de diagnostic de SEP, les lésions observées dans la matière blanche ne corrélaient que très peu avec les déficits fonctionnels observés. Récemment, il à été montré que la démyélinisation de la matière grise est un meilleur indice de l'aggravement fonctionnel (Mainero et al. 2015). Cependant, les techniques d'IRM classiques sont difficilement utilisables pour l'imagerie du cortex, en effet, son épaisseur est seulement 2 à 4 mm et la résolution spatiale d'une IRM standard est de l'ordre de grandeur de 1 mm, ce qui n'est pas suffisant pour examiner précisément la pathologies corticales.

L'IRM à ultra-haut champ (7 Tesla) à été montré capable d'imager des détails microstructurels du cortex, grâce à un gain en résolution et en signal sur bruit. Récamment, il a été montré que la relaxation transverse (apellée T_2*) acquise à 7 Tesla est un marqueur sensible de la progression de la pathologie corticale des patients polyscléreux, notamment, de la démyélinisation corticale (Pitt et al. 2010; Mainero et al. 2015; Cohen-Adad et al. 2011). Cependant, des effets confondants réduisent la spécificité qu'a le contraste T_2* à quantifier la myéline (notamment, le contenu en fer, ou les vaisseaux sanguins) (Hwang et al. 2010; Lee et al. 2012). Une seconde mesure indépendante serait bénéfique pour augmenter la spécificité d'une potentielle estimation de quantitée de myéline. Le Ratio de Transfert de Magnétisation (MTR) à aussi été démontré sensible à la myéline dans le cortex (Derakhshan et al. 2014; Chen et al. 2013) et serait une excellent mesure

complémentaire car ses principes physiques sont différents de ceux de T_2*. Mentionnons qu'il n'est pas facile d'imager T_2* et MTR dans le cortex car le cortex est fin, très convolué et sa géométrie varie beaucoup entre individus.

Objectifs: Le premier objectif de cette étude est de combiner MTR et T_2* en utilisant des statistiques multivariées, dans le but d'augmenter la spécificité, de l'imagerie de myéline. Le deuxiéme objectif est d'évaluer les bénéfices d'une telle combinaison pour l'étude de la pathologie corticale de patients polyscléreux.

Méthode: Des sujets sains (témoins) et des patients polyscléreux ont été scannés à 7 Tesla et à 3 Tesla pour acquérire les données T_2* et MTR respectivement. Un modèle multivarié d'estimation de myéline à été développé et consiste à (i) normaliser les données T_2* et MTR (ii) extraire le signal commun aux deux contrastes en utilisant une analyse en composantes indépendantes (ICA). La dépendence à l'orientation du champ B_0 et l'épaisseur corticales ont aussi été calculé et incluses dans le modèle. Une comparaison avec des précédents résultats histologiques et des simulations ont permis de valider le gain obtenu en utilisant les métriques combinées. Un modéle Linéaire Général (GLM) à été utilisé pour évaluer les différences entre patients *vs* sujets témoins. L'âge, le genre et l'épaisseur corticale moyenne furent inclus comme régresseurs dans le GLM. Des estimations de la spécificité et sensibilité ont été faites sur certaines régions du cortex en utilisant des courbes ROC. Finalement, une étude laminaire de la pathologie diffuse fut conduite en utilisant des coupes à différendes profondeurs du cortex.

Résultats: De fortes corrélations ont été observées entre MTR et T_2*, dans le cortex entier ($r = 0.76$, $p = 10^{-16}$), suggérant que les deux métriques soit en partie influancées par la même source de contraste, supposée étant la myéline. Les valeurs moyennes du MTR et T_2* dans le cortex sont respectivements de 31.0 +/− 0.3% et 32.1 +/− 1.4 ms. La carte de myéline résultant de la combinaison a montré une tendance similaire aux travaux histologiques de quantification de myéline ($r = 0.77$, $p = 0.01$). Des différences significatives inter hémisphères ont été détéctées dans le cortex moteur primaire, le cortex posterieur singulier et le cortex visuel ($p=0.05$). Les GLM ont révélés des régions de démyélinisation significatives dans les cortexes moteurs, visuels, auditifs et somato-sensoriels ($p<0.05$). Ces différences se sont montrées statistiquement significatives quand les cartes de myélines combinées étaient utilisées, alors qu'aucune différence significative ne fut détectée en utilisant les autres métriques seules (c.à.d MTR et T_2*). De plus, les cartes

combinées ont été montrées capables de révéler des aires de démyélinisation dans les cortexes de jeunes patients polyscléreux (diagnostiqués in y a moins de 3 ans).

Discussion: Cette étude à démontré que les modalitées MTR et T_2* sont fortement corrélées dans le cortex. La combinaison de MTR, T_2*, épaisseur corticale orientation par rapport à B_0 est un moyen efficace pour étudier la myélo-architecture corticale avec plus de spécificité qu'en utilisant seulement T_2* ou MTR. Ceci fournit un outil puissant pour l'étude des fines variations de myéline survenant dans le cortex des patients polyscléreux. Les premières applications de la méthode supportent le fait que la démyélinisation corticale est un évènement survenant tôt dans la sclérose en plaques, même en présence d'un handicap neurologique léger.

Impacte: La quantification non-invasive de la pathologie corticale de la SEP est la pièce manquante du puzzle pathophysiologie de la SEP. Comprendre les liens entre la pathologie de la matière blanche, la pathologie de la matière grise et les déficits fonctionnels peut i) aider à comprendre des détails fins des mécanismes de la SEP ii) aider à concevoir et cibler des futures traitements.

ABSTRACT

Problem description: Multiple Sclerosis (MS) is a devastating disease affecting around 100,000 people in Canada (MS Society of Canada). The functional deficits resulting from the disease include motor, cognitive and somatic troubles, affecting the social and professional activities of MS patients. The socio-economic cost of MS is colossal. Firstly, life quality of MS patients and those of their family members can be drastically hampered. Secondly, existing treatments that reduce handicapping effects of MS are expensive, with an annual cost estimated in billions of dollars in Canada (Karampampa et al. 2012) and in the USA (Hartung et al. 2015). To date, MS is not curable and its pathophysiological mechanisms are still obscure.

MS is known to be a chronic, inflammatory, demyelinating disease of the central nervous system. It is characterized by the formation of inflammatory and demyelinating lesions in the spinal cord and in the brain's white and gray matters.

While Magnetic Resonance Imaging (MRI) has been the main tool for diagnosing MS, correlations of white matter lesions with functional deficits remain poor. Recently, it was shown that grey matter demyelination provides a more specific assessment of functional worsening (Mainero et al. 2015). However, it is difficult to image the grey matter with standard MRI methods because the cortex is only 2-4 mm thick and the spatial resolution of standard MRI system is on the order of 1 mm, which is not sufficient for proper examination of cortical pathology.

Ultra-high field MRI (7 Tesla) was shown to reveal microstructural features thanks to an increase in signal to noise ratio and spatial resolution. Recently, transverse relaxation (characterized by a time constant: T_2*) at 7 Tesla was shown to be a sensitive marker of pathology and disease progression associated with demyelination in the cortex of MS patients (Pitt et al. 2010; Mainero et al. 2015; Cohen-Adad et al. 2011). However, several confounds hamper the specificity of T_2* measures (iron content, blood vessels) (Hwang et al. 2010; Lee et al. 2012). An independent measure would increase the specificity to the myelin content. Magnetization Transfer Ratio (MTR) imaging has been shown to be sensitive to myelin content (Derakhshan et al. 2014; Chen et al. 2013) and thus would be an excellent complementary measure because its underlying contrast mechanisms are different than that from T_2*. However, mapping MTR and T_2* in the cortex is challenging because the cortical ribbon is thin, highly convoluted and its geometry varies across individuals.

Goals: The first goal of this study was to combine MTR and T_2* using multivariate statistics in order to gain insights into cortical myelin content. The second goal was to assess the benefits of the combination to study the cortical disease progression in various groups of MS patients.

Method: Healthy Control (HC) subjects and MS patients were scanned at 7 T and at 3 T to obtain T_2* and MTR data, respectively. A multivariate myelin estimation model was developed, and consists of (i) normalizing T_2* and MTR values and (ii) extracting their shared information using independent component analysis (ICA). B_0 orientation dependence and cortical thickness were also computed and included in the model. Comparisons with previous histological work and simulated MRI data were used to validate the improvement given by the combined metrics. General Linear Models (GLM) were used to assess group differences in MS versus HC. Age, gender and mean cortical thickness were included as regressing factors. Sometimes, specificity/sensitivity assessment using Receiver Operating Characteristics (ROC) curves was performed on various cortical areas. Finally, laminar study of the diffuse pathology was achieved in a group of early MS patients by using samplings at diverse cortical depth.

Results: High correlations were found between MTR and T_2* in the whole cortex ($r = 0.76$, $p = 10^{-16}$), suggesting that both metrics are partly driven by a common source of contrast, here assumed to be the myelin. Average MTR and T_2* were respectively 31.0 +/− 0.3% and 32.1 +/− 1.4 ms. Resulting combined map showed similar trends to that from histological work stained for myelin ($r = 0.77$, $p = 0.01$). Significant right-left differences were detected in the primary motor cortex, the posterior cingulate cortex and the visual cortex ($p = 0.05$). General linear models have revealed regions of significant cortical demyelination, namely in the motor, visual, auditory and somatosensory cortices ($p<0.05$). These differences were statistically significant while using the combined myelin map, although no significant difference was detected when using others matrices (i.e. MTR and T_2*) taken alone. Moreover, the combined myelin map was shown to detect areas of diffuse demyelination in the cortices of early MS patients ($p<0.05$, disease duration < 3 years).

Discussion: This research demonstrated that MTR and T_2* are highly correlated in the cortex. The combination of MTR, T_2*, cortical thickness and B_0 orientation may be a useful means to study cortical myeloarchitecture with more specificity than taking each contrast separately. This provides a powerful tool to study slight and early cortical demyelination in MS patients. Pioneer

applications of the method support subpial demyelination as an early event in MS, even in the presence of mild neurological disability.

Impact: Non-invasive quantification of the MS cortical pathology is the missing piece of the MS pathophysiology puzzle. Effectively relating WM pathology, GM pathology and functional worsening, will i) help to understand fine MS mechanism ii) help to design and target future MS treatments.

TABLE OF CONTENTS

LIST OF TABLES

LIST OF FIGURES

LIST OF SYMBOLS AND ABBREVIATIONS

ASA	American Statistician Association
BBB	Blood-Brain Barrier
CARS	Coherent Anti-Stokes Raman Scattering
CL	Cortical Lesion
CLT	Central Limit Theorem
CNS	Central Nervous System
CSF	Cerebro-Spinal Fluid
CT	Cortical Thickness
DIR	Double Inversion Recovery
DSI	Diffusion Spectrum Imaging
DTI	Diffusion Tensor Imaging
ECTRIMS	European Committee for Treatment and Research in Multiple Sclerosis
FLAIR	FLuid-Attenuated Inversion Recovery
GM	Gray Matter
HC	Healthy Control
IC	Independent Component
ICA	Independent Component Analysis
IF	Impact Factor
ISMRM	International Society for Magnetic Resonance in Medicine
MMEM	Multivariate Myelin-Estimation Model
MRI	Magnetic Resonance Imaging
MS	Multiple Sclerosis
MT	Magnetization Transfer

MTR	Magnetization Transfer Ratio
NAGM	Normal Appearing Grey Matter
NAWM	Normal Appearing White Matter
NMR	Nuclear Magnetic Resonance
PCA	Principal Component Analysis
PET	Proton Emission Tomography
PNS	Peripheric Nervous System
qPD	quantitative Proton Density
qT_1	quantitative T_1
qT_2	quantitative T_2
RD	Radial Diffusivity
RRMS	Relapsing-Remitting Multiple Sclerosis
SBA	Surface-Based Analysis
SD	Standard Deviation
SNR	Signal to Noise Ratio
SPGR	SPoiled Gradient Recalled imaging
SPMS	Secondary Progressive Multiple Sclerosis
TE	Echo Time
TR	Repetition Time
WM	White Matter

LIST OF APPENDICES

CHAPTER 1 INTRODUCTION

Multiple Sclerosis (MS) is a neurodegenerative disease of the central nervous system (CNS) affecting around 100,000 people in Canada (MS Society of Canada). MS is the second cause of handicap in young adults. The functional deficits resulting from the disease include motor, cognitive and somatic troubles, affecting the social and professional activities of MS patients. The socio-economic cost of MS is colossal. Firstly, life quality of MS patients and those of their family members can be drastically hampered, they can for example lose their job or not anymore be able to live autonomously. Secondly, existing treatments that reduce handicapping effects of MS are expensive, with an annual cost estimated in billions of dollars in Canada (Karampampa et al. 2012) and in the USA (Hartung et al. 2015). MS is thus a colossal socio-economic concern for the society. To date, MS is not curable and its pathophysiological mechanisms are still obscure.

MS is known to be an inflammatory and demyelinating disease. Inflammation comes from an immune reaction of the nervous system against itself. This mechanism classifies MS with the autoimmune diseases. Moreover, MS attacks and disrupts the protective layer of axons, called **myelin**. Myelin is essential for the transmission of action potentials in axons, thus amongst neurons. Without myelin, information travels slower and bare axons become vulnerable to external attacks. Unfortunately, loss or degeneration of axons are common outcomes of MS, making it a so-called neurodegenerative disease.

MS patients can present various kind of symptoms. Some patients can keep a good quality of life and a perfect social integrity during their entire life, while others will quickly lose their cognitive abilities and social skills (Lhermitte 1924). One difficulty that clinicians and researchers developing treatment face is that MS is difficult to diagnose. In addition to a neurological examination, Magnetic Resonance Imaging (MRI) is used to detect tissue damages in the brain (and spinal cord). Because MRI can detect *in-vivo* a variety of MS features in the brain, such as inflammations, oedemas or demyelinating lesions, it has become the principal tool for the study of the disease progression, pathophysiology and treatment assessment.

Until the beginning of 2000s, MS has been primarily known as a white matter disease. However, evidence of diffuse gray matter (GM) pathology has been reported since the nineteenth century (Wyllys Taylor 1894; Brownell & Hughes 1962). This biased view has been partly

influenced by the difficulty in detecting MS lesions in the cortex. Moreover, the damaged WM areas and the observed functional deficits were not correlating well, letting doubts in the comprehension of the pathology. Eventually, progress in MRI technology (including superconductors) allowed to increase the MRI's magnetic field, permitting to gain resolution and sensitivity in MR images. Notably, 7 Tesla MRI devices led to a significant breakthrough in the study of the progression of MS in the cortical gray matter (also called cerebral cortex). Researchers not only discovered that MS pathology was present in the cortex, but studies found that the cortical pathology was at least as important as in the WM (Kidd et al. 1999; Peterson et al. 2001). Thus, new questions are raised, such as the potential interplay between GM and WM pathology, the role of GM demyelinating lesion or their correlation with functional deficits.

The cerebral cortex is a complex and still poorly-known part of the human brain, where the neuronal fibers converge and inter-connect. Despite its thin structure (2-4mm thick and 1.1-1.5% of the total brain volume), it contains more than 100 billion neurons and 100 trillion neural connexions. The brain cortex is involved in the Human intelligence, consciousness, senses perceptions, memory, motor functions, etc.. Thus, it is not surprising that cortical damages, such as cortical demyelinating lesions can seriously impact nervous functions.

The use of MRI to study myelo-architectural structures *in-vivo* (and MS damages) of the cortex is still a research practice. Indeed, cortical studies are challenging because of the thin aspect of the cortex, its high level of convolution, the low MR signal caused by a limited spatial resolution and the high structural variability across individuals. Moreover, even when using a cutting edge MRI device, there are only a few MR modalities (sometimes called metrics) capable of producing a good signal and contrast in the cortex.

Recently, T_2* acquired with 7 Tesla scanners was shown to provide quantitative markers of the pathology progression and the myelin organisation in the cortex (Deistung et al. 2013; Cohen-Adad et al. 2011; Mainero et al. 2015; Li et al. 2015). Although there are several aspects supporting a significant role of cyto/myelo- architecture in T_2* relaxation in the brain, several confounds exist that reduce the specificity of T_2* as a marker of myelin, such as the tissues iron level, B_0 field inhomogeneities or tissue orientation with respect to B_0 (Lee et al. 2012; Lee et al. 2011; Cohen-Adad et al. 2012; Stüber et al. 2014; Spees et al. 2001; Li et al. 1998).

An independent measure would increase the specificity to myelin. Magnetisation Transfer (MT) imaging has been shown to be sensitive to myelin content in WM (Schmierer et al. 2004; Schmierer et al. 2007) & GM (Chen et al. 2013; Derakhshan et al. 2014) and thus would be an excellent complementary measure because its underlying contrast mechanisms are substantially different from T_2*. The MT effect results from the interaction between water protons and protons associated with macromolecules. Macromolecules, such as myelin can be indirectly imaged by using an off-resonance pulse that will saturate their spins in magnetisation and lower their contribution in an ensuing MR image (Henkelman et al. 2001; Pike Bruce 1996). The term *transfer* comes from the fact that macromolecules will transfer their magnetisation to the surrounding water molecules, and this mechanism of transfer is the principal source of MT contrast.

The goal of my master's thesis was to acquire both MR metrics (MTR and T_2*) in the cortex of subjects and to combine them by using multivariate statistics in order to obtain a metric more specific to the cortical myelin content. The usefulness of such a metric being to study the cortical myeloarchitecture of the Human brain and the progression of cortical MS pathology.

My research hypotheses were: **H1)** The combination of T_2* and MTR using multivariate statistics will provide a sensitive and specific mapping of myelin content, as validated using previous histology work in humans (Braitenberg 1962; Geyer et al. 2011). **H2)** The combined metrics corrected for confounds will show changes in the cortex of MS patients versus healthy controls. **H3)** These changes will be correlated to functional deficits in MS patients, as assessed using clinical scores.

1.1 Publications

During my two years of Master's study, I've been working on the above hypotheses. As a result, I have published one scientific article and one conference poster about the validation of H1 (Mangeat et al. 2014; Mangeat, et al. 2015) as well as one conference presentation and one conference poster about the validation of H2 and H3 (Mangeat et al. 2015; G. Mangeat, et al. 2015; Mangeat et al. 2016). More explicitly, these publications were:

- Mangeat *et. al.*, 2015, *Multivariate combination of magnetization transfer,* T_2* *and* B_0 *orientation to study the myelo-architecture of the in vivo human cortex. Neuroimage* 119, 89–102.

- Mangeat *et. al.,* 2014, *Comparison between 7T* T_2* *and 3T MTR in the in vivo human cortex,* in: *ISMRM,* poster #1783.
- Mangeat *et. al.,* 2015, *Multivariate combination of magnetization transfer ratio and quantitative* T_2* *to detect subpial demyelination in multiple sclerosis,* in: *ISMRM,* presentation #0823.
- Mangeat *et. al.,* 2015, *Multivariate combination of quantitative* T_2* *and* T_1 *at 7T MRI detects in vivo subpial demyelination in the early stages of MS,* in: *Mult Scler.* Presented at the *ECTRIMS,* p. 485.
- Mangeat *et. al.,* 2016, *Association between cortical demyelination and structural connectomics in early multiple sclerosis, in: ISMRM,* presentation #237.

1.2 Memoire organization

This present mémoire is divided in eight chapters:

Chapter 1 is the present introduction.

Chapter 2 is the literature review. This review first introduces the physiology of a neuron with the emphasis on the axon composition and the key role played by myelin in the transmission of actions potentials. Then, it zooms out to present the laminar organisation of the Human cortex, namely, the various cortical layers, their typical neural composition and the differents techniques used to image the *ex-vivo* cyto- and myelo-architecture of the Human cortex. It zooms out again, and introduces the whole Human cortex, its various parcellations in cortical areas and the advantages of previous parcellation works. Then, challenges in creating and using cortical parcellations are pointed out. Next, Multiple Sclerosis is introduced. Elements of the pathophysiology are explained, and the various MRI techniques to study the disease features and progression are summarized. Then, the focus is put on cortical MS features and the cutting edge MRI methods to image them *in-vivo*. The second part of the review introduces the concept of nuclear resonance imaging and its evolutions leading to the concept of quantitative imaging (qMRI). Ensuingly, particular attention is given to the two quantitative MRI modalities MTR and T_2*, their contrast mechanism, their sources of signal and their abilities to image cortical myelin content. Thereafter, the rationale behind combining MTR and T_2* is presented. The third part of the review is about mathematics. It presents the concept of the Independent Component Analysis

(ICA) decomposition and compares diverse algorithms available in the literature, in term of computation time, robustness and accuracy. Finally, the Mathematics review outlines the problem of groups statistics when using normalized data and derives a solution based on relative distribution parameters.

Chapter 3 gives an overview of the research methodology followed in this mémoire. It shows the scientific publications resulting from this mémoire and explains the scientific approach that links these publications amongst them.

Chapter 4 presents the main scientific publication of this work: *Multivariate combination of magnetization transfer,* T_2* *and* B_0 *orientation to study the myelo-architecture of the in vivo human cortex,* article published in the scientific journal *NeuroImage* on October 1st, 2015.

Chapter 5 gives supplementary information about the methodology behind the choice of combining MTR and T_2*. It presents *Comparison between 7T* T_2* *and 3T MTR in the in vivo human cortex,* which is a scientific poster presented in may 2014 at the conference ISMRM (*International Society for Magnetic Resonance in Medicine*). This work explored the feasibility to combine MTR and T_2* metrics in the human cortex.

Chapter 6 discusses the applications of the combination method to study cortical MS pathology. It summarises the study: *Multivariate combination of magnetization transfer ratio and quantitative* T_2* *to detect subpial demyelination in multiple sclerosis,* which is an oral presentation presented in june 2015 at the conference ISMRM, as well as the study *Multivariate combination of quantitative* T_2* *and* T_1 *at 7T MRI detects in vivo subpial demyelination in the early stages of MS,* which is a scientific poster presented in october 2015 at the conference ECTRIMS (*European Committee for Treatment and Research in Multiple Sclerosis*).

Chapter 7 is a general discussion about the performed studies. It relates the limitations and the potential weakness of the methods and gives the details of potential improvements relevant for researchers interested in this work.

Chapter 8 concludes this Master's thesis and states examples of future work relevant to the study of cortical MS pathology using MRI.

CHAPTER 2 LITTERATURE REVIEW

2.1 Medical review

2.1.1 Physiological bases

2.1.1.1 Physiology of the neuron

Neurons are the basic functional units of both the central and the peripheral nervous systems. They are the cells responsible for the transmission of nervous information. Neurons operate by generating electrical signals (ionic currents) that move from one part of the cell to neighboring cells. Depending on the amount and amplitude of stimulations received by neighboring cells, a neuron will decide whether it will transmit the signal, called **action potential**, or not. This basic principle drives the whole nervous system and leads, for example, to **memory**, **cognition** or **consciousness**. This section will cover the anatomy of the neuron, the principle of circulation of information and the key role played by the molecules of myelin.

2.1.1.1.1 Anatomy

Neurons appear in a wide variety of sizes and shapes, but all share **dendrites** and **axons terminals**, used to receive and transmit the nervous information, respectively .Moreover, all neurons have a cell body, called **soma**, and a *wiring system,* called **axon**, that convey the electrical information through the nervous system. **Figure 2-1 A** shows a representation of a neuron and its basic components as well as the shape of a neuron observed through a microscope. As in other types of cells, a neuron contains a nucleus in its cell body (or soma) that enclose the genetic information as well as ribosomes and machinery necessary for protein synthesis. The **dendrites** are a series of highly branched outgrowths linked to the soma. their role is to receive the inputs from others neurons. On average a neuron has 1,000 dendrites, but some neurons may have as many as 400,000 dendrites. The number of dendrites increase the cell capacity to receive signal from many afferent neurons. The components that actually transmit the information are the **axon terminals**. Under the command of an action potential, axons terminals are releasing the neurotransmitters through the **synaptic terminals**, that reach another neuron or an excitatory cell. Finally, the part of the neuron which links the soma with the axons terminals is a kind of organic wire called **axon.** An axon can be some micrometers to many centimeters long. Axons are

encompassed by sheaths of **myelin**, a fatty white substance produced by a cell called **oligodendrocyte, Figure 2-1 B**. Axons transmit the actions potentials from the cell body to the axons terminals using **ionic currents**. To understand the key role played by myelin in the conveyance of action potentials, it is important to understand first the principles of membrane ionic currents.

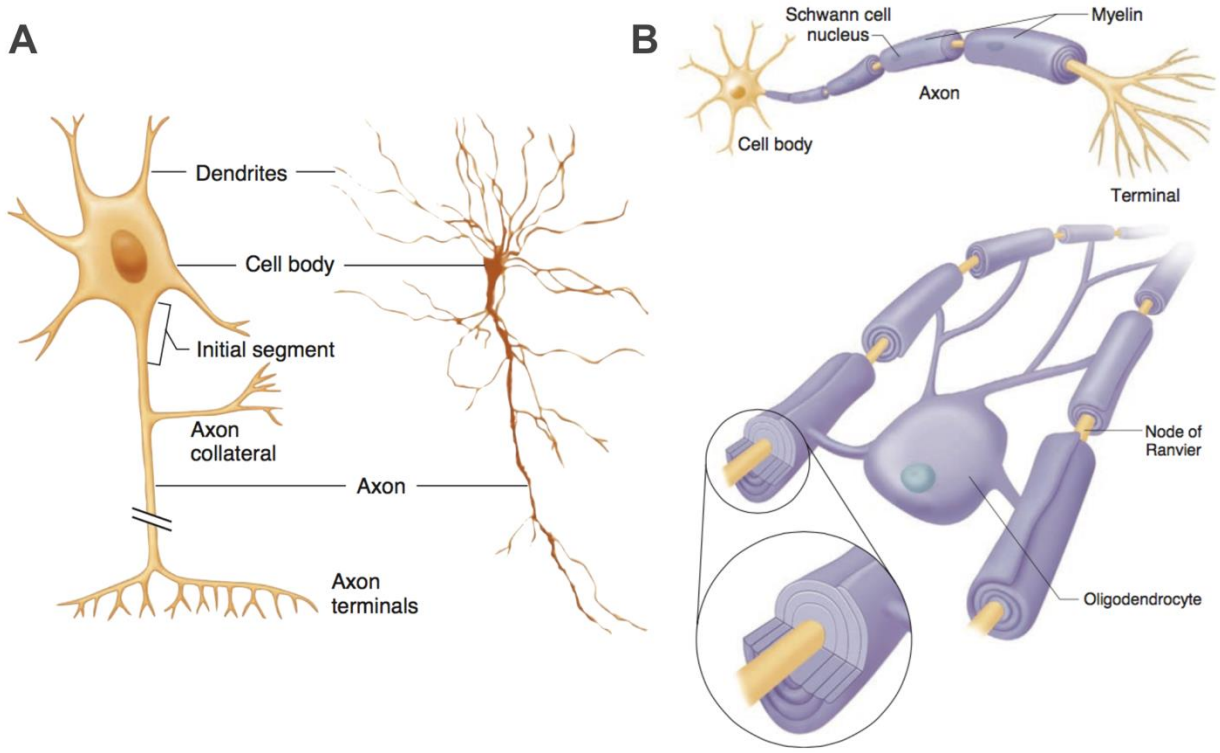

Figure 2-1, Adapted from (Widmaier et al. 2013, Fig. 6-1 & 6-2). Representation of a neuron and its basic components as well as the shape of a neuron observed through a microscope (A). Representations of axons encompassed by macromolecules of myelin. Myelin is produced by oligodendrocytes cells in the CNS and by Schwann cell in the Peripheric Nervous System (PNS). The portion of bare axon in between two myelin blocks is called *Node of Ranvier*.

The two ions that are playing the main role in neural ionic current are K+ (*Potassium*) and Na+ (*Sodium*). At resting state K+ ions are found in high concentration in the **intracellular** fluid (~150 [mmol/L]), whereas they are found in low concentration in the **extracellular** fluid (~5 [mmol/L]). Inversely, Na+ ions are present in low concentration in the intracellular fluid (~15 [mmol/L]), but are found in high concentration in the extracellular fluid (~145 [mmol/L]).

Moreover, the cell membrane is equipped with **channels** which act like a door and which are specific to one kind of ion, for example the **potassium channel** and the **sodium channel**. When these channels are open, the gradient in concentration is creating a **diffusion flux** through the membrane. For example, if the sodium channels open, a flux of Na+ ions will enter the cell because their concentration is lower inside the cell.

In addition to the diffusion gradient, the **electrical force** plays a role on ions flux. Indeed, some anions such as Cl- keeps the extracellular fluid neutral, in term of electric charge, while some negatively charged proteins keep the intracellular fluid negatively charged. At rest, the typical potential difference between intra- and extra- cellular fluids is -70 [mV]. This negative potential polarises the cell membrane and thus contributes to retain K+ ions inside the cell and to attract Na+ ions inside the cell as well. To maintain the gradient in concentration, **Na+/K+ -ATPase** pumps use energy contain in ATP to pump K+ inside the cell and pump Na+ outside. **Figure 2-2, A** represents the polarisation of the cell membrane, while **Figure 2-2 B** summarises the two forces driving K+ and Na+ flux occurring when channels are open.

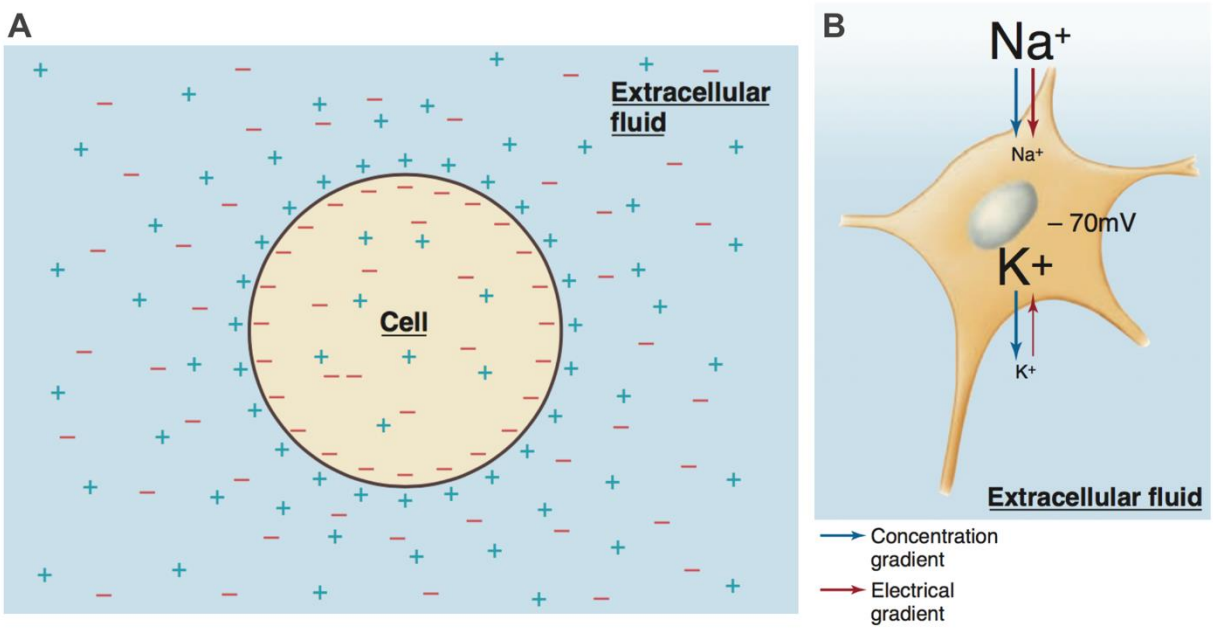

Figure 2-2, Adapted from (Widmaier et al. 2013, Fig. 6-9 & 6-12). Polarisation of the cell membrane, anions such as Cl- keeps the extracellular fluid neutral, in term of electric charge, while some negatively charged proteins keep the intracellular fluid negatively charged. At rest, the typical potential difference between intra- and extra- cellular fluids is -70 [mV] **(A)**. Gradient in ions

concentration is creating a diffusion flux through the membrane. For example, if the sodium channels open, a flux of Na+ ions will enter the cell because their concentration is lower inside the cell. To maintain the gradient in concentration, Na+/K+ -ATPase pumps use energy contain in ATP to pump K+ inside the cell and pump Na+ outside **(B).**

To understand how neurons transmit action potentials, it is necessary to understand how ionic channels open and what happens with the membrane potential when they open. Potassium and sodium channels are triggered by a variation of the membrane potential, they are called **voltage-gated channels**. Indeed, at rest, the membrane potential is -70 [mV], but if an external stimulus, such as the action of a synapse, changes this membrane potential to approximately -60 [mV], potassium and sodium channels will briefly open. Sodium channels open very briefly (~1 [ms]) whereas potassium channels open for a longer time (~4 [ms]). Moreover, the potassium channels opening is a bit delayed compared to sodium channels opening. **Figure 2-3 A** shows the variations of the membrane potential resulting of all these ion fluxes. while **Figure 2-3 B** shows the variations of membrane permeability after an action potential for both K+ and Na+.

To summarize, here are the steps taking place during an action potential: 1) The membrane is at its steady potential -70 [mV]. 2) an external depolarizing stimulus bring the membrane potential to the threshold potential. 3) Na+ channels open, thus Na+ ions enter rapidly (because both electrical force and and concentration gradient influence Na+ to enter the cell). This results in a fast depolarisation of the membrane (up to 30 [mV]). 4) Na+ channels are closing while K+ channels open. 5) K+ ions are going out of the cell, which has for effect to repolarizes the membrane. 6) A hyper-polarisation occurs because K+ channels close slowly and too much K+ is left out. 7) back to the steady potential.

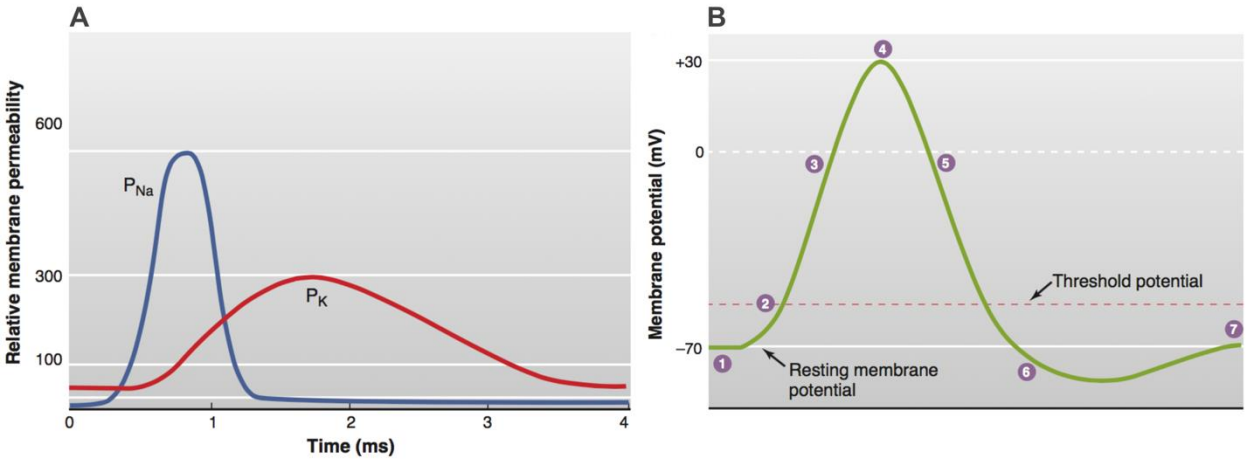

Figure 2-3, Adapted from (Widmaier et al. 2013 Fig. 6-19). Variations of the membrane potential resulting of K+ and Na+ fluxes **(A)**. Variations of membrane permeability after an action potential for both K+ and Na+ **(B)**. Steps 1-7 represents: 1) The membrane is at its steady potential -70 [mV]. 2) an external depolarizing stimulus brings the membrane potential to the threshold potential. 3) Na+ channels open, thus Na+ ions enter rapidly. This results in a fast depolarisation of the membrane (up to 30 [mV]). 4) Na+ channels close while K+ channels open. 5) K+ ions exit the cell, inducing repolarization of the membrane. 6) A hyper-polarisation occurs because K+ channels close slowly and too much K+ is left out. 7) back to the steady potential.

2.1.1.1.2 Circulation of information

After an action potential, the membrane is **refractory** for 2-4 [ms], meaning that it can not be re-excited while the channels are closing and the pumps are bringing K+ and Na+ concentrations back at their resting values. This refractory period turns out to be essential for the directional transmission of information. **Figure 2-4** illustrates the principle of the propagation of the membrane depolarisation. i) The local depolarisation of the membrane by an action potential will trigger the neighbouring membrane to depolarise itself (because K+ and Na+ channels are voltage-gated channels sensitive to a neighboring depolarisation). ii) the "already depolarised" membrane is refractory so that only the resting membrane will be depolarised and so on. This is the principle that causes **actions potential propagation along axons**.

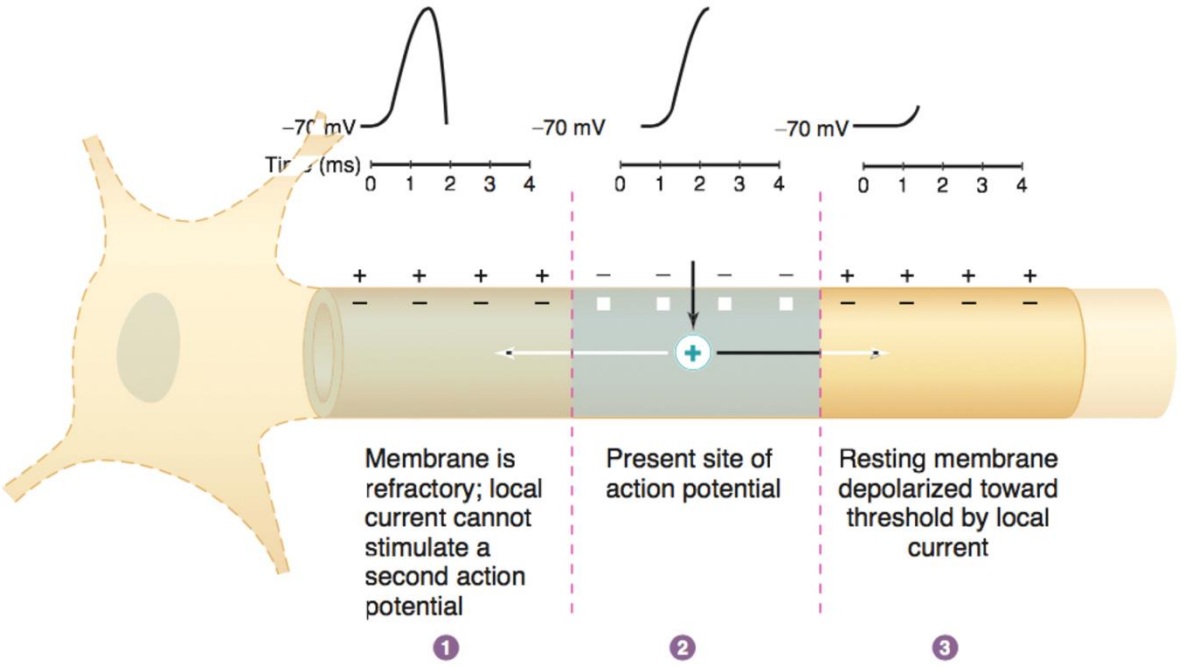

Figure 2-4**,** Adapted from (Widmaier et al. 2013 Fig. 6-22). Principle of the propagation of the membrane depolarisation. i) The local depolarisation of the membrane by an action potential will trigger the neighbouring membrane to depolarise itself (because K+ and Na+ channels are voltage-gated channels sensitive to a neighboring depolarisation). ii) the "already depolarised" membrane is refractory so that only the resting membrane will be depolarised and so on.

2.1.1.1.3 The key role of myelin

The velocity with which an action potential propagates along a membrane depends on fiber diameter and whether or not the fiber is surrounded by **myelin sheaths** (such fibers are called: **myelinated fibers**). The larger the fiber diameter, the faster the action potential propagates. Indeed, a large fiber offers less resistance to local current, so that more ions will flow in a given time, bringing adjacent regions of the membrane to threshold faster. (Widmaier et al. 2013)

Moreover, the larger part of axons are myelinated. Myelin acts as an insulator that decreases the membrane permeability to ions. Because there is less flux of charge across the myelin, a local current can spread farther along an axon. Furthermore, the concentration of voltage-gated sodium channels in the myelinated region of axons is low. Therefore, action potentials occur only at the **nodes of Ranvier**, where the myelin coating is interrupted and the concentration of voltage-gated

sodium channels is high, **Figure 2-5**. As, action potentials jump from one node to the next as they propagate along a myelinated fiber, such propagation is called **saltatory conduction**.

Propagation via saltatory conduction is faster than propagation in non-myelinated fibers of the same axon diameter because less charge leaks out through the myelin-covered sections of the membrane. More charge arrives at the node adjacent to the active node, and an action potential is generated there sooner than if the myelin were not present. Moreover, because ions cross the membrane only at the nodes of Ranvier, the membrane pumps need to restore fewer ions. Myelinated axons are therefore metabolically more efficient than unmyelinated ones. In this way, myelin adds speed, reduces metabolic cost, and saves room in the nervous system because the axons can be thinner.

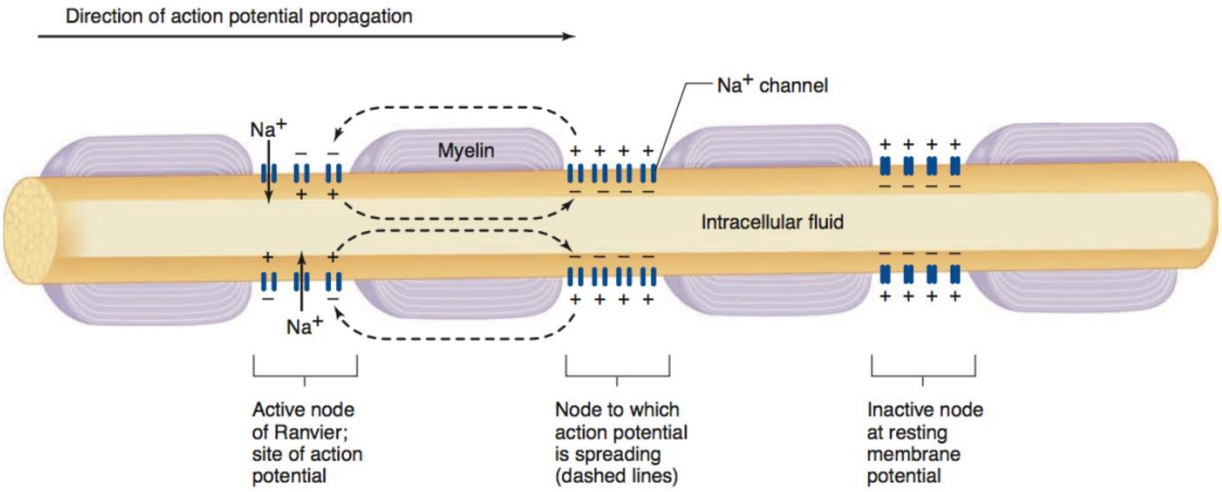

Figure 2-5**,** Adapted from (Widmaier et al. 2013 Fig. 6-23). Representation of the saltatory conduction. Concentration of voltage-gated sodium channels is low in the myelinated regions. Action potentials occur only at the **nodes of Ranvier**, where axon is bare and the concentration of voltage-gated sodium channels is high. Action potentials thus "jump" from one node to the next as they propagate along a myelinated fiber.

2.1.1.2 Physiology of the Human cortex

2.1.1.2.1 The cerebral cortex

The cerebral cortex is the outer layer of the brain neural tissue, **Figure 2-6**. Is is often called cerebral Grey Matter (GM) because it appears darker than the inner neural tissue called White Matter (WM). Although GM is commonly used as a synonymous of cerebral cortex, it is important to notice that the term GM actually includes cerebral cortex along with others neural tissues such as the thalamus or spinal grey matter. Basically, GM can be used to design any neural tissue that includes neurons bodies and neurites. In this review GM will refer to the cerebral cortex.

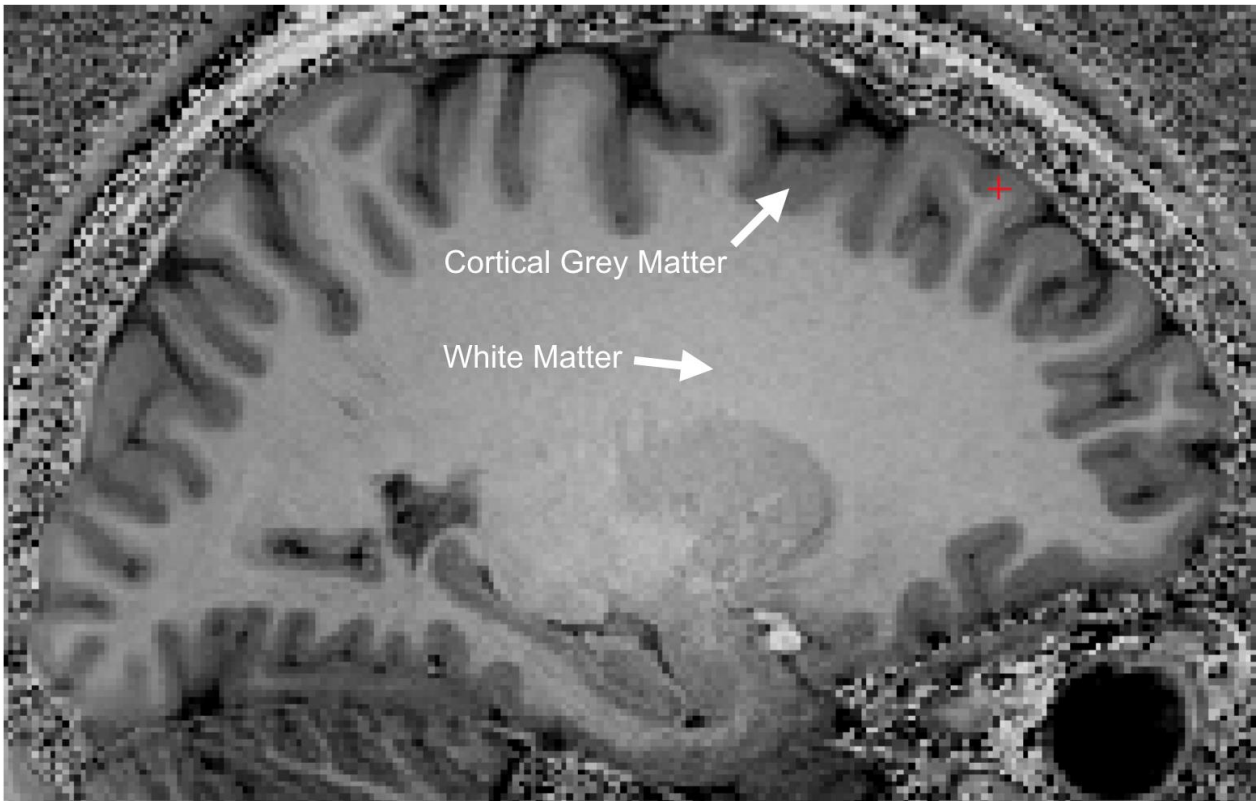

Figure 2-6, MRI T_1-w image, sagittal view. The cortical grey matter (GM) is the outer (dark) layer of the brain, while the inside white region is the white matter (WM).

2.1.1.2.2 Cortical composition: neurons and glial cells

In humans, the cerebral cortex is 2 to 4 mm thick. It contains the cell bodies and the dendrites of the cerebral neurons whereas the axons are found in the cerebral white matter. Moreover, neurons

account for only 28% of the cells in the cerebral cortex (Azevedo et al. 2009), the 72% remaning cells are the glial cells, also called neuroglial cells (glia = glue). Glial cells surround the soma, axons and dendrites, one of their role is to provide them with metabolic support. The main glial cells are the **Astrocytes, Microglia, Ependymal cells** and **Oligodendrocytes**, **Figure 2-7**. The **Astrocytes** help regulate the composition of the extracellular fluid and sustain the neurons metabolically, for example by providing glucose and removing ammonia. Astrocytes also stimulate the formation of tight junctions between the wall cells of the capillaries in order to form the so-called **blood-brain barrier** (BBB), which prevents toxins and other undesired substances to enter the brain. **Microglia** are macrophage cells that perform immune function in the cortex and in the central nervous system in general. **Ependymal cells** form the boundaries between the brain matter and the cerebrospinal fluid. Lastly, the **Oligodendrocytes** produce the myelin sheaths that cover the axons. As we saw in the precedent section, the myelin sheaths are essentials for the propagation on the actions potentials. Therefore, death of oligodendrocytes in a region of the cortex leads to a demyelination of axons that hampers the afferent communications between neurons. The demyelination processes and effects will be discussed in more details in the next section. So far, glial cells are known to play a secondary role in the information processing but they are critical for the synergy of the central nervous system. Moreover, as well as neurons, they are contributing to the MRI signal, thus, a change in the neuroglial composition implies a change in an MRI image.

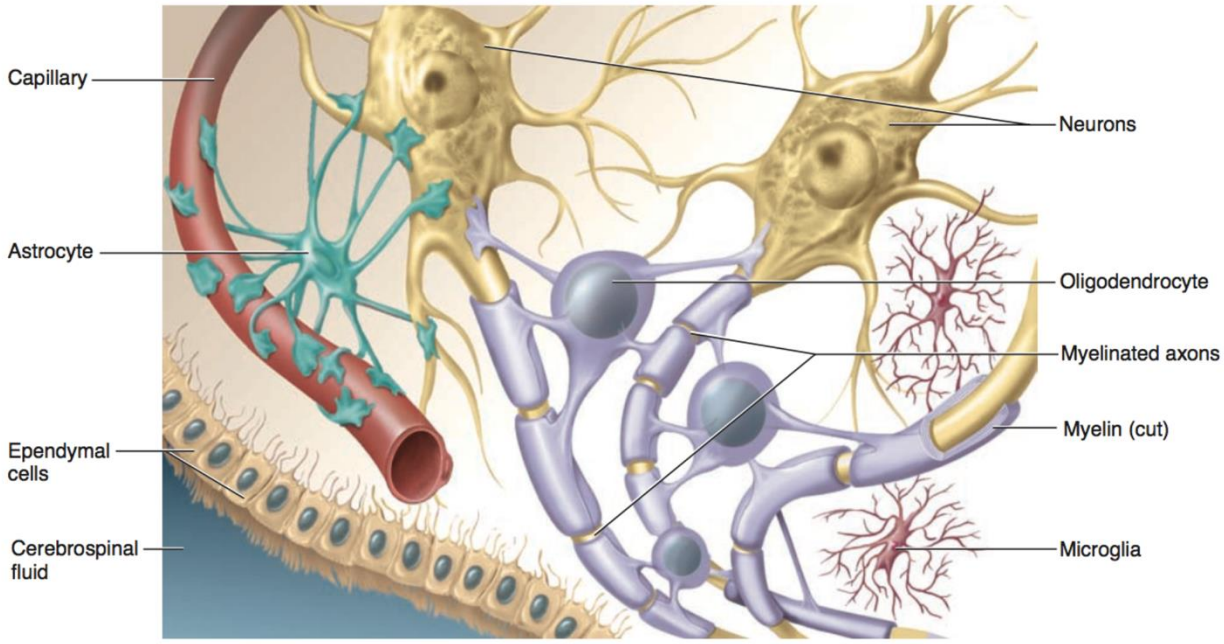

Figure 2-7, Adapted from (Widmaier et al. 2013). Representation of the main glial cells of the central nervous system.

2.1.1.2.3 Cortical structure: layer based

The spatial organisation of neuron bodies is uneven in the cortex. A straightforward parcellation can be made by **layer**: the cortex can be divided in six layers where neurons bodies are found with differents shapes and concentrations. Cortical neuron come in two main forms: excitatory (**pyramidal**) and inhibitory (Azevedo et al. 2009). Commonly, a neuron 'belongs' to the layer in which its body cell is sited, even if its dendrites span several more layers. Inhibitory neurons are in minority (20%) and have more diverses morphologies. Inhibitory neurons are known as local circuit neurons because they are purely intrinsic, i.e. they remain entirely in the cortex. Some pyramidal neurons are also intrinsic but others make short and long connexions with others parts of the CNS. **Figure 2-8** shows a representation of the structural organisation of neurons through the differents layers of the cortex.

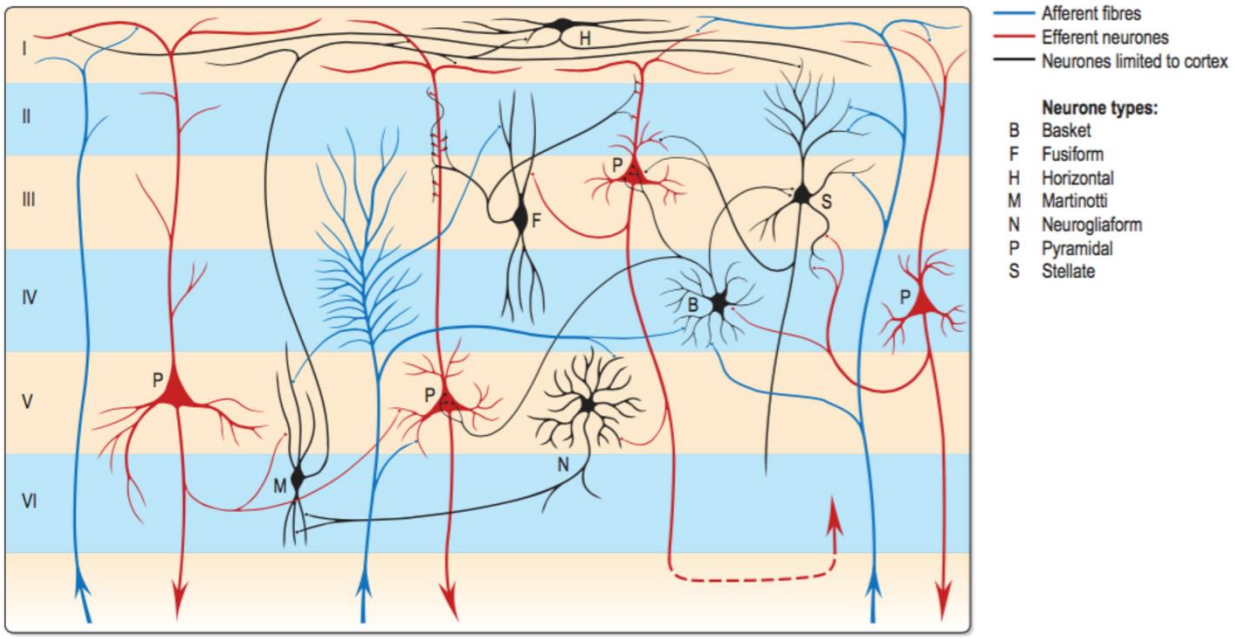

Figure 2-8, From (Gray & Standring 2008). Representation of the structural organisation of neurons through the differents layers of the cortex. The most frequent types of neocortical neurones, showing typical connections with each other and with afferent fibers are represented.

Basically, there are two layers of pyramidal neurons (III and V) indicated with two layers of granular neurones (non-pyramidal, II and IV), all of this enveloped in two mainly connective layers (I and VI).

More precisely, **Layer I** is called the molecular zone and contains mostly horizontal (or tangential) cell fibers. This layer contribute to the cortico-cortical connexions which for example contribute to connect two adjacent Brodmann areas. **Layer II** is the external granular layer and contains both small and non-pyramidal neurons. Myelin staining shows mainly vertically arranged neural fibers. **Layer III** is the external pyramidal layer, it contains pyramidal cells of varying sizes and scattered non-pyramidal neurons. This layer is often subdivided in **IIIa**, **IIIb** and **IIIc**, containing respectively small, medium and large pyramidal neurons. Like in Layer II, myelin staining reveals mainly vertical myelinated fibers. **Layer IV** is the internal granular layer, it contains small round cell bodies of non-pyramidal cells. In this layer, the myelinated fibers are mainly horizontally organised. **Layer V** is the internal pyramidal layer, it contains the largest pyramidal cells. Scattered non-pyramidal cells are also present. It contains descending vertical

fibers as well as a prominent central band of horizontal fibres. Finally, **Layer VI** includes neurons with a variety of shapes, mostly small to medium in size. This layer is adjacent to the white matter clear determination of its boundary is not always possible. **Figure 2-9** shows a representation of the cortical layers as revealed by three different staining methods, namely the **Golgi staining**, the **Nissl staining** and the **Weigert staining**. These staining methods are complementary, they respectively show the whole neurons (soma + dendrites), the cells bodies only and the myelinated fibers only (Gray & Standring 2008).

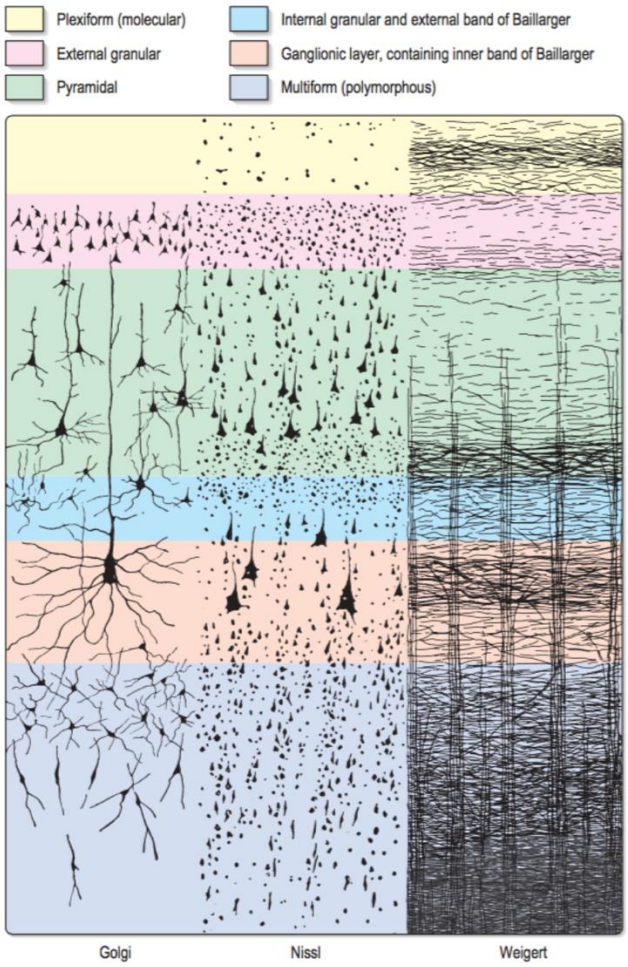

Figure 2-9, From (Gray & Standring 2008), representation of the six cortical layers as revealed by three different stainings, namely the Golgi staining, the Nissl staining and the Weigert staining. These staining methods are complementary, they respectively show the whole neurons (soma + dendrites), the cells bodies only and the myelinated fibers only.

2.1.1.2.4 Cortical parcellations: Atlases

2.1.1.2.4.1 Morphological atlases

There are many features of the cortex that could be used to create a parcellation or an atlas. In the literature, the most occurring parcellations are based either on the **cortical morphology**, **the microstructural organisation** or the **functional processing**. Below are some examples of these three types of atlases. The next sub-section will review challenges encountered when creating an atlas, such as the Human cortex variability or the choice of number of regions.

The morphological parcellation is one of the most intuitive, unfortunately, this is also the most variable across the literature. Firstly, each hemisphere of the cortex can be divided in four areas called "lobes": the **frontal lobe**, the **parietal lobe**, the **temporal lobe** and the **occipital lobe**. For example, this basic parcellation has been made in 1858 by Henry Gray (Gray & Standring 2008), as shown in **Figure 2-10 A**. This basic representation is quite robust because the borders of the four areas are defined from evident sulci present in every Human brain.

Furthermore, instead of using the lobes, the main sulci and gyri can be used to divide the cortex. For example, the Mindboggle atlases made by the group of freesurfer (Fischl et al. 2004; Desikan et al. 2006; Klein & Tourville 2012) segment the cortex based on different gyri such as the precentral gyrus or the orbital gyrus, **Figure 2-10 B**. A name is given to every gyrus, then the gyrus boundaries can be drawn manually or automatically by using a parcellation software.

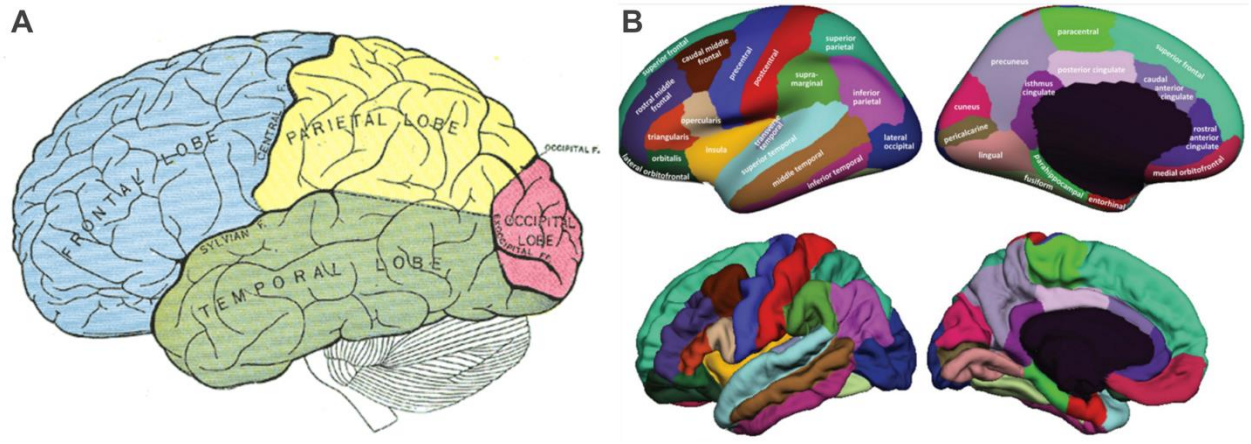

Figure 2-10**, (A)** Basic four-areas parcellation of the cerebral cortex, made by Henry Gray in 1858 (Gray & Standring 2008). These four areas are: the frontal lobe (blue), the parietal lobe (yellow),

the temporal lobe (green) and the occipital lobe (red). **(B)** Anatomical atlas made from cortical gyri parcellation (Klein & Tourville 2012).

2.1.1.2.4.2 Microstructural atlases

Atlases based on **microstructural organization** are difficult to create but are very useful to study the composition of the cortex. The main microstructural atlases in the literature are describing either the **cyto-architecture** or the **myelo-architecture** of the human cortex. Cyto-architectural atlases are classifying areas of the human cortex depending on the cell composition, for example the number of visible cortical layer and the number and shapes of neurons present in these layers. A pioneer in cytoarchitectural atlases is **Korbinian Brodmann**, who created a cyto-architerctual atlas of the Human cortex in 1909 (Zilles & Amunts 2010; Brodmann 1909).(Zilles & Amunts 2010; Brodmann 1909) that is still widely used in many studies. Brodmann used the **Nissil** method to stain histological samples of the cortex and study the cellular organisation of neurons. He found approximately 50 adjacent regions containing distinct cellular organisations. **Figure 2-11** shows a representation of the Brodmann atlas as well as samples of several cellular organisations.

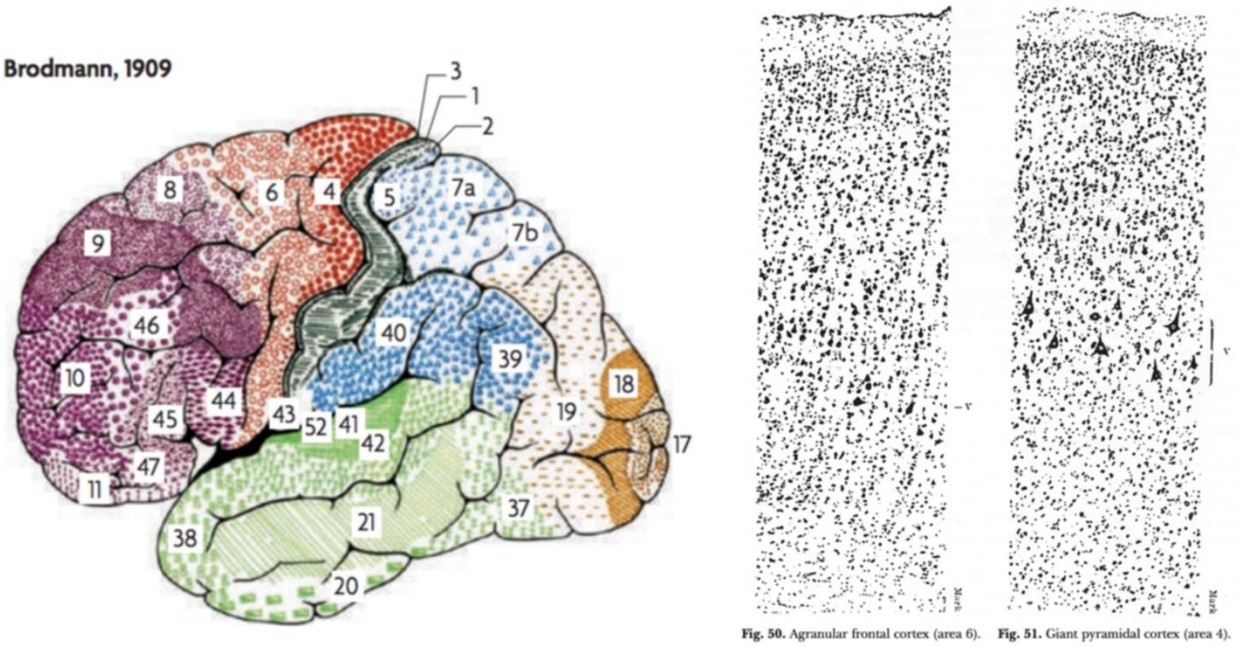

Figure 2-11, atlas of the Brodmann areas (left,(Zilles & Amunts 2010) of the Human cortex and samples of the cellular organisation of the brodmann area (BA) 6 and BA 4 in monkeys (right, (Brodmann 1909)).

While Brodmann used the Nissil stain to visualize the neural cell bodies of the cortex, Oscar and Cecile Vogt used the **Weigert** stain to reveal the myelinated nerves fibers. Based on the amount and organization if the cortical myelinated fibers, they have proposed a 185-regions atlas of the human cortex (Vogt 1911). However, their work is not as widely used as the Brodmann atlas, maybe because of the complexity of the atlas, or because of the lack of documentation. For this reason, Rudolf Nieuwenhuys decided to pass through all the Vogt-Vogt archives and recreate a modern version of the myelo-architectural Vogt-vogt atlas (Nieuwenhuys et al. 2014; Nieuwenhuys 2013). **Figure 2-12** shows a representation of the restored Nieuwenhuys atlas and some sample of the myelinated fiber staining made by Vogt and Vogt in 1911.

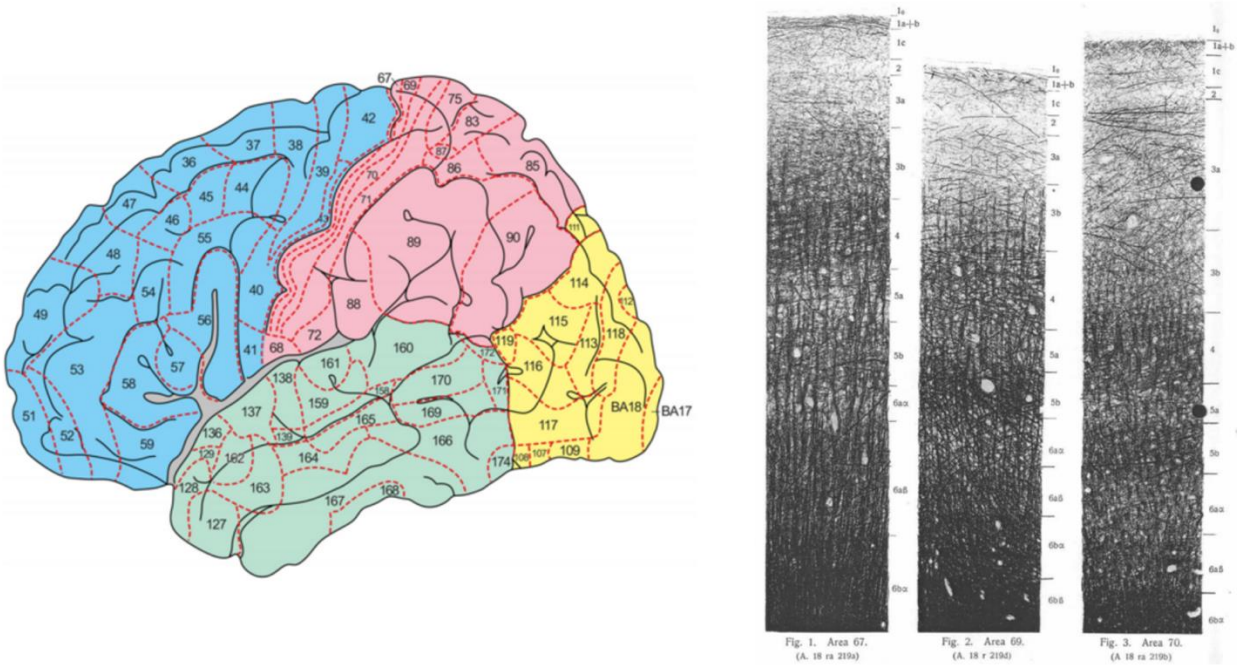

Figure 2-12, Nieuwenhuys atlas: restored version of the myelo-architectural Vogt-Vogt atlas (left, (Nieuwenhuys et al. 2014) and sample of the myelinated fibre, stained with the Weigert method made by Vogt and Vogt in 1911 (Vogt 1911).

2.1.1.2.4.3 Functional atlases

Finally, the cortical parcellation by **functional processing** is widely used in the literature. Indeed, the functional areas are containing groups of neurons (or tracts) that link a specific functional region of the body. For example the motor area contains neurons governing motor functions and visual area receives the neuronal inputs from the optic nerve. Interestingly, it turns out that many of the Brodmann areas have been correlated closely to diverse cortical functions (Gray & Standring 2008; Barbier et al. 2002; Lanzilotto et al. 2013; Glasser & Van Essen 2011), although they were defined based on their neuronal organisation. This has surely contributed to the standing of the Brodmann atlas. **Figure 2-13** shows a detailed parcellation of Brodmann areas and the legend names the main Brodmann areas associated with a specific function.

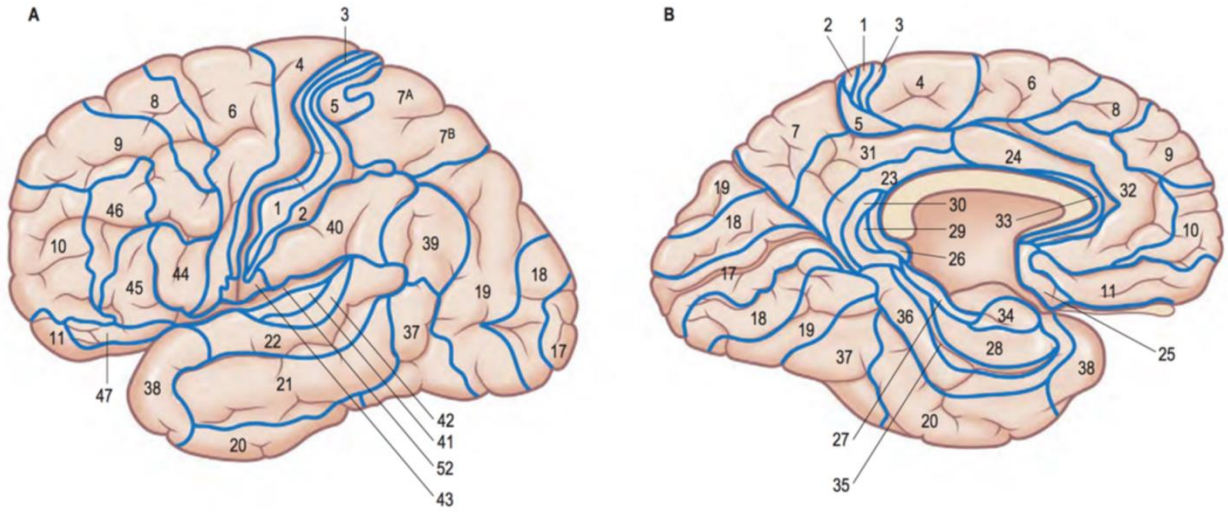

Figure 2-13, From (Gray & Standring 2008), shows a detailed parcellation in Brodmann Areas (BAs) in lateral (A) and medial (B) views of the left hemisphere of the Human cortex. Here is a non-exhaustive functional description of some BAs:

- BA 1, 2 & 3: Primary Somatosensory Cortex, i.e. receive somatosensory inputs.
- BA 4: Primary Motor Cortex, i.e. receive and send motor commands.
- BA 6: Premotor Cortex, i.e. helps the motor cortex for example by preparing movements.
- BA 17, 18 & 19: Primary, Secondary and Associative Visual Cortices.
- BA 41 & 42: Auditory Cortex.
- BA 43: Gustatory Cortex.

2.1.1.2.4.4 Reported challenges

The main challenge in creating an atlas is the compromise between the variability of the Human cortex and the desired level of accuracy. The first question is: What is my Atlas based on? Previous sections showed that an atlas of the cortex could be based on the cortical morphology, on the microstructural organization or on the functional processing. In fact, metrics can be used to create an atlas, for example the gyri's spatial orientation, the cortical thickness, content in iron and so on. The chosen metric depends on the purpose of the atlas and the means available to create it. Then comes the question of "how accurate does my atlas need to be?", or "How do I define boundaries between two regions". For example, an atlas based on the microstructural organisation

across cortical layers (as Brodmann did) could have been done with only five areas, as presented in **Figure 2-14**, containing only the Agranular, Frontal, Parietal, Granular and Polar organisations. However, Brodmann had decided to subdivide his parcellation in more than forty regions because he thought the variation of the organisation was clear enough to do so. This highlights the fact that the number of region in an atlas is an arbitrary parameter that has to be carefully chosen. Indeed, if there are very few regions the atlas might not be useful to precisely locate a small region of interest, for example a cortical lesion. Furthermore, if there are too many regions, the variability of the cortex morphology across people might affect the precision of the areas locations, and again the usefulness of such an inaccurate atlas can be questioned.

A technique to minimise the inter-subjects variability is to deform and project the subject cortex into a common cortex-template allowing to average the information of several subjects (Klein & Tourville 2012) and thus create robust atlases. This technique was namely used to create the PALS-B12 Brodmann Atlas (Van Essen 2005) that is further used in this work.

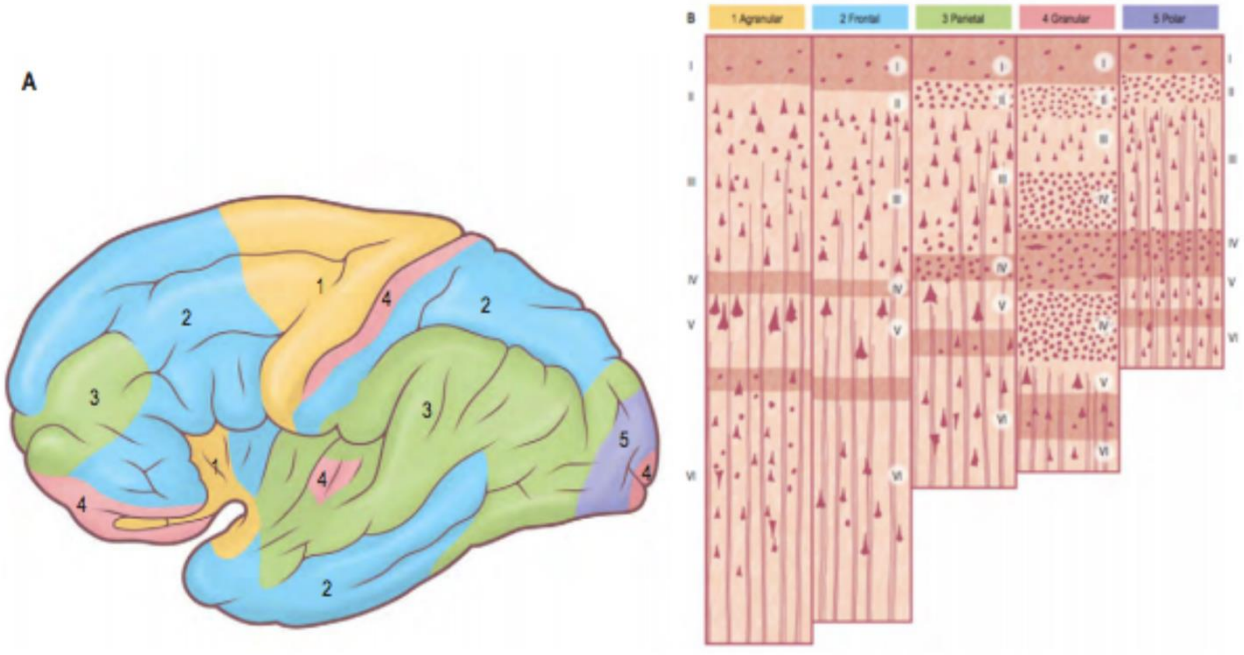

Figure 2-14, From (Gray & Standring 2008). Representation of the five main neural organisations of the cerebral cortex (B) and a map of their respective location (B).

2.1.2 Pathophysiology of Multiple Sclerosis

2.1.2.1 Overview of MS in the central nervous system

Multiple Sclerosis (MS) is a chronic, **inflammatory** and **demyelinating** disease of the central nervous system. MS inflammation affects the sheaths of myelin in the brain and the spinal cord. This damage disrupts the ability of regions of the central nervous system to communicate, resulting in various symptoms including physical, mental and sometimes psychiatric problems. Most of the time the inflammation disappears and reparation mechanisms, called **remyelination** take place and allow the patient to recover. However, sometimes the inflammation and demyelination are too high compared to the remyelination mechanism and non-reversible connectivity disorders occurs (Compston & Coles 2008; Anon n.d.). These different progressions of disease lead to several phenotypes of MS, depending on the progression of the disease over time. **Relapsing Remitting MS** (RRMS) patients present *relapses* which are "spikes" of disability over time after which patients fully or partially recover (Figure MS1 A). **Secondary Progressive MS** (SPMS) patients show a constant and non-reversible progression of disability, **Figure 2-15 A**. As well as functional disability episodes, inflammation events, axonal loss and brain atrophy occurs in various intensities depending of the MS phenotype, **Figure 2-15 B**.

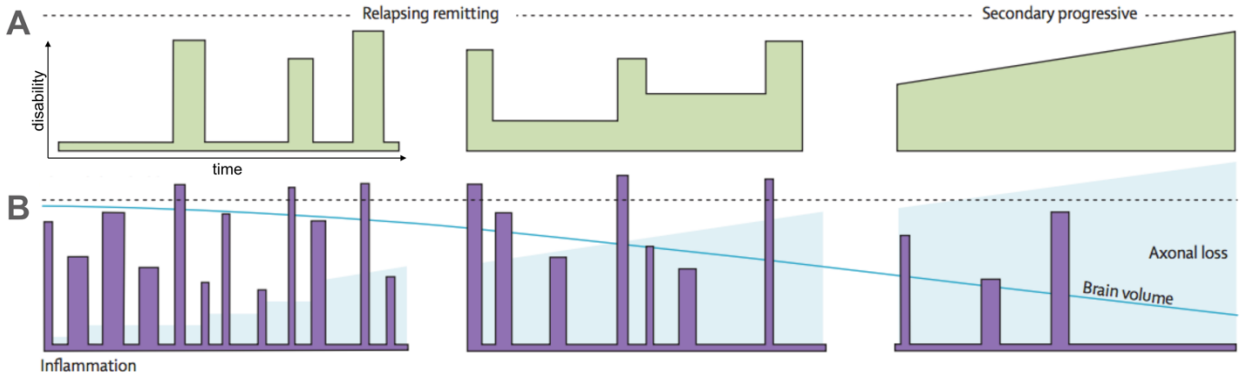

Figure 2-15, adapted from (Compston & Coles 2008). **(A)** Example of the progression of the disability over time for RRMS and SPMS patients. **(B)** Example of the progression of inflammation events, axonal loss and brain atrophy over time for RRMS and SPMS patients.

Loss of myelin (or demyelination) occurs in **plaques** which are localised areas where myelin is being attacked, **Figure 2-16**. Plaques have various sizes and shapes, their volume can be

less than a cubic millimeter to more than several cubic centimeters. Moreover, axonal demyelination can take place in diverse myelinated axons of the CNS, such as spinal cord axons, cerebral white matter axons or cerebral grey matter axons. GM demyelination has been challenging to detect with MRI, for this reason MS used to be wrongly called a *white matter disease*. Indeed, the recent improvement of MRI features, such as the spatial resolution, the signal to noise ratio (SNR) or the contrast mechanisms, helped to observe demyelination spots inside the cerebral cortex, **Figure 2-16 B**. This finding raised new questions: Is there a link between WM and GM demyelination? If yes, which one is afferent and which one is efferent? Which one has the more effect on functional deficits? And so on. Thus, study of cortical demyelination in MS is becoming an important field of research. The goals being to better understand the pathophysiology of the disease and to target potentials treatments to damaged cortical areas. Cortical demyelination will be discussed further as it is the main topic of my research.

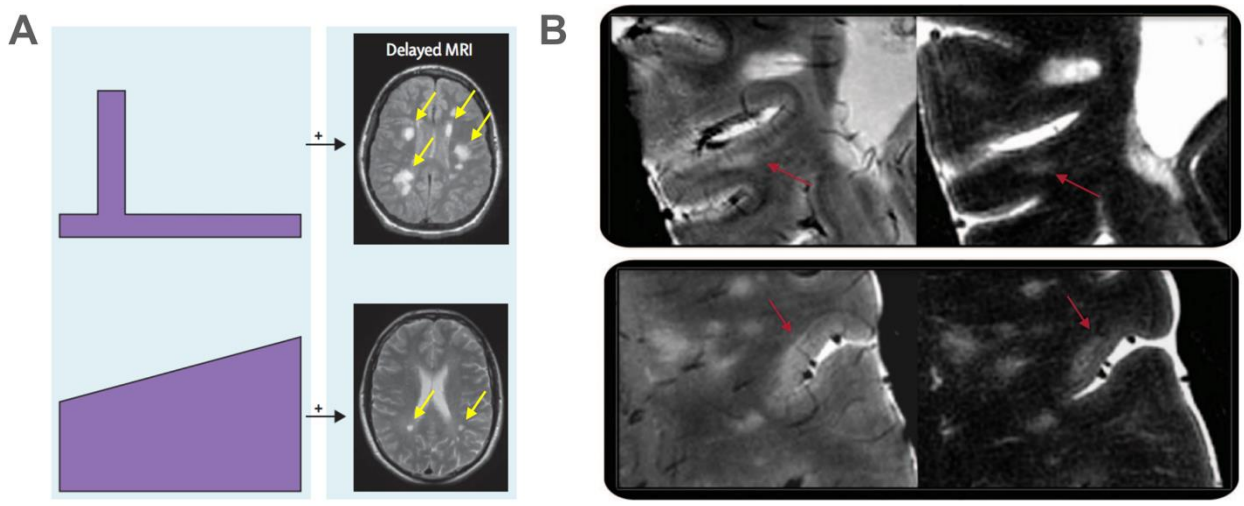

Figure 2-16**,** Adapted from (Compston & Coles 2008) (A) and (Mainero et al. 2009) (B). A: Example of WM plaques or lesions observed in RRMS and SPMS patients. B: Example of plaques or lesions in the cortical grey matter of MS patients.

2.1.2.2 Elements of MS pathophysiology

2.1.2.2.1 Causes of Multiple Sclerosis

Even though the causes of multiple sclerosis are still unclear, studies are mostly reporting **environmental** and **genetic factors** (Compston & Coles 2008). The global distribution of multiple

sclerosis can be generalised as increasing with distance north or south of the equator, but some countries do have a higher incidence of MS, e.g. Canada, UK, Sweden, Finland or New Zealand. In Canada, a significant increase in incidence of MS has been reported in Canadian women over the past 30 years (Orton et al. 2006), causing a change in the female to male ratio to more than 3:1. Moreover, it has been reported that hygiene can be a negative indirect factor, indeed, individuals not exposed to infections early in life, because of a clean environment, make aberrant responses to infections as young adults (Levin et al. 2010). Especially, an inadequate immune response to the Epstein-Barr virus can cross-react with myelin and induce demyelination, because several T-cell receptor peptide contacts are identical for myelin basic protein and Epstein-Barr virus (Lang et al. 2002). Some studies suggested other environmental triggers such as low sunlight, vitamin D deficiency, diet, geomagnetism, air pollutants, radioactive rocks, cigarettes, and toxins (Marrie 2004). Genetics also plays a role in MS. The familial recurrence rate is about 20% to 30% depending on the country and which first-degree relative is diagnosed with MS (Willer et al. 2003).

2.1.2.2.2 Disease mechanisms

The formation of the sclerotic plaque is the end stage of a process involving inflammation, demyelination and remyelination, oligodendrocyte depletion and degeneration of astrocytes, axons and neurons in general. However, the order and relation of these separate components remain fully to be resolved. Some studies suggest that the process starts with the migration of **autoreactive lymphocytes** across the blood brain barrier then, because of a regulatory defect, these cells are allowed to set up an immune response within the brain (Viglietta et al. 2004). Failure of local regulatory mechanisms within the brain accounts for the particular sites of inflammation, causing **plaques** that cluster around the lateral ventricles, corpus callosum, throughout the spinal cord, in the subcortical white matter and in the cerebral cortex. More specifically, the inflammation would be partly due to a T-cell subtype that secretes interleukins-17, disrupting the **blood-brain-barrier** and allowing efficient penetration of Th17 cells into the brain where they can kill neurons (Kebir et al. 2007). Demyelinating lesions show axonal injury with transection that correlates with T-cell and microglial infiltration (Kuhlmann et al. 2002). Moreover, areas of demyelination coexist with diffuse neuronal and axonal degeneration (Anderson et al. 2008). Demyelinating lesions seem to grow slowly by radial expansion whereas focal brain inflammations fades into diffuse microglial activation resulting in extensive abnormalities of the normal appearing white matter (Kutzelnigg

et al. 2005). The interplay between degenerative and inflammatory processes is still a topic of research. Indeed, causality between axonal loss and demyelination is difficult to interpret, and both mechanism are maybe independent. To some extent, every pathological component can be detected *in-vivo* with MRI.

2.1.2.2.3 MRI studies of MS

Table 2-1 gives an overview of various MRI contrasts that have been shown sensitive to the main pathological components of MS.

Table 2-1, Overview of various MRI contrasts that have been shown sensitive to the main pathological components of MS. These studies have looked at the sensitivity of MR modalities to MS-related pathology, however they did not address (or only partially addressed) the issue of specificity.This list is not exhaustive, studies were selected by pertinence and recent publication dates.

Component of MS Pathology	Sensitive MRI modality	References
Inflammation	Hyperintense T_2w Gadolinium FLAIR	(He et al. 2001)
Axonal loss/injury	Hyperintense T_1w DTI DSI MTR	(Barkhof & van Walderveen 1999; Kidd et al. 1999) (Shu et al. 2011) (Wang et al. 2015) (Schmierer et al. 2007)
WM demyelination and WM remyelination	MT MTR (1.5T, 7T) qT_1 qT_2 DSI (RD) T_2* (7T) MTV Hypointense T_2w	(Pike 1997) (Mottershead et al. 2003; Schmierer et al. 2004; Schmierer et al. 2008) (Mottershead et al. 2003; Schmierer et al. 2008) (Mottershead et al. 2003; Schmierer et al. 2008) (Wang et al. 2015) (Li et al. 2015) (Vargas et al. 2015) (Barkhof & van Walderveen 1999)

GM demyelination and GM remyelination	MTR (1.5T, 9.5T) T_2* (7T)	(Derakhshan et al. 2014; Chen et al. 2013) (Pitt et al. 2010; Li et al. 2015)
Gliosis	Mid-intense T_1w T_2w	(Barkhof & van Walderveen 1999)
Microglia and macrophages activation	PET T_2* (7T, hyperintense ring)	(Faria et al. 2014) (Pitt et al. 2010)
Vasogenic oedema	DSI (RD) Hyperintense T_2w	(Wang et al. 2015) (Barkhof & van Walderveen 1999)
Intracellular oedema	Mid-intense T_1w	(Barkhof & van Walderveen 1999)
BBB disruption	Gadolinium	(He et al. 2001)

All of these studies have validated the link between **pathological components** and **MRI contrast**, for example by using ex-vivo histology to directly observe a specific pathological feature and draw a correlation with the variations of the studied MRI contrast. These studies are extremely useful to properly analyse *in-vivo* MRI images of MS patients, and thus they contribute making MRI the ultimate tool for *in-vivo* study of the progression of the disease.

However studies involving **histological validations** are challenging in terms of time, cost and resources. It is not always possible to compare the in vivo image acquired with a brand new MRI contrast and the corresponding ex-vivo histology of the tissue. For this reason, many MRI studies of MS patients are comparatives. It means that MR images of MS patients are compared to the same MR images acquired in Healthy Controls subjects (HC). Such studies are useful to find out what kind of **MS lesions** the studied MRI contrast is able to detect. However, the nature of such lesions has to be **inferred based on prior knowledge and similar studies**. For example, a vasogenic oedema and a local demyelination can appear very similar on T2-w images (hyperintense spot) (Barkhof & van Walderveen 1999; Sahraian et al. 2010), therefore both changes will be called lesions. The term *lesion* is rather vague, a lesion does not describe the area where a specific pathological component is taking place, but describes an area where the MRI signal takes significantly abnormal values in comparison with healthy tissue. The *a priori* physiological mechanism underlying a lesion remains unsure since we know that several pathological features are occurring simultaneously in MS. A lesion can be an inflammation, an oedema, a loss of myelin,

a loss or injury of axons, an area with activation of macrophages, an area of re-myelination or even a combination of several simultaneous processes.

The term lesion being clarified, it is important to say a few words about two kinds of lesion occurring often in the literature: the **local lesion** and the **diffuse lesion**. A **local lesion** is a relatively small region (from some millimeters to (say) 4 or 5 centimeters maximum) where the MR signal drops or rises strongly enough to be detected with a naked eye. A **diffuse lesion (**or **diffuse pathology)** points out spread changes that are detected using software because they are visually not detectable. Because diffuse lesions are hard to delimit, arbitrary areas can be chosen and compared between MS patients and HC. A widely used example is to compare the changes occurring in the Normal Appearing White Matter (NAWM) or in the Normal Appearing Grey Matter (NAGM) in MS vs HC. **Table 2-2** gives an overview of MRI contrasts mainly used to observe various types of MS lesions:

Table 2-2, Overview of MRI contrasts mainly used to observe various types of MS lesions. This list is not exhaustive (especially for WM studies). While thousands of studies exists on the topic, studies were selected by pertinence and recent publication dates, with the emphasis put on **quantitatives MR modalities**.

MS lesion type	**Sensitive MR modality**	**References**
WM focal lesion	Hyperintense T_2w Hypointense T_1w QSM qT_1 qT_2 MTR	(Sahraian et al. 2010) (Sahraian et al. 2010) (Chen et al. 2014; Reichenbach et al. 2015) (Schmierer et al. 2008) (Schmierer et al. 2008) (Schmierer et al. 2004; Schmierer et al. 2007)
GM focal lesion	DIR (3T, 7T) FLAIR (7T) SPRG MTR T_2*	(Geurts & Barkhof 2008; de Graaf et al. 2012) (de Graaf et al. 2012) (Tardif et al. 2012) (Chen et al. 2013; Derakhshan et al. 2014) (Pitt et al. 2010; Mainero et al. 2009)
NAWM alteration	qT_1 qT_2 MTR	(Schmierer et al. 2008) (Schmierer et al. 2008) (Schmierer et al. 2004; Schmierer et al. 2007)
NAGM alteration	MTR (1.5T, 9.4T) T_2* (7T)	(Chen et al. 2013; Derakhshan et al. 2014) (Cohen-Adad et al. 2011; Mainero et al. 2015)
Laminar cortical changes	T_2* (7T)	(Cohen-Adad et al. 2011; Mainero et al. 2015)
WM rimmed lesions	T_2* (7T)	(Harrison et al. 2016; Pitt et al. 2010)

As seen in **Table 2-2**, detection of MS lesions in the cortex can be done by only few MR contrasts and requires higher field strengths. Indeed, MS cortical pathology is more challenging to observe *in-vivo* because of low MR signal emitted from the cortex. If the focus is put on the cortical pathology, Table 2-2 suggests that MTR, 7T T_2*, SPGR, qT_1, qT2, FLAIR and DIR, can detect cortical lesions. Moreover, if the pathological component of interest is in the cortex, Table 2-1 tells

that MTR and 7T T_2* are sensitive to it. This implies that MTR and 7T T_2* are sensitive to cortical demyelinating lesions.

2.1.2.3 MS in the cerebral cortex

Although MS was, until recently, called a white matter disease, the involvement of grey matter was reported as far back as the beginning of the 20th century (Dawson 1916). However, the significance of GM pathology was **underestimated** until recent histopathologic data revealed that they constitute a substantial proportion of the total brain MS lesion load (Kidd et al. 1999).

The pathological feature of cortical lesions (CL) is mainly demyelination (Tardif et al. 2012). They also occasionally exhibit a minor microglial reaction, axonal transection, as well as neuronal, glial, and synaptic loss (Wegner et al. 2006; Trapp et al. 1998). The contrast between demyelinated CLs and surrounding normal appearing cortex is further reduced due to the lower myelin content of GM, about 10% that of WM.

(Bø et al. 2003) defined a system of CL classification that distinguishes mixed GM-WM lesions (type I, leukocortical) from purely GM lesions. The latter include small intracortical lesions (type II), subpial lesions that affect the superficial cortical layers and may extend over several gyri (type III, subpial), and lesions affecting the entire width of the cortex from pial surface to the subcortical WM (type IV).

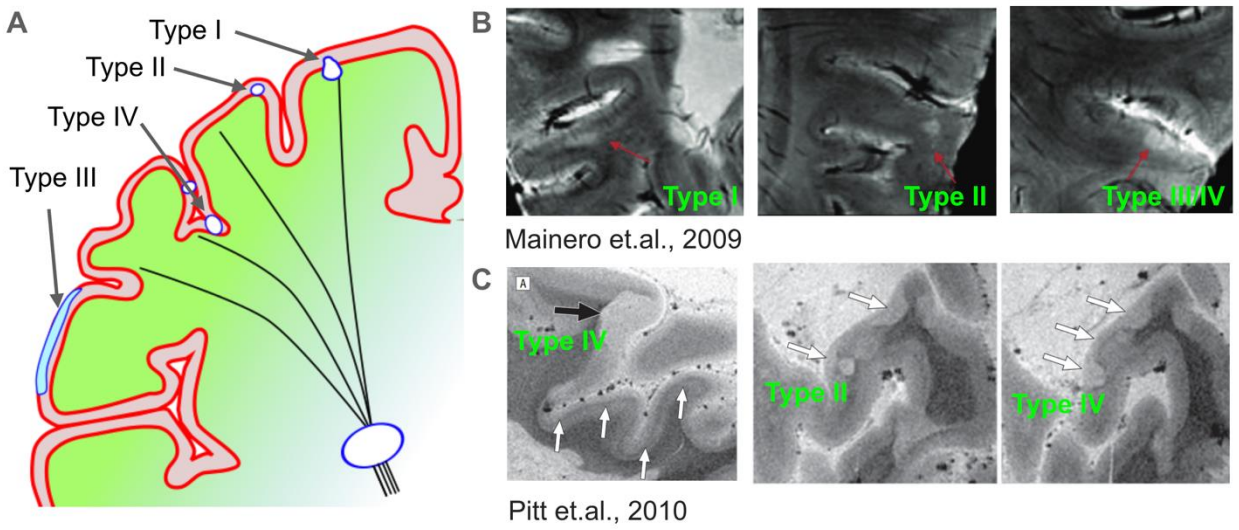

Figure 2-17**. (A)** Representation of the four types of cortical lesions (courtesy of Dr. C. Louapre). **(B)** Example of cortical lesions seen on MS patients, using 7T FLASH T_2* modality. Adapted from (Mainero et al. 2009) **(C)** Example of cortical lesions seen on MS patients, using 7T T_2*w modality. Adapted from (Pitt et al. 2010).

Type III subpial lesions are most extensive and frequent, and may lead to general subpial demyelination affecting up to 70% of the total cortical area (Bø et al. 2003; Kutzelnigg et al. 2005). The subset of CL load detected using DIR is highly correlated with overall CL load and demyelinated area (Seewann et al. 2011), and is associated with disability, especially cognitive impairment (Roosendaal et al. 2009; Calabrese et al. 2009; Calabrese et al. 2010; Mainero et al. 2015).

However, combined MRI and neuropathology studies of fixed (Geurts et al. 2005; Seewann et al. 2011) and fresh (Seewann et al. 2012) post mortem MS brain tissue have shown that CLs, in particular type III subpial lesions, remain significantly under-detected using 3 Tesla DIR and FLAIR images. Ultra-high field imaging (≥7 Tesla (T)) and multichannel phased array coils have contributed to improved in vivo imaging of cortical MS pathology, due to the increase in signal-to-noise ratio and accelerated acquisition (Mainero et al. 2015; Cohen-Adad et al. 2011). Despite using ultra high field imaging to detect the Type III *"diffuse"* cortical lesions has been been revealed promising (Mainero et al. 2015; Cohen-Adad et al. 2011), a lack of specificity regarding the nature of observed 7T T_2* changes arises because of it's sensitivity to several underlying

mechanisms (Cohen-Adad 2014; Stüber et al. 2014). Indeed, 7T T_2* has been shown to be sensitive to myelin distribution in the cortex (Cohen-Adad et al. 2012; Deistung et al. 2013; Mainero et al. 2015) but also to others features of the cortical tissues, such as iron content (Fukunaga et al. 2010; Stüber et al. 2014) or fiber sizes and orientation (Hwang et al. 2010; Lee et al. 2012; Pitt et al. 2010).

The main goal of my Master's thesis is to propose a method to increase the specificity in the *in-vivo* detection of cortical demyelination such as diffuse or type III demyelinating cortical lesions, using MRI. Now that we have a better idea of the scope of this work, let's take a deeper look inside the technology involved in order to better understand the solution proposed. The next chapter will review the physics part of this work: the principles of Magnetic Resonance Imaging.

2.2 Physics Review

2.2.1 MRI basics

Magnetic Resonance Imaging is a powerful noninvasive imaging modality that is widely used around the globe. MRI is based on the phenomena of Nuclear Magnetic Resonance (NMR) of atoms. Sometimes the acronym NMR is used to designate the MR device, but word *nuclear* is commonly removed to avoid the negative connotation and the amalgam with nuclear ionizing radiations phenomenons. All nuclei with an odd number of neutrons possess a nuclear **spin angular momentum**. In biological tissues, hydrogen (^{1}H) is the most abundant because it is present in every water molecule (H_2O). The spin acts as a magnetic dipole that **precesses** around the nucleus at a rotational frequency called **Larmor frequency.** The Larmor frequency \omega is proportional to the strength of the surrounding magnetic field *B*.

$$\omega = \gamma B$$

where γ is called the gyromagnetic ratio. For ^{1}H, $\gamma/2\pi = 42.58$ [MHz/Tesla]. In MR devices, a static magnetic field, called B_0, is applied to the whole sample in order to macroscopically polarize all the angular momentums in the same direction (arbitrarily defined as the *z*-direction). Typical B_0 field strengths are within the range 1.5T to 7T. Spins will then be excited by a rotational magnetic field called $\boldsymbol{B_1}$ which rotate at the larmor frequency in the *xy*-plane

in order to be seen as stationary in the point of view of the spin. To acquire an MR image, a brief excitation with a magnitude $\boldsymbol{B_1}$ will rotate the spins towards the x-y planeand will make all spins precess with the same phase. Once the $\boldsymbol{B_1}$ field is turned off, receiving antennas will record the signal emitted by the spins, while they go back to the steady state. Two independent phenomena will affect the recorded signal. Firstly, spins will eventually realign themselves with the main magnetic field B_0 thus making the macroscopic magnetization aligning to B_0 (z-direction), the characteristic realigning time can be measured and is called T_1 , **Figure 2-18 A**. Typical T_1 time is about 100-2000ms in the brain tissues. Secondly, when $\boldsymbol{B_1}$ field is turned off, **spin-spin interactions** will slightly affect the Larmor frequency of each spin, making them dephase with each other and destruct the macroscopic magnetization initially present in the xy-plane, the characteristic dephasing time is called $\boldsymbol{T_2}$, **Figure 2-18 A**. Typical $\boldsymbol{T_2}$ time is about 10-300ms. These two characteristic times, T_1 and $\boldsymbol{T_2}$ are properties of the imaged biological tissue and thus create the contrast observable in MR images **Figure 2-18 B**. The spatial encoding of the image is obtained with gradient fields that are used to affect the spin's Larmor frequency and the spin's phase depending on their location.

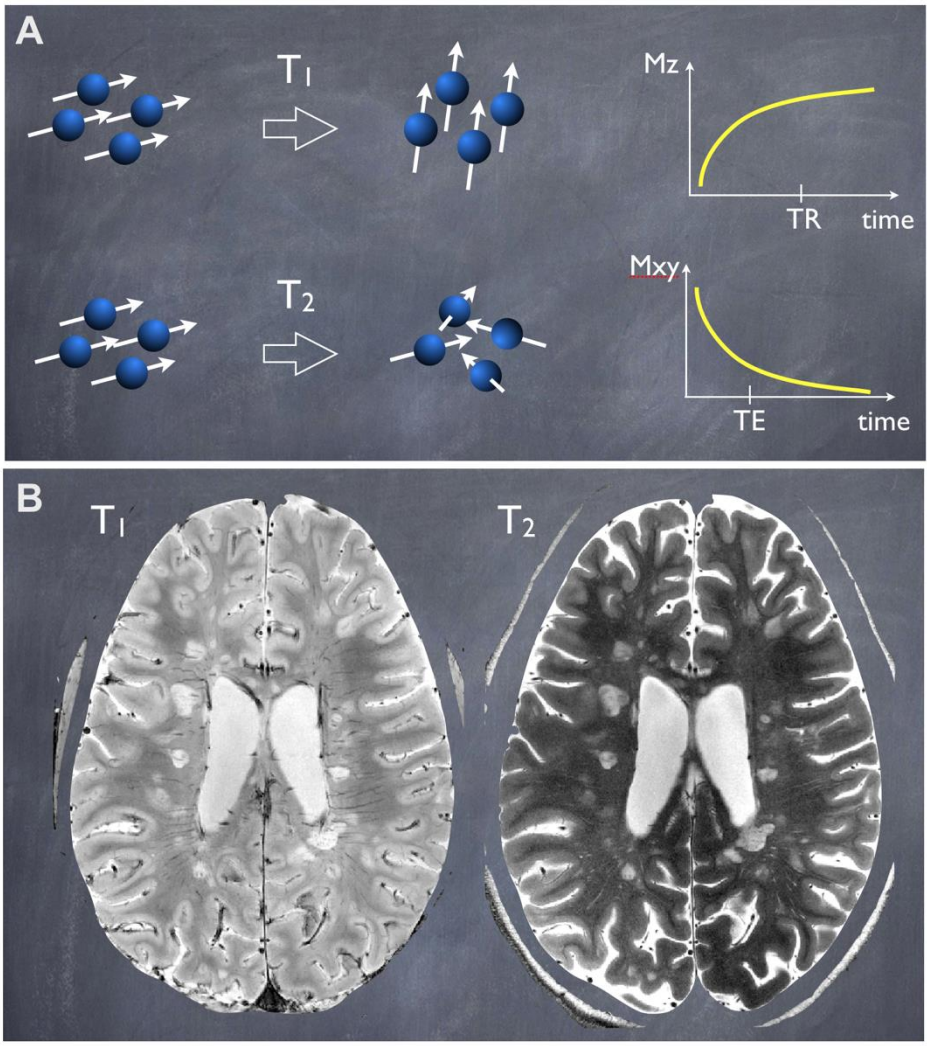

Figure 2-18**.** (A) Representation of the characteristic T_1 and T2 relaxation times. The B1 excitation rotates the spins in the xy plane and sets them in-phase. T_1 is the characteristic realigning time while T2 is the characteristic dephasing time. (B) MRI images of T_1 and T2 weighted contrasts, acquired at 7T.

The recorded signal depends on various parameters, such as the excitation time (TE), the repetition time (TR) or the kind of $\boldsymbol{B_1}$ pulse sequences, to cite only few of them. Every set of parameters will lead to a different MRI contrast. The most used MRI contrasts are T_1w, T2w and PDw (Proton Density weighted). These contrasts are recognizable by some specific features, for example, T_1w will show a GM darker than the WM, inversely T2W will show a darker WM (**Figure 2-18 B**), while PDw will present a very bright CSF. The letter "*w"* means *weighted*, it indicates

that such a contrast is not quantitative, i.e., when measured in another scanner with other parameters, the values will change. Even though two T2w images of the same patient acquired with the same acquisitions parameters will look similar, the values behind each voxel won't necessarily be comparable. It is like taking pictures of an object with various sources and positions of lighting. The object will still look the same, but the values of each pixel will show different numbers.

Because the necessity to perform group studies has arisen during the past decades, solutions had to be found to be able to quantitatively compare MRI images of different subjects, or different regions of the same brain. Thus, a set of quantitative MRI metrics (or contrasts) has been developed during the past years. To emphasize the fact that a metric is quantitative, the suffix *q* is sometime added before the metric's name, e.g. qMT, qT_2* or qT_1. Sometimes the *q* is not present, but the quantitative aspect of the metric is clarified by the context.

2.2.2 Quantitative MRI

2.2.2.1 Usefuleness of qMRI

MRI presents unprecedented opportunities to quantify *in-vivo* brain tissues properties, information about disease mechanisms and provide pronostics to patients. However, the abilities of MRI to accurately quantify tissues properties or brain metrics is challenging. For example, the variations of the scanner performance across space and time on a given machine, or the variability in software and hardware across platforms has to be taken into account to obtain quantitative measurements. Even simple quantitative measures such as brain volume or atrophy are subject to difficulties due to image qualities, quantitative measure implementation or variability in methods daily used by different centers. This section will summarize the principles and methods used to obtain the two quantitative metrics of interest in this study, which are MTR and T_2*.

2.2.2.2 MTR modality

Magnetization Transfer (MT) was first demonstrated in vivo by (Wolff & Balaban 1989). MT is a contrast based on a mechanism of exchange of magnetization between two different kinds of protons, characterized by different molecular environments. Interestingly, MT provides a source

of contrast different from T_1 and T2. MT reflects the relative density of macromolecules, such as lipids or proteins. As myelin has a lipid-protein structure (60-70% lipids and 20- 30% protein), MT is able to probe indirectly a measure associated with the myelin content. The MT phenomenon is complex, and several details of the process are still unknown.

2.2.2.2.1 Magnetisation transfer principle

The MT effect results from the interaction between two kinds of hydrogen nucleus. Protons in a liquid state (free state) associated with water molecules and protons in semisolid state associated with macromolecules. Macromolecular spins cannot be imaged by conventional MRI method, because of their very short T2 (<1ms). However, macromolecular spins can be indirectly imaged. Indeed it is possible to saturate macromolecular spins by an off-resonance radio frequency pulse because they have a much boarder absorption lineshape than the liquid spins, **Figure 2-19**. It creates a preferential saturation of the macromolecular spins that can be transferred to the liquid spins, depending on the rate of exchange (Levesque & Pike 2009). And hence, this water spin saturation can be detected with MRI (Henkelman et al. 2001).

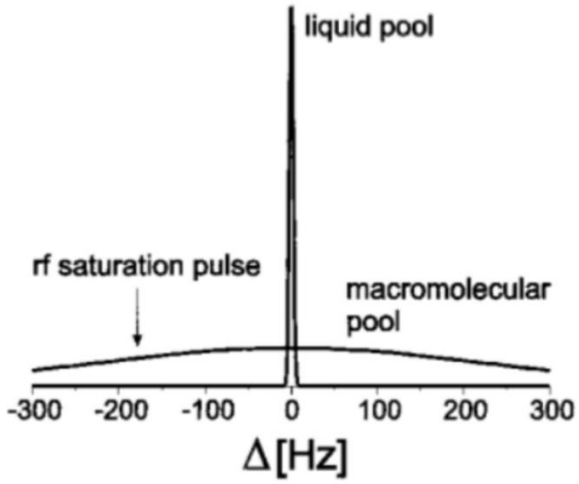

Figure 2-19**.** From (Henkelman et al. 2001). Schematic absorption lineshape of protons in the liquid pool (water protons) and protons in the macromolecular pool (protons linked to macromolecules).

2.2.2.2.2 Magnetisation Transfer Ratio

MT pulses are designed to saturate the semi-solid spins bound to macromolecules. This results in a suppression of the MRI signal that is proportional to the amount of macromolecules in a given tissue. One of the simplest way to separate MT phenomenon is to acquire two images, with and without off-resonance pulse. Taking the ratio of these two images highlights variations caused by the magnetization transfer. This method is called Magnetization Transfer Ratio (MTR) (Schmierer et al. 2004). MTR is the percentage difference of the image acquired with off-resonance saturation M_S and without saturation M_0:

$$MTR = \frac{M_0 - M_S}{M_0} * 100$$

An example of MTR image is shown in **Figure 2-20**. The MTR is a semi-quantitative measure reflecting the amount of bound protons. Moreover, some studies suggest that molecules associated with myelin dominate the MT exchange in WM (Schmierer et al., 2004) and that MTR increases with myelin content.

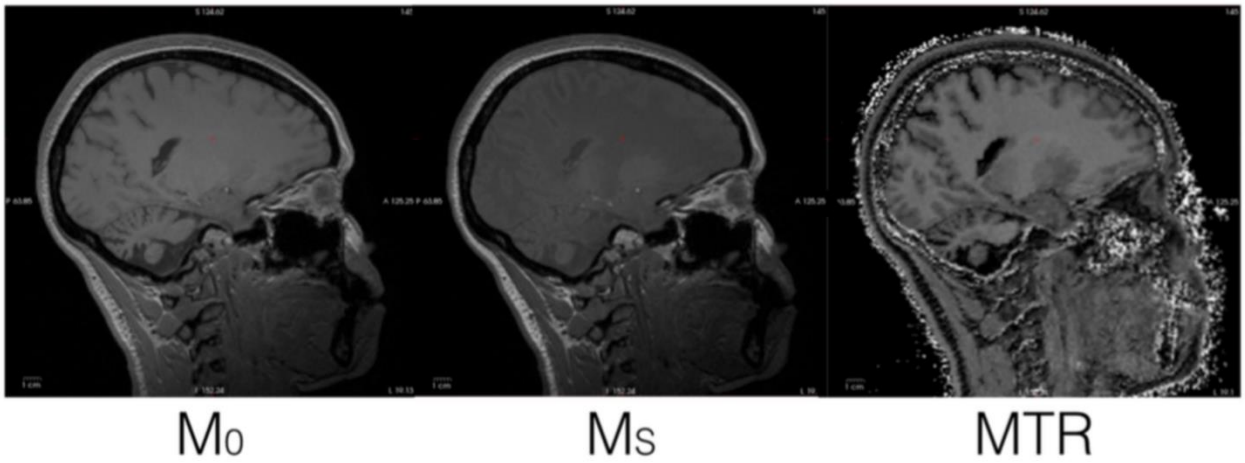

Figure 2-20**.** Adapted from (G. Mangeat, 2013). Example of MTR image of the brain.

2.2.2.2.3 Usefulness

The MT Ratio can be computed on a voxel by voxel basis to obtain MTR maps. The MTR is very popular to characterize WM disease and is often used to image the spinal cord. The MT phenomenon reduces the signal from tissues with "large amount of transfer" so it increases the

signal of low MT tissues such as MS lesions (Tanttu et al. 1992). Myelin content is a popular metric to study neurodegenerative diseases. MTR was shown to correlate with myelin content in WM (Schmierer et al. 2004) and is thus commonly used to study MS patients. Moreover, as shown in **Table 2-1 & 2-2**, MTR is commonly used to study GM lesions, especially demyelinating lesions (Tardif et al. 2012; Pitt et al. 2010; Chen et al. 2013; Derakhshan et al. 2014).

However, MTR is only a semi-quantitative metric, in the sense that MTR values depend on the sequence parameters (Berry et al. 1999). Moreover, some confounding factors hamper the MT phenomenon making it not fully specific to myelin. Firstly, B1 inhomogeneities related to RF transmission induce variabilities on the MT pulse power, which affect MTR measures. Secondly, MTR values are affected by T_1 relaxation (Pike Bruce 1996). Thirdly, others macromolecules such as large proteins can play a role in the MT effect and thus decrease the specificity of MTR to myelin.

My idea was to minimize these confounds by combining MTR with another metric sensitive to myelin but which does not share the same confounding factors. Let's see why T_2* was an appropriate candidate.

2.2.2.3 T_2* modality

T_2* contrast was shown to reveal feature of cortical anatomy. As we can see on **Table 2-1 & 2-2**, T_2* is also used by several groups to study features of MS progression in the cortex, especially at high fields strength (7T) (Mainero et al. 2015; Pitt et al. 2010; Cohen-Adad et al. 2011). The features of which T_2* is sensitive interestingly includes myelin content, but also iron, blood vessels and structure orientation.

2.2.2.3.1 T_2 principles*

As explained at the beginning of this section, the T2 relaxation time is coming from the dephasing amongst spins driven by the phenomena called *spin-spin relaxation*. In a perfect hypothetical case, the signal amplitude decay would be modulated by exp(-t/T2), where t is the time after excitation and T2 is the transverse relaxation time constant. However, various factors are influencing the T2

signal decay, for example water diffusion, influence of electrons from non-hydrogen atoms or the multiple water compartments. These inhomogeneities will slightly and locally change the value of the static magnetic field B_0, this will induce a faster dephasing and thus a faster relaxation time. The effective relaxation time taking into account these inhomogeneities is called T_2* (Haacke et al. 2005; Chavhan et al. 2009). T_2 and T_2* relaxations times are related according to the following equation:

$$\frac{1}{T_2^*} = \frac{1}{T_2} - \frac{\gamma}{2\pi}\Delta B_{inhom}$$

where γ is the gyromagnetic ratio and ΔB_{inhom} is the magnetic field inhomogeneity across a voxel.

2.2.2.3.2 Acquisition

T_2* volume is obtained by acquiring a set of T_2*w images with various echo-times (TE). Then, for each voxel, the T_2* decay curve is obtained by fitting a negative monoexponential curve on T_2*w values (Cohen-Adad 2014; Govindarajan et al. 2014). **Figure 2-21** shows the transverse relaxation decay curves as well as an example of experimentals T_2*w values acquired at regular TEs. The T_2* value of a voxel is a time constant (characterizing the response to a step input of a first-order, linear time-invariant system), and as such is defined as the time at which the signal is 37% of the maximum signal (at t=0).

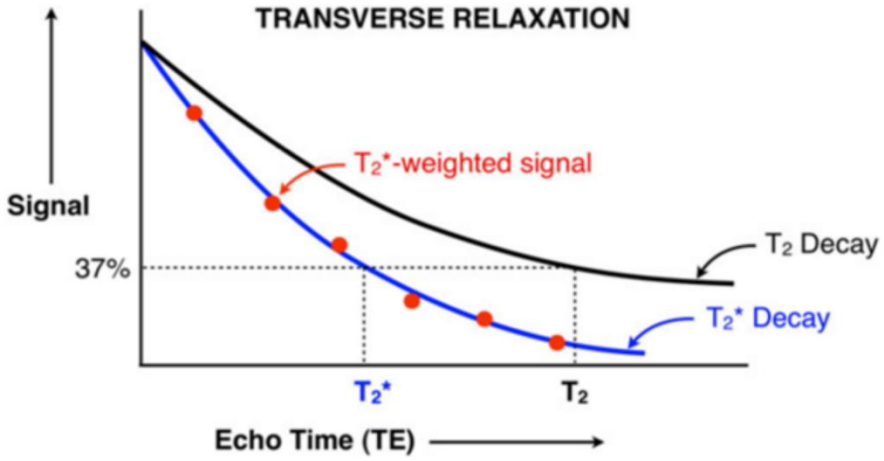

Figure 2-21, From (Cohen-Adad 2014), shows the transverse relaxation decay curves T2 and T_2* as well as an example of experimentals T_2*w values acquired at regular TEs. The T_2* decay curve is obtained by fitting a negative monoexponential curve on T_2*w values while T_2* value of a voxel is defined as being the time value for which the signal is 37% of the maximum signal (at t=0).

2.2.2.3.3 Usefulness

T_2* contrast is known to be sensitive to myelin content in the cortex (Pitt et al. 2010; Cohen-Adad et al. 2011; Mainero et al. 2015), but it is also sensitive to tissue iron level (Lee et al. 2012; Stüber et al. 2014) as well as cortical fibers orientation (Cohen-Adad et al. 2012), blood vessels (Spees et al. 2001) and blood oxygen level (Li et al. 1998). **Figure 2-22** shows a T_2* map zoomed in the cortex as well as two histological maps of myelin content and iron content of the same area. The contribution of both is visible in the T_2* map. But the most beautiful feature in this T_2* map is the high contrast and the level of details revealed in the cortex.

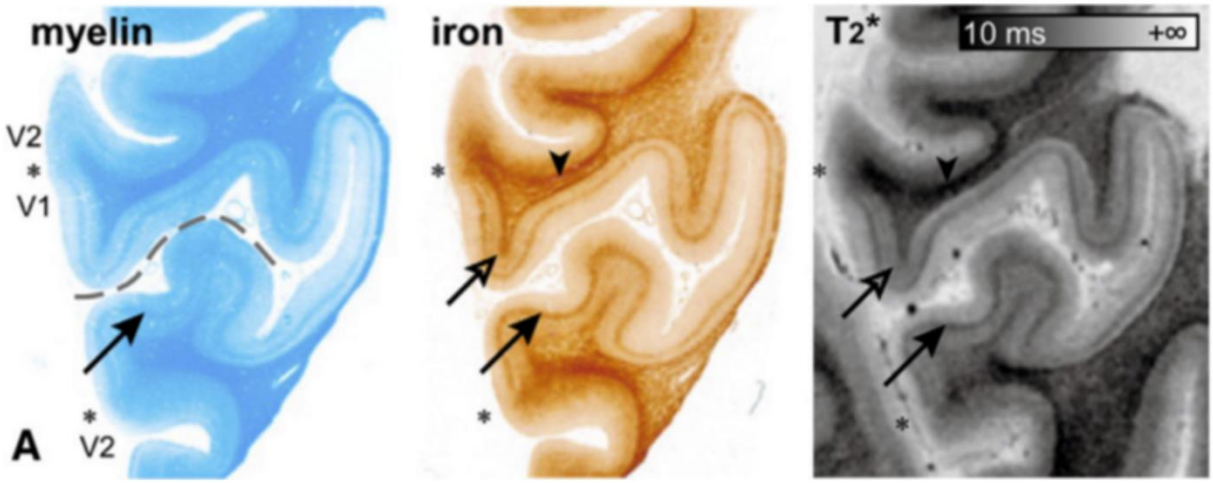

Figure 2-22, From (Cohen-Adad 2014), shows two histological maps of myelin content and iron content of the same cortical area, as well as the corresponding T_2* map acquired at 7T.

2.2.2.4 Combining MTR and T_2*

So far, we saw that MTR and T_2* are two powerful techniques to image features of the cortical gray matter. While they are both already used to study the progression of demyelinating lesions in the cortex of MS patients (Table 2-1 & 2-2), we saw that both techniques are not fully specific to myelin. Because of their divergent physical underlying sources (transfer of magnetisation *vs* inhomogeneous spin dephasing), their confounding factors are not overlapping. Indeed, the specificity of MTR to myelin is mainly confounded by B1 inhomogeneities and others macromolecules, while the specificity of T_2* to myelin is mainly confound by iron and fiber orientation.

Starting from this point we now understand that it is possible to improve the myelin specificity of quantitative cortical maps, which would be relevant for the study *in vivo* of the cortical demyelinating lesions is MS. **Figure 2-23** summarizes the conceptual idea of the myelin extraction from several myelin-sensitive MRI contrasts. The next section presents the mathematical features used to perform this multimodal combination.

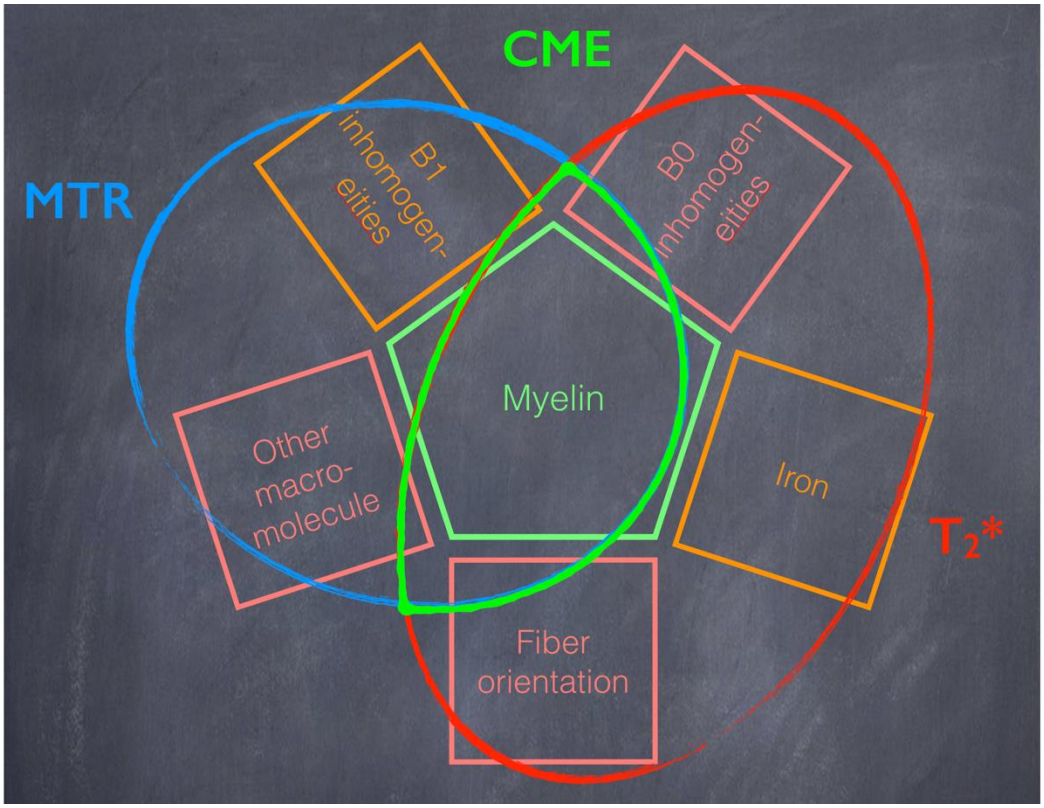

Figure 2-23, simplified concept of myelin extraction from several myelin-sensitive MRI contrasts. As presented in the previous section, MTR and T_2* have both confounding factors hampering their specificity to myelin, but interestingly, their confounding factors are not overlapping. The idea is thus to extract the source of signal shared by both metrics, yielding a better estimator of myelin than when taking each metric separately.

2.3 Mathematical Review

2.3.1 Multimodal combination challenges

The actual multimodal combination framework revealed many practical challenges. For example, mapping the MTR and T_2* values in the cortex is challenging because of its thin and convoluted shape. Moreover, registering both metrics in the same space is not easy because non-linear deformations imply re-interpolation, which can affect T_2* and MTR value, and which is particularly problematic at interfaces (T_2* and MTR are noisy in the CSF). The full combination framework as well as the solutions and discussions about practical challenges are detailed in the

article (SECTION 4). This mathematical review covers two mathematical concepts that deserve a particular attention to better understand the capabilities and the limitation of the myelin extraction framework.

2.3.2 Independent Component Analysis (ICA) principles

2.3.2.1 Principles

Independent Component Analysis is a computational method for separating a multivariate signal into additive subcomponents. ICA finds the independent components (also called latent variables or sources) by maximizing the statistical independence of the estimated components. There are two types of algorithms in the literature which are maximizing the independence either by minimisation of **mutual information** or maximisation of **non-Gaussianity** (Hyvärinen & Oja 2000). I decided to use the *FastICA* algorithm (Hyvärinen & Oja 1999) based on maximisation of non-Gaussianity because of faster computation (cubic convergence), little required memory space and possibility of parallelization (Bingham & Hyvärinen 2000). The principle of sources extraction by maximisation of non-gaussianity is coming from the **Central Limit Theorem** (CLT). Indeed, according to the CLT, the distribution of a sum of independent random variables with finite variance tends towards a gaussian distribution. This means that if we take two random variables, for example the distribution of iron and the distribution of myelin, their sum will have a distribution closer to gaussian that any of the two original variables.

2.3.2.2 Measures of non-gaussianity

Assessing the non-gaussianity of a distribution can be performed by comparing its **kurtosis** or its **negentropy** with those of a gaussian distribution. The kurtosis is a predictor of the shape of a distribution. Mathematically, it represents the **fourth standardized moment**, defined as:

$$Kurt[X] = \frac{\mu_4}{\sigma^4} = \frac{E[(X-\mu)^4]}{(E[(X-\mu)^2])^2}$$

with μ_4 the fourth moment about the mean. The kurtosis of a gaussian distribution is 3. Thus, the estimator defined as *Kurt[X] - 3*, called **excess kurtosis**, is a measure of non-gaussianity. Despite

excess kurtosis is a very intuitive measurement, it has shown very sensitive to outliers (Huber 1985; Hyvärinen & Oja 1999) and its value may depend on only a few observations in the tail of the distribution.

A second measure of the non-gaussianity is given by the negentropy. Negentropy means **negative entropy** and the concept was introduced by Erwin Schrödinger in 1944, in his book *What is Life?* (Schrödinger 1967).

Entropy is a key concept in information theory. The entropy of a random variable can be interpreted as the degree of information that the observation of the variable gives. The more *random* or unpredictable or unstructured the variable is, the larger is the entropy. Mathematically, the entropy *S(X)* of a discrete random variable X is defined as:

$$S(X) = -\sum_i P(X = a_i)\log(P(X = a_i))$$

where a_i are the possible values of *X*. It turns out that the Gaussian distribution is the distribution that maximises the entropy. The Negentropy is thus defined as the difference between the entropy of a gaussian distribution and the entropy of a random variable:

$$J(X) = S(X_{gauss}) - S(X)$$

where X_{gauss} is a Gaussian random variable with the same covariance matrix as *X*. The higher the negentropy, the less Gaussian the random variable *X*. The advantage of using negentropy is that it is the optimal estimator for non-Gaussianity, from statistical point of view (Hyvärinen & Oja 1999). However, estimating negentropy is computationally difficult. Therefore, approximations of negentropy are used in the *FastICA* algorithm in order to reduce the computing time. (Hyvärinen & Oja 1999) demonstrated that a robust approximation of the negentropy can be written as:

$$J(X) \propto [E[G(X) - E[G(N)]]]^2$$

where, N is a Gaussian variable with zero mean and unit variance (i.e. standardized), and *G* is a non-quadratic function such as $x^2, x^3, \tan(ax), or\ x\ e^{-a/x^2}$. One of these four *G* functions has to be chosen in the FastICA algorithm. The choice of *G* will affect the computing time and will not have a significant impact on the result.

2.3.2.3 Simplified algorithm

The FastICA algorithm starts by centering and weighting the data. This means that the input set of data *X* is transformed into a set of data *x* with zero mean, uncorrelated components and variance equal to unity. Then, the determination of the direction of the projection that minimizes gaussianity works as following:

1. Choose an initial weight (direction) vector **w**.
2. Let $\boldsymbol{w}^{+} = E[\boldsymbol{x}G(\boldsymbol{w}^{T}\boldsymbol{x})] - E[G'(\boldsymbol{w}^{T}\boldsymbol{x})]\boldsymbol{w}$
3. Let $w = \boldsymbol{w}^{+}/\|\boldsymbol{w}^{+}\|$
4. If not converged, go back to 2.

Note that the convergence means that the old and new values of $\boldsymbol{w}$ point in the same direction (i.e. their dot products almost equal to 1). The derivation of $\boldsymbol{w}^{+}$ by approximation of negentropy convergence (step 2) is detailed in (Hyvärinen & Oja 1999).

Despite the concept of ICA in very intuitive, the implementation of a fast and robust algorithm is complex and challenging. The FastICA algorithm presented an excellent compromise between robustness of results and computation speed.

2.3.3 Group statistics and ICA normalisation

2.3.3.1 Problem

Group statistics refer to statistics performed between two (in our case) groups, for example, MS patients (MS) *versus* Healthy Controls (HC). Various statistical tests are available to compare two groups, for example, the **Student's t-test** or a **General Linear Model** (GLM). Considering a normal case, we can compute a marker (value) for each subject, for example the mean MTR across the cortex, and use a t-test to see if, based on their mean cortical MTR values, MS can be distinguishable from HC (the only assumption to make being that both distributions of mean values are Gaussian).

However, this kind of group comparison is not feasible when using raw IC (Independent Components) instead of e.g. MTR maps. The problem comes from the fact that the ICA algorithm needs to center and weight the data before finding the ICs. Because ICAs are performed independently for each subject, we lose the information of mean and SD of the recorded signals (i.e. MTR and T_2* maps). Thus, two relative parameters need to be saved in order to restitute the apparent (or relative) mean and standard deviation to the resulting ICs. Otherwise, all MS and HC maps would have a mean of 0 and a SD of 1. Even if the distribution of each individual map is closer to the actual distribution of myelin, we couldn't compare the maps amongst them neither compare MS *vs* HC.

2.3.3.2 Derivation of a solution

An unbiased solution is to use the **relative mean** (Ψ) and the **coefficient of variation** (COV) of each component of the recorded signal (i.e. here MTR and T_2*), and to compute Ψs and COVs of the ICs by using the ICA solution $\boldsymbol{w^T}$. Technically speaking, for one subject's recorded signal, the relative mean Ψ is defined as:

$$\Psi_i = \frac{\mu_i - \mu_{Gi}}{\mu_{Gi}}$$

with *i* representing each recorded signal (i.e. here i = MTR, T_2*). Where, μ_i is the mean of the distribution i of the computed subject, while μ_{Gi} is the mean of the whole group (the mean of the means). (Note that the value of the group mean is not a critical parameter and could even be set as an arbitrary constant as long as the same constant is used for the computation of every subject). So, the relative mean is an information of how far the mean of the subject is, compared to the mean of the group. The COV is defined as follow:

$$COV_i = \frac{\sigma_i}{\mu_i}$$

with *i* representing each recorded signal (i.e. here i = MTR, T_2*), σ_i is the standard deviation of the distribution *i* of the computed subject. The idea is that these parameters are relatives and can thus be compared amongst recorded signals *i*. Now, let's define:

$$\psi = \begin{bmatrix} \Psi_1 \\ \vdots \\ \Psi_n \end{bmatrix}, here, \psi = \begin{bmatrix} \Psi_{MTR} \\ \Psi_{T_2^*} \end{bmatrix}$$

and

$$\zeta = \begin{bmatrix} COV_1 \\ \vdots \\ COV_n \end{bmatrix}, here, \zeta = \begin{bmatrix} COV_{MTR} \\ COV_{T_2^*} \end{bmatrix}$$

So, if $\boldsymbol{w_j}$ is the direction of the j[st] IC,

$$COV_{ICj} = w_j^T \phi$$

and

$$\Phi_{ICj} = w_j^T \zeta$$

and thus, the new group comparable ICs (noted IC') can be recovered as following:

$$IC_j' = IC_j \frac{w_j^T \zeta}{50(1 + w_j^T \phi)} + 50(1 + w_j^T \phi)$$

Where, *j=[1, ..., k]* with *k* the number of ICs if interest. The factor 50 is arbitrary. It means that the average amongst all distributions IC' will have a mean of 50.

This processing fixes the problem of normalisation or centralisation of data imposed by multivariate processing methods. Group comparable ICs are essential to keep the quantitative aspect of resulting maps and thus to be able to perform group statistics such as t-test or GLM.

CHAPTER 3 METODOLOGY

3.1 Approach of the problem

A careful review of the literature revealed three points: i) MTR and T_2* are amongst the most efficient MR modalities to study the cortical pathology of MS patients. ii) Both metrics lack specificity when used to assess cortical demyelination. iii) No model aiming to combine MR modalities using an ICA-based approach was proposed in the literature.

Hence, the idea was to develop a novel approach to combine MTR and T_2* modalities acquired in the *in-vivo* human cortex. The goal being to obtain a metric more specific to myelin, that could be used to study the cortical demyelination of MS patients.

Firstly, the feasibility and the relevance of combining MTR and T_2* was investigated. Then, an approach based on the principle of signal decomposition using minimization of gaussianity was developed. The framework pre-processing includes a normalisation, a first order correction to partial volume effect and a correction to tissue orientation with respect with B_0. The gain in myelin specificity of the extracted components has been validated using simulations and previous histology works. In a second time, the method was applied on MS patients in order to study their cortical variations of myeloarchitecture. Two groups of MS patients have been studied with the above method. A *classic* cohort and an *early* cohort (disease duration < 3years), MS vs HC numbers were respectively 6 HC vs 11 MS and 5 HC vs 10 MS.

3.2 Publications resulting from this mémoire

Researches conducted along this Mémoire led to several publications, notably one in a high impact factor journal (Neuroimage, IF=6.357). Steps of this project have also been presented in the following international and local conferences/symposiums:

- *22nd annual meeting of International Society for Magnetic Resonance in Medicine*, Milan, Italy, June 2014. Poster #1783
- *13e journée de la recherche, Polytechnique Montreal,* Montreal, Canada, Mai 2015.

- *23nd annual meeting of International Society for Magnetic Resonance in Medicine,* Toronto, Canada, June 2015. Presentation #0823
- 31st *annual meeting of European Committee for Treatment and Research in Multiple Sclerosis, Barcelona, Spain, October 2015. Poster #957*
- *7st journée scientifique du Réseau de Bio-Imagerie du Québec,* Montreal, Canada, January 2016.
- *24nd annual meeting of International Society for Magnetic Resonance in Medicine,* Singapore, Mai 2016. Presentation #237

The next section presents the content of these publications and their coherence along with the scientific goals of this Memoire.

3.3 Coherence between publications

As mentioned previously, the choice of the MR modalities to be combined was first based on previous literature review demonstrating the potential of both metrics to image myelin in the cortex. Then, a deeper analysis of i) the mechanisms of both modalities, ii) their respective behaviour in the cortex iii) their mutual interplay in various cortical areas, was performed to ensure the quality of the future combination. This preliminary work led to a presentation of a poster at the conference ISMRM 2014. This poster was entitled: *Comparison between 7T* T_2* *and 3T MTR in the in vivo human cortex.*, presented in CHAPTER 5.

Once the relevance of the combination demonstrated, several ideas and algorithms were tested to effectively extract the main information of myelin contained in both modalities. An ICA-based algorithm was revealed to be the best compromise between robustness, reproducibility and calculus time. Following the development of the combination framework, and its validations, a scientific article was published in the journal NeuroImage: *Multivariate combination of magnetization transfer,* T_2* *and* B_0 *orientation to study the myelo-architecture of the in vivo human cortex.*, presented in CHAPTER 4.

This new tool being available, its application to study MS patients could start. A first study comparing the ability of the combined metric to detect cortical demyelination relatively to standard metrics was performed. It resulted in a presentation at the conference ISMRM 2015: *Multivariate*

combination of magnetization transfer ratio and quantitative T_2* *to detect subpial demyelination in multiple sclerosis.*, presented in CHAPTER 6.

As this study revealed the benefits of the combined metric to study MS patients, a second study was performed in a cohort of early MS patients, for whom the cortical demyelination is more subtle. This study was presented at the conference ECTRIMS 2015: *Multivariate combination of quantitative* T_2* *and* T_1 *at 7T MRI detects in vivo subpial demyelination in the early stages of MS., presented in CHAPTER 6.*

CHAPTER 4 ARTICLE 1: MULTIVARIATE COMBINATION OF MAGNETIZATION TRANSFER, T_2* AND B_0 ORIENTATION TO STUDY THE MYELO-ARCHITECTURE OF THE IN-VIVO HUMAN CORTEX

This article presents the combination framework, from its development details to its validation. Please note that the Tables and Figures will have the suffix 4- (i,.e. CHAPTER 4) before their actual number, because the document formmating had to be respected.

doi : 10.1016/j.neuroimage.2015.06.033

Authors:

G. Mangeat [1,3], S. T. Govindarajan [3], C. Mainero [3,4], J. Cohen-Adad [1,2]

Affiliations:

[1] Institute of Biomedical Engineering, Polytechnique Montreal, Montreal, QC, Canada

[2] Functional Neuroimaging Unit, CRIUGM, Université de Montréal, Montreal, QC, Canada

[3] Athinoula A. Martinos Center for Biomedical Imaging, MGH, Charlestown, MA, USA

[4] Harvard Medical School, Boston, MA, USA

4.1 Abstract

Recently, T_2* imaging at 7 tesla (T) MRI was shown to reveal microstructural features of the cortical myeloarchitecture thanks to an increase in contrast-to-noise ratio. However, several confounds hamper the specificity of T_2* measures (iron content, blood vessels, tissues orientation). Another metric, magnetization transfer ratio (MTR), is known to also be sensitive to myelin content and thus would be an excellent complementary measure because its underlying contrast mechanisms are different than that from T_2*. The goal of this study was thus to combine MTR and T_2* using multivariate statistics in order to gain insights into cortical myelin content.

Seven healthy subjects were scanned at 7T and 3T to obtain T_2* and MTR data, respectively. A multivariate myelin estimation model (MMEM) was developed, and consists in (i) normalizing T_2* and MTR values and (ii) extracting their shared information using independent component analysis (ICA). B_0 orientation dependence and cortical thickness were also computed and included in the model.

Results showed high correlation between MTR and T_2* in the whole cortex ($r=0.76$, $p<10^{-16}$), suggesting that both metrics are partly driven by a common source of contrast, here assumed to be the myelin. Average MTR and T_2* were respectively 31.0 +/- 0.3% and 32.1 +/- 1.4 ms. Results of the MMEM spatial distribution showed similar trends to that from histological work stained for myelin ($r=0.77$, $p<0.01$). Significant right-left differences were detected in the primary motor cortex ($p<0.05$), the posterior cingulate cortex ($p<0.05$) and the visual cortex ($p<0.05$).

This study demonstrates that MTR and T_2* are highly correlated in the cortex. The combination of MTR, T_2*, CT and B_0 orientation may be a useful means to study cortical myeloarchitecture with more specificity than using any of the individual methods. The MMEM framework is extendable to other contrasts such as T_1 and diffusion MRI.

Keywords: | MTR | T_2* | B_0 orientation | myeloarchitecture | ICA | Brodmann

4.2 Introduction

Myeloarchitecture refers to the spatial organization of myelinated fiber in the central nervous system, including features such as their size, density orientation, and myelination (Flechsig, 1920; Vogt, 1911). The study of myeloarchitecture in the *in vivo* human cortex can provide further elements about the organization of the healthy and pathological cortex.

Previous studies have shown that T_2* magnitude and phase images can reveal exquisite details of cortical microstructure, with enhanced contrast at ultra-high field strength (Duyn et al., 2007; Li et al., 2009, 2006). T_2* is the effective transverse relaxation and is driven by microscopic and macroscopic field inhomogeneities, e.g. caused by susceptibility differences between tissues (Cohen-Adad, 2014). Of interest, T_2* contrast is notably influenced by the size, density and orientation of myelinated fibers (Hwang et al., 2010; Lee et al., 2012; Pitt et al., 2010). Surface-based analysis of T_2* revealed several features that correlate with myelin distribution in the cortex (Cohen-Adad et al., 2012, 2011; Deistung et al., 2013; Mainero et al., 2012). Similar observations were obtained from T_1 (Dinse et al., 2013) and T_1w/T_2w (Glasser and Van Essen, 2011) measurements, further confirming the influence of myelin on T_2* contrast. Despite its sensitivity to myeloarchitecture, T_2* it is influenced by several confounds, such as the tissues iron level (Fukunaga et al., 2010), B_0 field inhomogeneities (Hernando et al., 2012) and fibers orientation with respect to B_0 (Cohen-Adad et al., 2012). Hence, combining T_2* with another measure sensitive to myelin would increase the confidence in assessing the degree of myelination, as has been shown *ex vivo* (Tardif et al., 2012).

Magnetization Transfer (MT) imaging was shown to be sensitive to myelin content (Levesque and Pike, 2009; Schmierer et al., 2004) in white matter (WM) and thus would be an excellent complementary measure because its underlying contrast mechanisms are different than that from T_2*. The MT effect results from the interaction between two kinds of hydrogen nucleus: protons in a liquid state associated with water molecules and protons in semisolid state associated with macromolecules. The macromolecular spins can be saturated by an off-resonance radio frequency (RF) pulse because they have a much broader absorption lineshape than the liquid spins. The preferential saturation of the macromolecular spins can be transferred to the liquid spins, depending on the rate of exchange (Levesque and Pike, 2009). This water spin saturation can then be detected with MRI (Henkelman et al., 2001). MTR is an index calculated using images with and

without MT saturation pulse and was shown to correlate with myelin content (Henkelman et al., 2001; Schmierer et al., 2004). Recently, MTR was mapped in the cortex of MS patients (Chen et al., 2013; Derakhshan et al., 2014) and showed similarities between myelinated regions and high MTR values. However, MTR is only a semi-quantitative metric as it depends on sequence parameters, B1 profile and T_1 relaxation (Berry et al., 1999; Pike Bruce, 1996).

Combining MTR with T_2* thus appears to be a useful means to gain insight into cortical myelination because these two metrics are sensitive to myelin content but are based on different biophysical phenomena. MTR increases with myelin and T_2* decreases with myelin.

However, mapping T_2* and MTR in the cortex is challenging because the cortical ribbon is thin, highly convoluted and its geometry varies across individuals. Cortical surface-based analysis allows robust visualization of MRI measurements across the entire cortex and enables the calculation of spatial statistics at a population scale (Dale et al., 1999; Derakhshan et al., 2014; Fischl, 2012; Fischl et al., 1999; Glasser and Van Essen, 2011). Other confounds exist that can affect cortical mapping studies. Namely, (i) the effect of cortical thickness, which can introduce variable amount of partial volume effect and (ii) the angle between coherently-oriented myelinated fibers in the cortex and the direction of the main magnetic field (B_0) (Cohen-Adad et al., 2012). Multivariate statistics, such as Independent Component Analysis (ICA) can decompose multivariate signal into independent signals coming from independent sources (Bingham and Hyvärinen, 2000; Hyvärinen and Oja, 2000; Xie and Wu, 2006). Here, ICA would be an adequate candidate for probing the existence of shared information between T_2*- and MTR-derived signal related to myelin content, while taking into account confounding factors (thickness, B_0 orientation).

The goals of the present study were: (*i*) to map T_2* at 7T and MTR at 3T in the healthy *in vivo* human cortex using surface-based analysis and (*ii*) to combine T_2* and MTR using a multivariate model in order to extract the shared information related to myelin.

4.3 Material and Methods

4.3.1 Data acquisition

Healthy subjects (N=7, gender = 4F and 3M, age = 36 +/- 5 years) were recruited. Subjects were scanned with a 7T whole-body scanner (Siemens Healthcare, Erlangen, Germany) to measure T_2* and with a 3T scanner (Siemens TIM Trio) to measure MTR. We chose not to perform the MTR protocol at 7T due to the less homogeneous B1 profile and SAR limitations. Both scanners were equipped with a 32-channel coil. Parameters values at 7T were: 2D gradient-echo, TR = 2020 ms, TE = 6.34+3.2n [n=0,...,11] ms, resolution = 0.33x0.33x1 mm^3, acquisition time (TA) was 20 min (10 min/slab * 2 slab). Parameters for the 3T magnetization transfer contrast were: Spoiled gradient echo sequence: 3D FLASH (Fast Low-Angle Shot), TR/TE = 30/2.49 ms, matrix = 192x192, resolution = 1.2x1.2x1.2 mm3, with (*mt_on*) and without (*mt_off*) MT pulse. The MT pulse is a Gaussian envelope with pulse duration = 9984μs and frequency offset = 1200 Hz. The acquisition time (TA) of each FLASH volume was 7:45 min. In addition to the MTR protocol, a T_1-weighted image was acquired at 3T for cortical surface reconstruction using a magnetization-prepared rapid acquisition with multiple gradient echoes (MEMPR) (van der Kouwe et al., 2008). Parameters were: TR/TI=2530/1200 ms, TE=[1.7, 3.6, 5.4, 7.3] ms, flip angle (α)=7°, FOV=230×230 mm2, resolution=0.9×0.9×0.9 mm3, bandwidth=651 Hz/pixel, scan time=6.5min. The reason for doing surface reconstruction from 3T data is that this protocol has been thoroughly validated (Dale et al., 1999; Govindarajan et al., 2014; Postelnicu et al., 2009; van der Kouwe et al., 2008), in comparison with the 7T MEMPR protocol, from which the less homogeneous B1+ profile can produce errors in segmentations.

4.3.2 Data processing

Figure 1 shows an overview of the data processing pipeline. Pre-processing steps included: (i) computing MTR and T_2*. (ii) registering MTR and T_2* volumes to the cortical surface model, (iii) sampling the obtained values within the cortex, (iv) calculate the cortical thickness and (v) computing the angle between B_0 field and the vector normal to the cortical surface. Processing was done with FreeSurfer (http://surfer.nmr.mgh.harvard.edu) and custom-made scripts written in MATLAB.

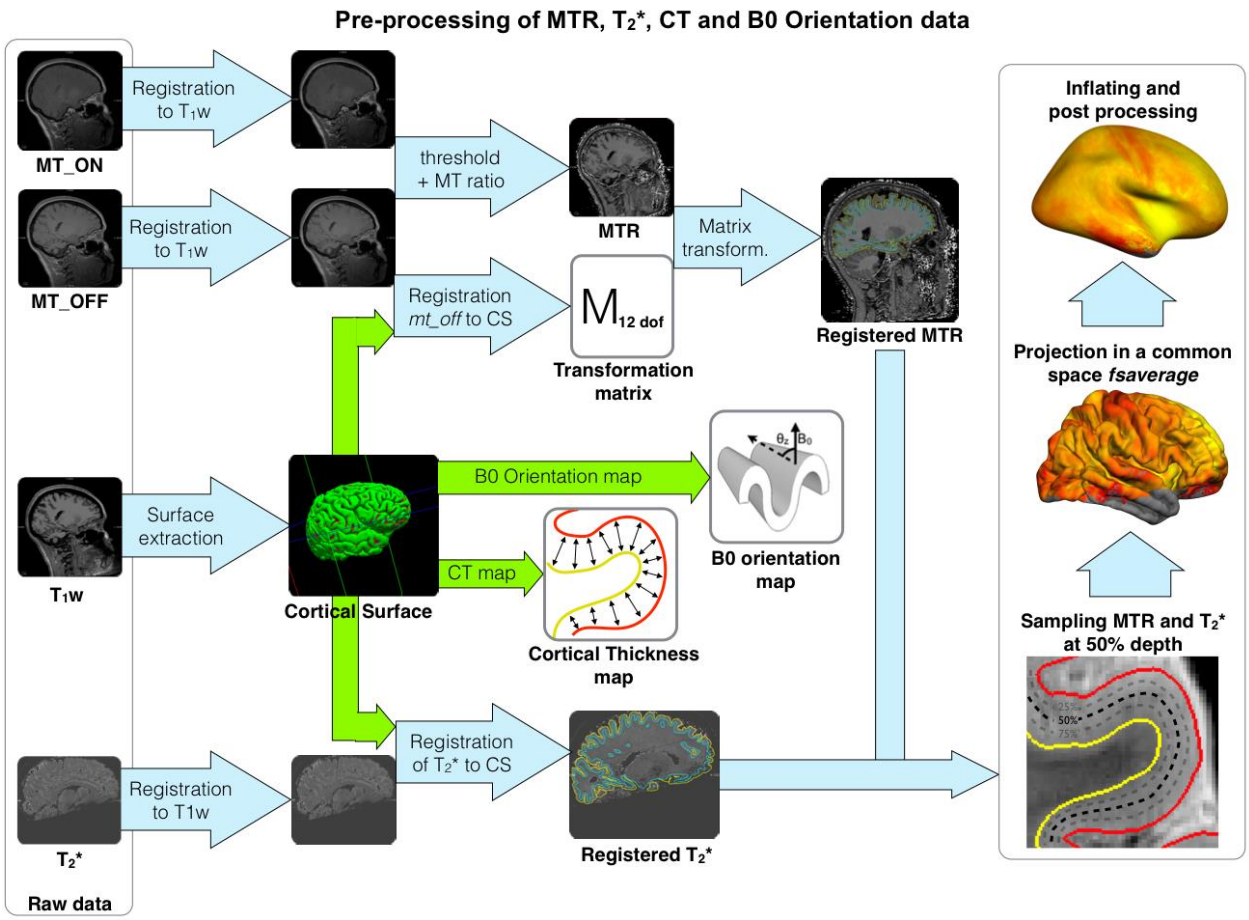

Figure 4-1**.** Pre-processing framework. The cortical surface was extracted with freesurfer from an anatomical T_1-weighted volume. MT data: *mt_on* and *mt_off* volumes were registered to the T_1-w volume (Reuter et al., 2010), then the MT ratio (MTR) was computed. *mt_off* was registered to the cortical surface (CS) using boundary based registration technique (12 d.o.f.) (Greve and Fischl, 2009). The transformation matrix of the registration was applied to the MTR volume. T_2* volume was registered to the T_1-w volume using header information. Then, T_2* volume was registered to the cortical surface using boundary based registration (9 d.o.f.). MTR and T_2* cortical maps were computed at each vertex along the mid-cortical surface. Cortical thickness map was acquired by computing the distance between white and pial surfaces for each vertex. B_0 orientation map was computed from the angle between the normal of the cortical surface and the orientation of the B_0 field. Lastly, the four metrics (T_2*, MTR, cortical thickness and B_0 orientation) were projected to a common space (*fsaverage*) using a spherical averaging procedure (FreeSurfer).

T_2* data were first corrected for background inhomogeneities as described in (Cohen-Adad et al., 2012), then T_2* was estimated using monoexponential fitting. A gross alignment was first performed between the averaged first 4 echoes of the T_2*-weighted volume and the T_1weighted volume (at 3T) following the protocol described in (Govindarajan et al., 2014) Then, a fine alignment of the T_2*-weighted volume to the surface was estimated using the boundary-based registration method (BBR, 9 degrees of freedom), which is based on the local intensity gradient and was shown to have high robustness and accuracy (Greve and Fischl, 2009). Then, the registration matrices were applied to the T_2* volume. More details can be found in (Cohen-Adad, 2014). All registrations were visually inspected. For pre-processing of MTR data, both volumes with (*mt_on*) and without (*mt_off*) the Gaussian MT pulse were registered to the 3T T_1-weighted volume using the function *mri_robust_register* available in FreeSurfer (Reuter et al., 2010). The *mt_off* volume was registered to the surface using bbregister (12 d.o.f.). The resulting affine matrix was then applied to the MTR volume. Once both mt_on and mt_off were registered to the cortical surface, MTR was computed as follows:

$$MTR = 100 * \frac{mt\_off - mt\_on}{mt\_off} \quad (1)$$

Figure 1 shows the MTR registrations steps. Once registered to the individual surface, MTR and T_2* were sampled at the mid distance between the pial and the white matter surface (50% depth) as done in (Cohen-Adad, 2014). The mid-cortical distance was chosen in order to minimize partial volume effect. Cortical thickness (CT) map was calculated using the normal distance between both pial and white matter surfaces previously segmented by *freesurfer*. B_0 orientation dependence was estimated using the angle θ_z between the normal vector of the surface and the B_0 field direction (Cohen-Adad et al., 2012). MTR, T_2*, CT and B_0 orientation data were then spatially normalized to the existing common space (fsaverage) available in FreeSurfer V4.2. Spatial normalization was performed using a spherical averaging procedure as described in (Fischl et al., 1999). For each subject, the cortical manifold was projected onto the target surface (fsaverage) and assigned a normal vector field with a consistent orientation.

Mean and inter-subject standard deviation (SD) maps were calculated for MTR, T_2*, CT and B_0 orientation. Then, Pearson's coefficient was calculated vertex-wise between each pair of the following parameters: MTR, T_2*, CT and B_0 orientation.

4.3.3 Multivariate Myelin Estimation Model (MMEM)

Here we propose a method to merge the myelin-related information contained in MTR and T_2* into a single metric. The framework works as follows: Firstly, multilinear regressions were performed using predictors of myelin content (MTR and T_2*) and confounding covariates (cortical thickness, which can introduce variable amount of partial volume effect, and B_0 orientation dependency). Secondly, independent component analysis (ICA) is used to combine MTR- and T_2*-derived signal related to myelin.

The detailed steps of the MMEM are represented in Figure 2. Firstly, two maps were estimated using multi-linear regressions: one using the regressors MTR, CT and B_0 orientation (ME_MTR) and one using the regressors T_2*, CT and B_0 orientation (ME_T_2*). ME_MTR and ME_T_2* maps respectively represent MTR and T_2* values corrected for partial volume effect and fibers orientation. Notice that constant regressors such as age and gender were in the constant term of the regression because the MMEM was performed independently for each subjects and the resulting map was normalized under a common dynamic range (explained below). ME_MTR and ME_T_2* maps were calculated using equations (2) and (3):

$$ME\_MTR = a_1 + b_1 MTR + c_1 CT + d_1 sin(2\theta_z) + e_1 cos(2\theta_z) \quad (2)$$

$$ME\_T_2^* = a_2 + b_2 T_2^* + c_2 CT + d_2 sin(2\theta_z) + e_2 cos(2\theta_z) \quad (3)$$

where *a*, *b*, *c*, *d* and *e* are the resulting parameters of the multilinear regressions. θ_z is the angle between the surface's normal vector and the B_0 magnetic field direction. The estimation of B_0 orientation dependency was based on the model presented in (Cohen-Adad et al., 2012; Lee et al., 2011) but rearranged in a linear form to be used in a linear regression. More specifically, the sine function from the orientation dependency model was broken down into a linear sum of sine and cosine (see equation 1,2 and Supplementary Material S1 for the whole derivation). In order to merge MTR and T_2* within the same framework, both linear regressions were performed with a common dependent variable. This dependent variable was a binary map made of regions that are known to be highly (BA1, BA4 and BA42) and poorly myelinated (BA8 and BA9) (Annese et al., 2004; Glasser and Van Essen, 2011; Glasser et al., 2014; Laule et al., 2008; Nieuwenhuys, 2013; Vogt, 1911). BA3 was not considered because of the thinness of the cortex in this region (mean CT=1.8mm) and hence strongly hampered by partial volume effect. The regions of high and low myelin content were arbitrarily set to 70% and 30%. It is however important to keep in mind that

these arbitrary values were only chosen for adjusting the dynamics of both metrics (i.e. ME_MTR and ME_T_2*), on a subject-by-subject basis, in order to explore the relative distribution of myelin-related values throughout the entire cortical ribbon. Secondly, the shared information between ME_MTR and ME_T_2* was extracted using ICA decomposition, for each subject. ICA was chosen because (i) it is an unsupervised data-driven algorithm and is therefore free from arbitrary priors, (ii) it outputs mathematically independent components (as opposed to PCA) and (iii) the 'so-called' first component represents the shared information from ME_MTR and ME_T_2* with the highest variance, which is assumed to represent myelin. This assumption is based on previous studies demonstrating the sensitivity of T_2* and MTR to myelin content (Cohen-Adad et al., 2011; Deistung et al., 2013; Levesque and Pike, 2009; Mainero et al., 2012; Schmierer et al., 2004). The hypothesis being that the first component of the ICA was a more specific indicator for myelin content than a single metric taken separately. This hypothesis was further confirmed by simulations (see Supplementary Material S2) and comparison with previous histology works (Braitenberg 1962). The final multivariate myelin estimation was calculated from the principal independent vector of the ICA's separating matrix (V_1) and the matrix (X) containing ME_MTR and ME_T_2* data (equation 4). This map was named Combined Myelin Estimation (*CME*).

$$CME = {V_1}^T * X \quad (4)$$

The robustness of the ICA decomposition was qualitatively checked for each subject by plotting the ICA's vectors on the original set of data. The ICA's first component map was then computed for each subject separately. Lastly, the ICA's first component map were averaged across subjects.

The PALS-B12 Brodmann atlas (Van Essen, 2005) was used for interrogating sub-region of the cortex defined by their cyto-architecture. This choice was driven by previous studies showing homogenous myeloarchitecture within functional areas (Abdollahi et al., 2014; Bock et al., 2009; Geyer and Turner, 2013; Glasser and Van Essen, 2011; Glasser et al., 2014; Nieuwenhuys, 2013; Sereno, 1991).

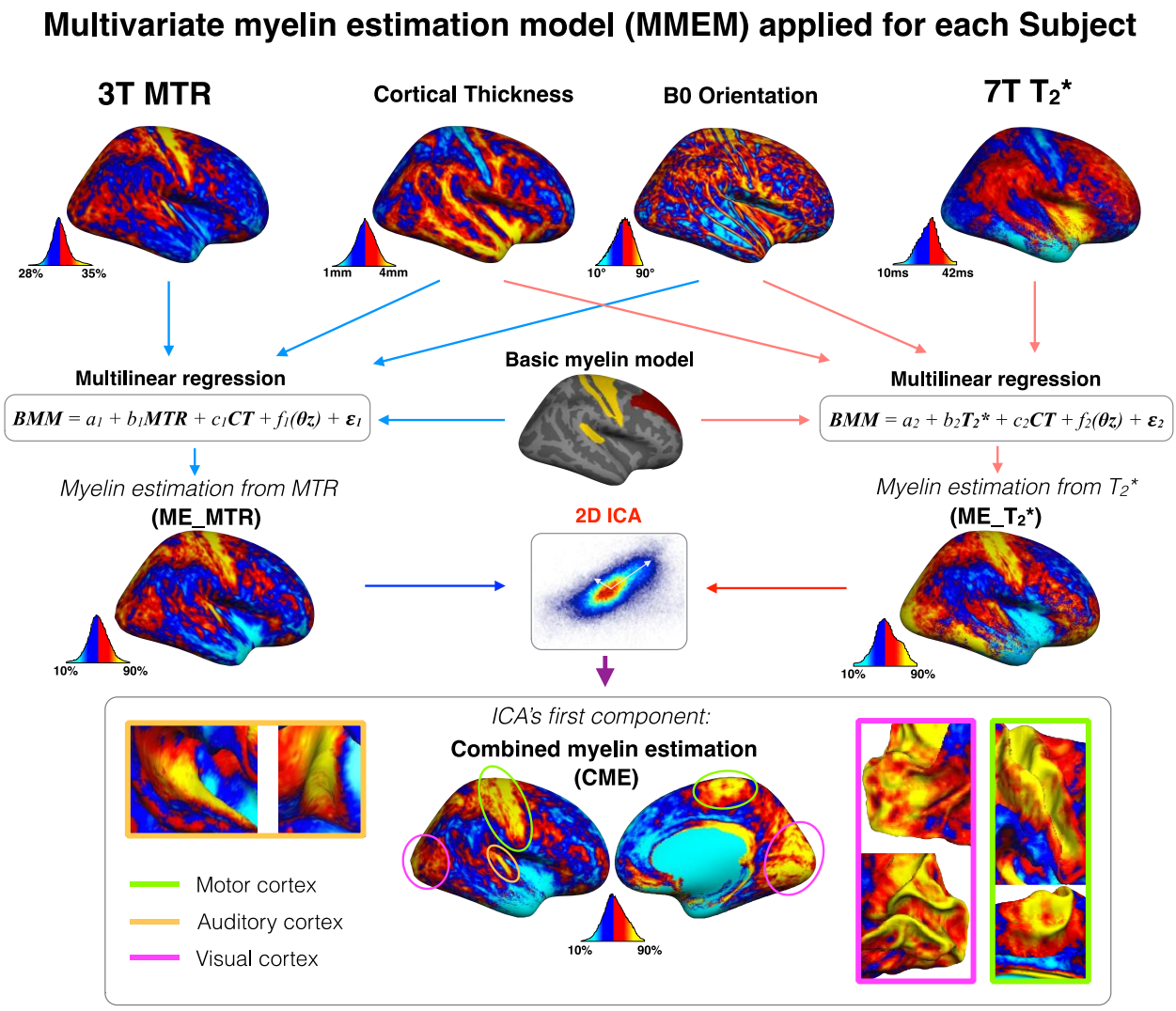

Figure 4-2**.** Multivariate myelin estimation model (MMEM). MMEM aimed to estimate a cortical myelin map using MTR, T_2*, cortical thickness (CT) and B_0 orientation maps. The MMEM was divided into two steps. Firstly, two maps were estimated using multi-linear regressions: one using MTR, CT and B_0 orientation (ME_MTR) and one using T_2*, CT and B_0 orientation (ME_T_2*). ME_MTR and ME_T_2* maps represent myelin-correlated values corrected for partial volume effect and fibers orientation. In order to merge MTR and T_2* within the same framework, both linear regressions were performed with a common dependent variable (BMM). Secondly, the shared information between ME_MTR and ME_T_2* was extracted using ICA decomposition, for each subject. The ICA decomposed the signal into two component that are mathematically independent. The 'so-called' first component of the ICA was the source that share the highest

variance between ME_MTR and ME_T_2*. The hypothesis being that the first component of the ICA was an indicator for myelin content.

4.4 Results

4.4.1 MTR, T_2*, CT and B_0 orientation mapping

MT and T_2* data were successfully acquired in 6 out of 7 subjects. Visual inspection revealed excessive motion in one subject for the MT data. Hence only 6 subjects were used for subsequent analyses.

Figure 3A shows maps of 3T MTR, 7T T_2*, CT and B_0 orientation averaged across subjects. MTR map shows high values (>32%) notably in the primary motor cortex (BA4), in the primary somatosensory cortex (BA1, BA2 & BA3), in the somatosensory association cortex (BA5 & BA7), in the posterior cingulate cortex (BA31 & BA23), in the visual cortex (BA17, BA18 & BA19) and in the auditory cortex (BA42). However, some 'strip' patterns of lower MTR are observed in these regions, notably in the central sulcus (~BA3) and in the calcarine fissure. The CT map also highlights a 'strip' pattern in BA3 and shows some regions of low cortical thickness (< 2mm) around the calcarine sulcus. These regions are also highlighted by the CT map by showing thin cortical thickness (between 1 and 2mm). In the frontal cortex MTR is notably low. T_2* map shows an overall similar pattern but with an opposite tendency. Low values (<25ms) are visible in the primary motor cortex, the primary somatosensory cortex and in the visual cortex whereas T_2* is high (~35ms) in the frontal lobe. The CT map shows lower cortical thickness in BA3, BA17 and BA18 as previously shown (Clarkson et al., 2011; Cohen-Adad et al., 2012).

Figure 3B shows maps of SD across subjects for the respective metrics. MTR SD is fairly homogenous and small in the whole cortex (~1.5%). T_2* SD also exhibits fairly small values across the cortex (~2.5ms), however extreme values are found in the lower brain region, likely due to inhomogeneous B_0 field at 7T. These fairly small SD maps for MTR and T_2* suggest that the two metrics have centered and narrow distributions across subjects and hence the averaged maps are representative of the population studied here. Cortical thickness SD and B_0 orientation SD were fairly large on a voxel-by-voxel basis (average SD was respectively 0.47mm and 17.4°), suggesting

that there is an inter-subject variability in the morphology of the cortex, e.g., thickness, location and orientation of different gyri/sulci.

Table 1 summarizes the whole brain statistics (mean, inter subject SD and coefficient of variation (COV)). COV coefficients are calculated by performing the ratio between the inter-subjects SD and the mean across the whole cortex. COV are displayed percentage. Inter-subject SD and COV are fairly small for all metrics as previously seen on the maps.

Table 4-1. Mean, inter-subject SD and coefficient of variation (COV) of MTR, T_2* and CT maps. Left and Right tables are showing results for left (LH) and right (RH) hemispheres respectively.

LH	MTR [%]	T_2* [ms]	CT [mm]		RH	MTR [%]	T_2* [ms]	CT [mm]
Mean	31.04	32.16	2.61		Mean	31.02	32.03	2.60
SD	0.34	1.42	0.053		SD	0.41	1.39	0.061
COV [%]	1.1	4.4	2.0		COV [%]	1.3	4.3	2.3

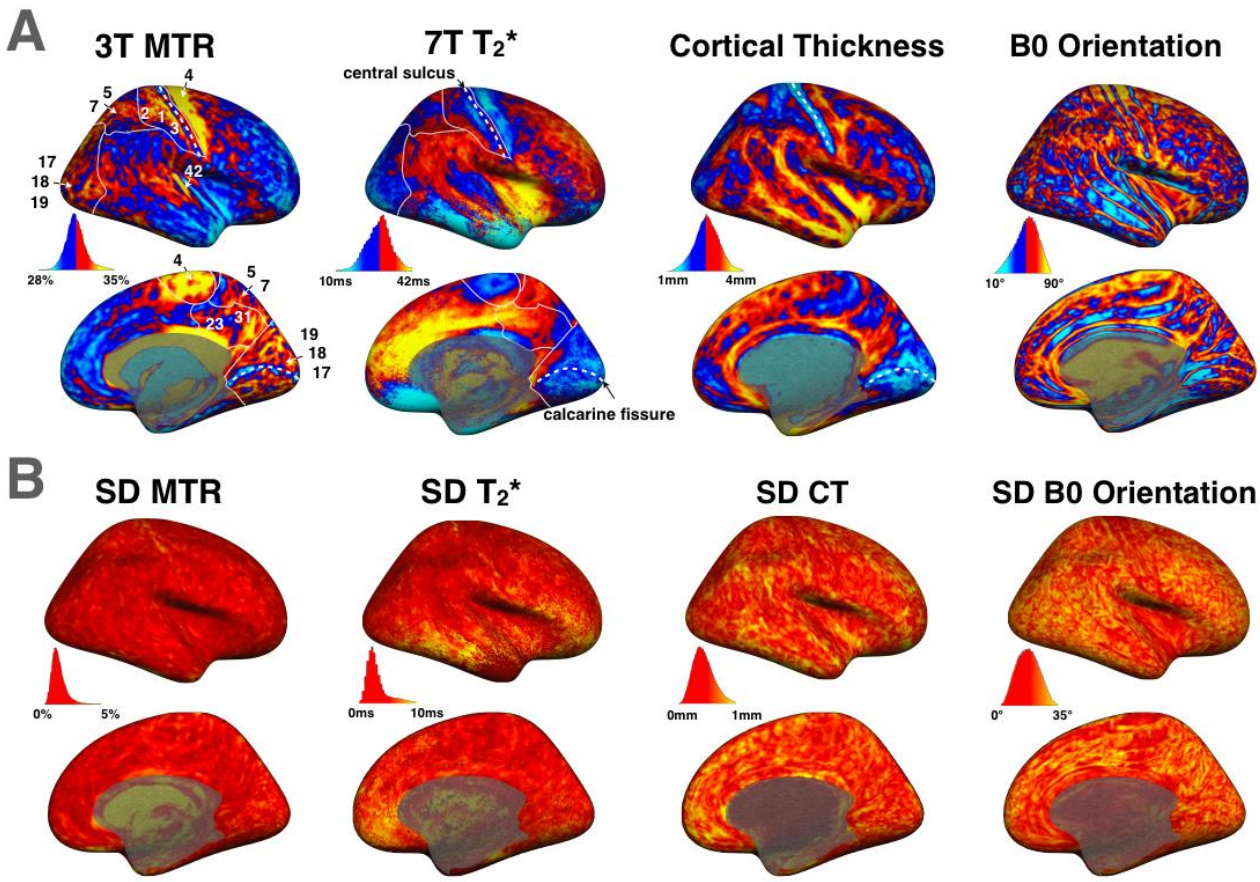

Figure 4-3**. (A)** Maps averaged across subjects of MTR, T_2*, cortical thickness (CT) and B_0 orientation. In MTR and T_2* maps, white lines are showing the borders of the primary somatosensory cortex (BA1, BA2 & BA3), the somatosensory association cortex (BA5 & BA7), the posterior cingulate cortex (BA31 & BA23) and the visual cortex (BA17, BA18 & BA19). Arrow are also showing the primary motor cortex (BA4) and the primary auditory cortex (BA42). White dashed lines are showing the central sulcus and the calcarine fissure. The colormap was thresholded (mid-value of each distribution) to enhance its dynamic. For un-thresholded maps, see Supplementary Material S4. **(B)** Maps of the standard deviation across subjects for MTR, T_2*, CT and B_0 orientation.

4.4.2 Pearson's correlations between MTR and T_2*

Figure 4 shows the Pearson's correlations between MTR and T_2*. Different colors are showing the vertices density in order to better visualize scatter's shape. To reduce the high-

frequency noise in the correlation space (MTR vs. T_2*) a 2-dimensional smoothing of 10 points was achieved before computing the Pearson's correlation. Strong correlations were observed in the right (r=-0.77) and left (r=-0.75) hemispheres. The colormap reveals higher density in the center of the scatter showing a 2D Gaussian tendency well defined at the center of the distributions.

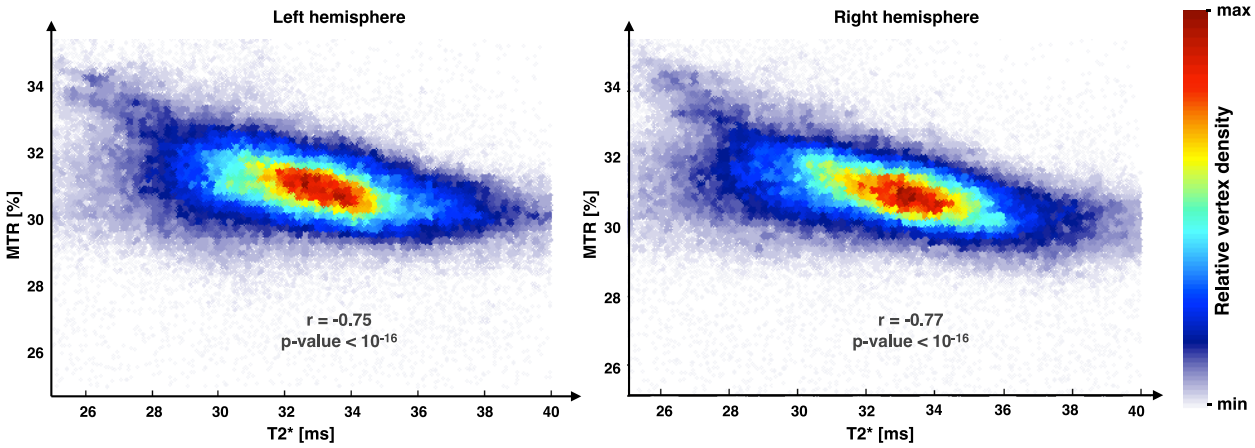

Figure 4-4**.** Pearson's correlations between MTR and T_2* maps averaged across subjects. Strong correlations were observed in right (r = -0.77) and left (r = -0.75) hemispheres. The colormap shows the data-point density in the scatter and suggest a 2D Gaussian tendency well defined in the center of the distribution.

We also assessed the whole cortex correlation between T_2* & CT ; T_2* & B_0 orientation ; MTR & CT and MTR & B_0 orientation. Table 2 shows their corresponding Pearson's correlation coefficient. We can see that in the whole cortex, correlations with B_0 orientation are fairly low.

Table 4-2**.** Pearson's coefficient calculated vertex-wise between each pair of the following parameters: MTR, T_2*, CT and B_0 orientation for left (LH) and right (RH) hemispheres.

LH	**Thickness**	B_0 **orientation**		**RH**	**Thickness**	B_0 **orientation**
MTR	r = -0.19 $p < 10^{-16}$	r = 0.18 $p < 10^{-16}$		**MTR**	r = -0.24 $p < 10^{-16}$	r = 0.14 $p < 10^{-16}$
T_2*	r = 0.52 $p < 10^{-16}$	r = -0.13 $p < 10^{-16}$		**T_2***	r = 0.42 $p < 10^{-16}$	r = -0.05 $p < 10^{-8}$

4.4.3 Distribution graph

The distribution graph (Figure 5) is a qualitative way to visualize spatial correlations between MTR, T_2*, CT and B_0 orientation for assessing the feasibility to combine these four metrics using a linear model (first step of the MMEM). First, we compared the shape of MTR, T_2*, CT and B_0 orientation across all 164,000 vertices. Vertices of the mean T_2* map (in red) were sorted in the ascending order. The same index distribution was then used to display MTR (blue), CT (magenta) and B_0 orientation (green) values. For clarity, values were smoothed along the abscissa (100-point window). Inter subjects SD have also been plotted for each vertex. We chose to sort T_2* values instead of MTR due to the larger number of artefactual vertices in the T_2* data, leading to extremely low or high values, related to field inhomogeneity and/or surface registration (Cohen-Adad, 2014). Only the right hemisphere values are plotted for more clarity. Similar trends are observed between left and right hemispheres.

In order to further explore the different trends between metrics, the distribution graph was divided into four ensembles of vertices:

- Region 1 (light blue on figure 5): Vertices hampered by strong artifacts on T_2* data caused by signal dropout (T_2*<24ms). This region contains less than 2% of all cortical vertices.
- Region 2 (dark blue): Vertices for which MTR and T_2* are correlated. Interestingly, these vertices are mainly located in the gyri adjacent to the central sulcus and the calcarine fissure. There are some dark blue areas that neighbor light blue areas in the lower brain region, and these vertices are likely affected by artifacts due to poor shimming in this region. However, we believe that the same pattern observed in other vertices (e.g., visual and motor cortex) is genuine. This region contains less than 2% of all vertices.
- Region 3 (yellow): Vertices where MTR and T_2* are anti-correlated (R-squared > 0.90). This region contains more than 96% of all vertices.
- Region 4 (red): Vertices with high T_2* values (>40ms), notably in anterior cingulate cortex (BA24 & BA32). These vertices are possibly affected by surface misregistration.

The main purpose of this graph was to identify vertices where a linear relationship between MTR and T_2* can be tested without introducing too much bias. Based on these results, the

combination into a unique framework for estimating myelin content (MMEM, see below) will be performed on region #3.

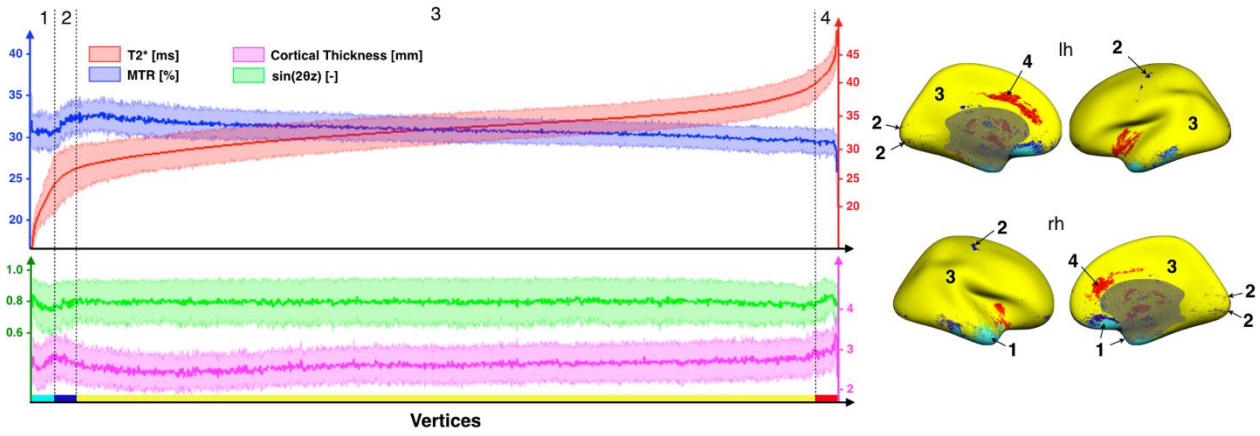

Figure 4-5**.** The graph on the left panel shows the distribution of the four signals used in the MMEM: MTR (blue), T_2* (red), CT (magenta) and B_0 orientation (green). The abscissa represents vertices defining the cortical surface (total number of vertices = 163,842). For clarity, the vertices order was chosen to make T_2* increasing and values were smoothed along the abscissa (100-point window). Error strips represent the inter-subjects SD. Similar trends are observed between the left and the right hemispheres, therefore only the signal of the right hemisphere was plotted. The distribution graph was divided into four ensembles of vertices (1, 2, 3 & 4) based on their signal's shapes. Vertices corresponding to these regions are plotted on the right panel with the respective colors: light blue, dark blue, yellow & red.

4.4.4 Multivariate myelin estimation model (MMEM)

4.4.4.1 Multilinear regression

Table 3 shows results of the linear models defined in Figure 2 and equations 2,3. These results show that myelin estimation is proportional to MTR and is inversely proportional to T_2*, as was expected (Cohen-Adad et al., 2011; Schmierer et al., 2004). Secondly, we notice that MTR accounts for about 54% of the ME_MTR metric and T_2* accounts for about 38% of the ME_T_2* metric, whereas cortical thickness and B_0 orientation have lesser influence (6% and <1%, respectively). Thirdly, we notice a fairly low inter-subject variability for the fittings coefficients of the constant part (*a*), the MTR or T_2* part (*b*) and the cortical thickness part (*c*), that suggest a

fairly good robustness of the model. However we notice a high variability of d and e parameters. We believe this is related to the fact that even though T_2* is modulated by B_0 orientation with respect to cortical surface (Cohen-Adad et al., 2012), this modulation is fairly low compared to that in the white matter. Evidences are found in gray/white matter comparative studies from (Sati et al., 2012). Moreover, it is possible that there is an inter-subject variability in the morphology of the cortex, e.g., orientation of coherently-aligned cortical fibers. Again, our model is performed in a subject by subject basis, and thus is not affected by the morphological inter-subject variability.

Table 4-3**.** Resulting coefficients of the linear models defined in equation 2,3 and their inter-subjects SD. Coefficients values are expressed in percentages in order to show their relatives contributions to the output maps (ME_MTR and ME_T_2*). *a* is the constant coefficient, *b* is the coefficient of the main metric (MTR in the ME_MTR regression and T_2* in the ME_T_2* regression), *c* is the CT coefficient, *d* and *e* are the coefficients of the B_0 orientation dependency (see equations (2) and (3)).

	a [%]	***b [%]***	***c [%]***	***d [%]***	***e [%]***
ME_MTR	-39.1 ± 1.9	54.2 ± 0.4	-6.2 ± 1.7	-0.14 ± 0.4	-0.05 ± 0.13
ME_T_2*	54.4 ± 2.0	-37.6 ± 2.9	-6.0 ± 2.5	0.33 ± 0.33	0.05 ± 0.12

4.4.4.2 Independent Component Analysis (ICA)

The second step was to perform an ICA for each subject, in order to find a transformation matrix that optimizes the extraction of the common information contained in ME_MTR and ME_T_2* (Hyvärinen and Oja, 2000; Xie and Wu, 2006). However, performing an ICA with large data vector (~164,000 vertices) is poorly robust. Therefore, a graphical validation of each ICA result (one per subject) was made. This graphical validation was useful to assess the result of each ICA's and the inter-subject consistency between results.

Figure 6A shows results of ICA for each subject. Pink arrows are the two vectors of the separating matrix *W* found by the ICA (Hyvärinen et al, 2000). Figure 6B represents the projection of the ME_MTR and ME_T_2* data into the space defined by the two vectors of the ICA's separating matrix. These graphs are useful to assess the non-correlation ($r<0.06$) of the resulting set of data.

The inter-subject variability of ICA results is fairly low (First vector direction = 58±4° and angle between both vectors = 112±5°), justifying the relevance of computing an average map of principal components across subjects.

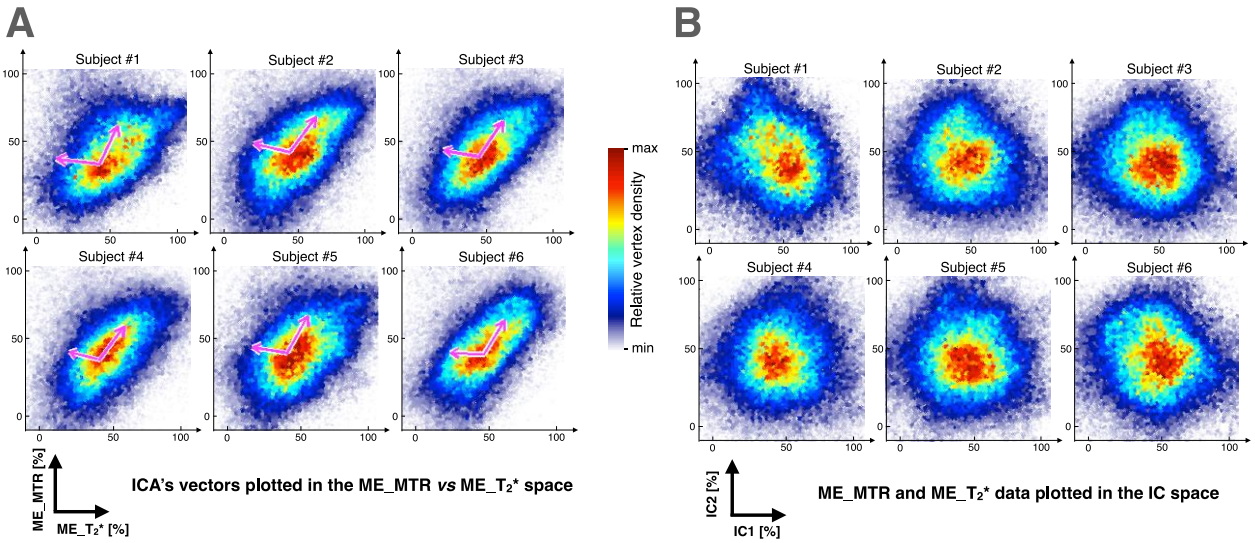

Figure 4-6**. (A)** Scatters of the individual data (ME_MTR vs ME_T_2*) and both ICA's resulting components (pink arrows). For each subjects, first ICA's component is the one sharing most variance between ME_MTR and ME_T_2* (pointing upper right). **(B)** Projection of the ME_MTR and ME_T_2* data into the space defined by the two ICA's components. These graphs are used to assess the non-correlation ($r<0.06$) of the resulting set of data. The colormap shows the data-point density in the scatters.

4.4.4.3 Combined Myelin Estimation (CME)

Figure 7 shows the average map of the Combined Myelin Estimation (CME). This map was computed from the first component of the ICA using equation (3) and averaged across subjects. The CME represents the common entity contained by ME_MTR and ME_T_2*, i.e., the source shared between ME_MTR and ME_T_2* that is mathematically independent from the rest of the acquired signal. Therefore, CME is thought to reflect the cortical myelin content with greater specificity than MTR or T_2* alone. The mean and SD of CME across the cortex was 50.3±0.7. Overall, we notice a high myelin estimation (yellow/red) in the primary motor cortex BA4=74±3% (here, % refers to the CME metric, and ±3% refers to the SD across subjects) and in the primary

somatosensory cortex (BA1=67±7%, BA2=59±4% and BA3=63±13%). Moreover, a high myelin estimation is also observed in the visual cortex (BA17=67±5% & BA18=68±6%) and the auditory cortex (BA42=57±10%). These results are consistent with previous study (Annese et al., 2004; Glasser and Van Essen, 2011; Glasser et al., 2014; Laule et al., 2008; Nieuwenhuys, 2013; Vogt, 1911).

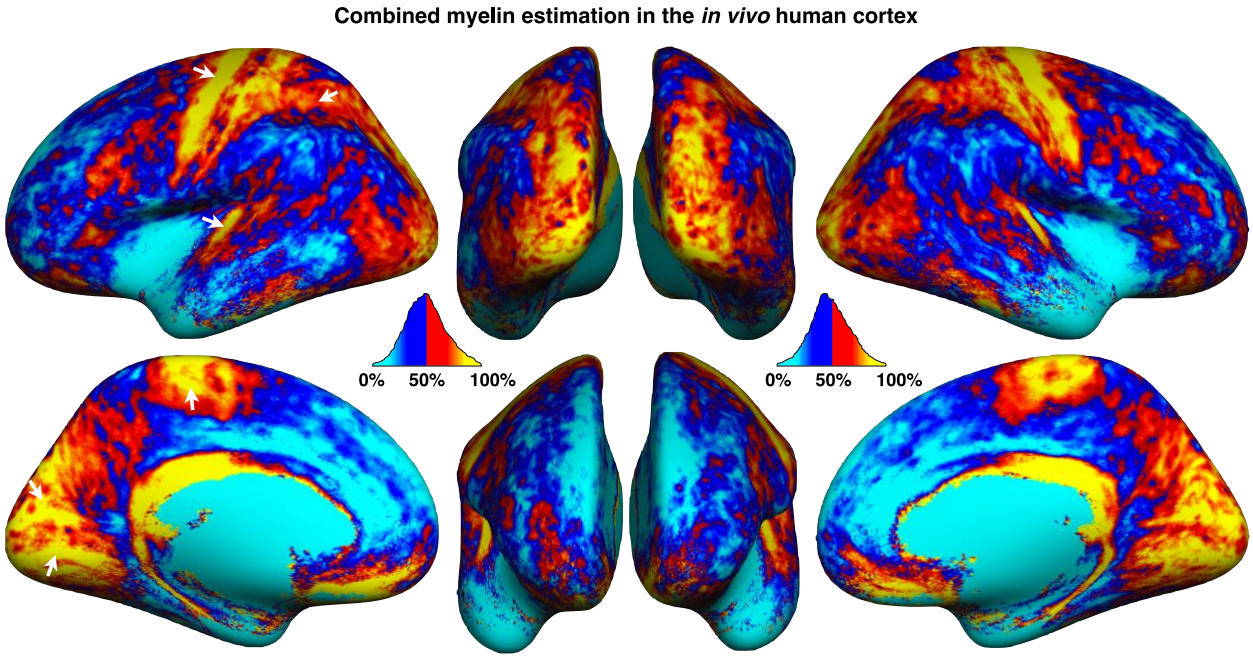

Figure 4-7**.** Average map of the Combined Myelin Estimation (CME). The mean and SD of CME across the cortex was 50.3±0.7. Overall, we notice a high myelin estimation (yellow/red) in the primary motor cortex BA4=74±3% (here, % refers to the CME metric, and ±3% refers to the SD across subjects) and in the primary somatosensory cortex (BA1=67±7%, BA2=59±4% and BA3=63±13%). Moreover, a high myelin estimation is also observed in the visual cortex (BA17=67±5% & BA18=68±6%) and the auditory cortex (BA42=57±10%).

4.4.4.4 CME maps comparisons

Figure 8A shows a side-by-side comparison of CME, ME_MTR and ME_T_2* on the inflated cortical surface. Major differences between ME_MTR and ME_T_2* are indicated with white circles (plain and dashed). In the medial view of ME_T_2*, one can observe a higher signal in the visual cortex than that in the ME_MTR (plain-circle). Inversely, the ME_T_2* map shows a

lower signal in the precuneus areas (small-dashed-circle) and superior frontal cortex (middle-dashed-circle) compared to that in the ME_MTR map. In the lateral view of the ME_MTR map, one can observe a higher signal in the somatosensory association cortex (small-dashed-circle) and in the angular gyrus (plain-circle), compared to that in the ME_T_2* map. Figure 8B,C show correlations between the myelin estimations metrics and histology values from (Braitenberg 1962), which are based on optical attenuation measures in an ex vivo human cortex stained for myelin. The Pearson's correlation coefficients of: ME_MTR vs. Histology, ME_T_2* vs. Histology and CME vs. Histology, were respectively 0.71 (p-value < 0.05), 0.69 (p-value < 0.05) and 0.77 (p-value < 0.01). These correlations suggest that CME is a more specific marker for cortical myelin content than ME_MTR or ME_T_2* taken separately.

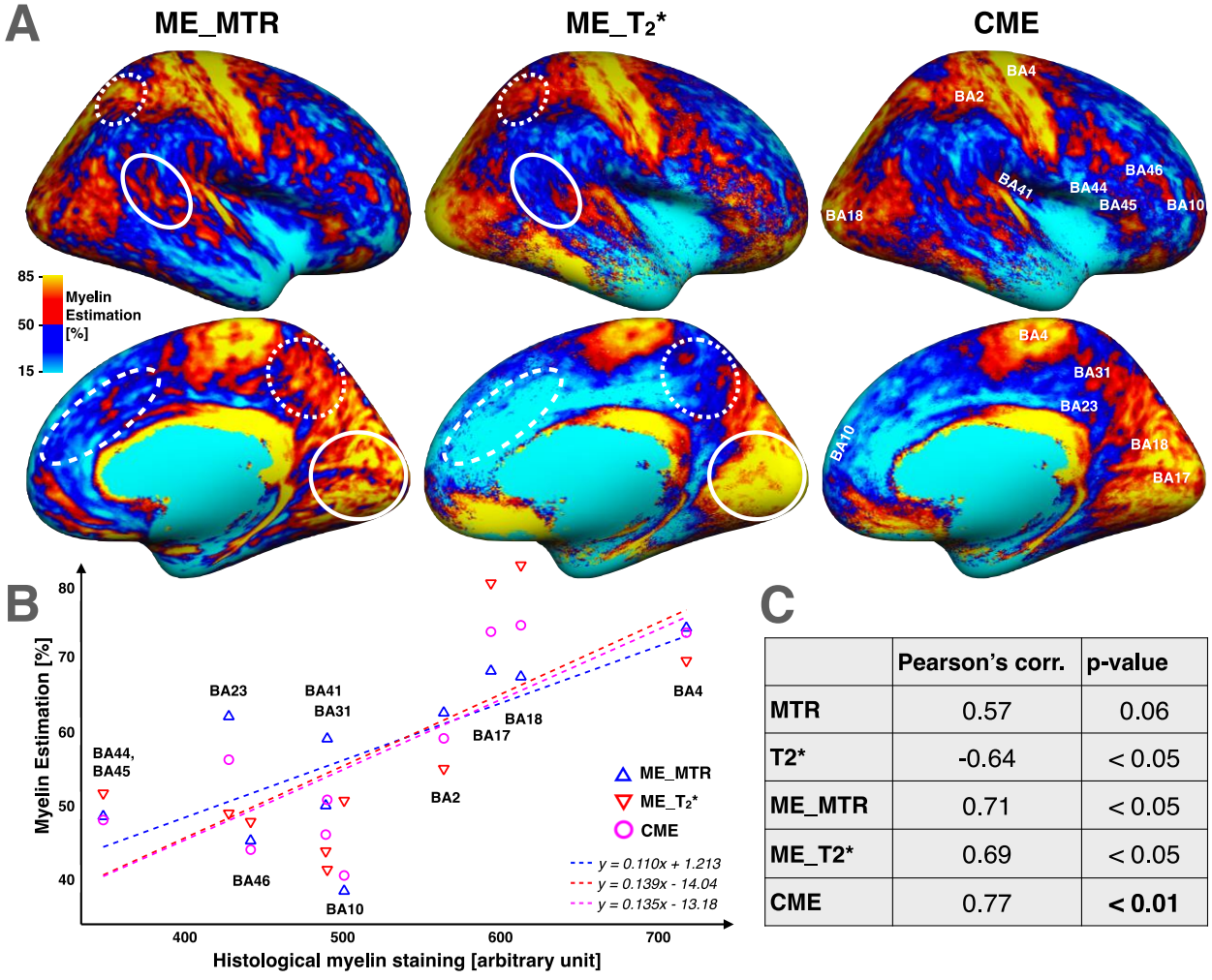

C

	Pearson's corr.	p-value
MTR	0.57	0.06
T2*	-0.64	< 0.05
ME_MTR	0.71	< 0.05
ME_T2*	0.69	< 0.05
CME	0.77	**< 0.01**

Figure 4-8**. (A)** Side-by-side comparison between CME maps and its both parents contrasts: ME_MTR and ME_T_2*. Major differences between ME_MTR and ME_T_2* are circled by white

circles. The CME map is labelled with the Brodmann areas used in the histological comparison. **(B)** Comparison between our myelin-related maps (CME, ME_MTR and ME_T_2*) and previous cortical myelin content histology data performed by Braitenberg (Braitenberg, 1962) in different Brodmann areas. The equations of the linear regressions are displayed at the bottom-right of the graph. The linear regression between T_2* and histological myelin staining (HMS) is: T_2*=-15.2*10^{-3}[ms/a.u.]*HMS+39.4[ms]; and the linear regression between MTR and HMS is: MTR=4.2*10^{-3}[%/a.u.]*HMS+29.0[%]. **(C)** Pearson's correlations coefficients between MTR vs Histology, T_2* vs Histology, ME_MTR vs Histology, ME_T_2* vs Histology and CME vs Histology and their respective P_values. Results suggests first that ME_MTR and ME_T_2* contrasts are relevant marker of the cortical myelin content and second that CME is a more specific marker for cortical myelin content than ME_MTR or ME_T_2* taken separately.

4.4.4.5 Analyses within Brodmann Areas

Figure 9A shows the CME map with an overlay of the PALS-B12 Brodmann Areas (BA). This figure shows a fair adequation between variations of CME and BA borders, for instance in BA1, BA2, BA3 and BA4 (primary motor and primary somatosensory cortex, green arrows), in BA17, BA18, BA19 (visual cortex, blue arrows) and in BA42 (auditory cortex, yellow arrow). However, in several areas (for instance BA22 or BA39) CME is quite heterogeneous, suggesting to divide these regions in smaller areas if we aimed to build a more accurate myelo-architectural atlas.

Figure 9B shows the CME map averaged within each BA and Figure 9C shows the mean BA values, as well as the inter-subject SD and the intra-area SD. In comparison with the SD across the entire cortex (26.5%), the intra-area SD is fairly low (in average 11.9%). We also note that the inter-subject SD is low, with an average coefficient of variation of 25% (here the average COV was calculated by computing the COV for each area, and then averaging all COVs across areas).

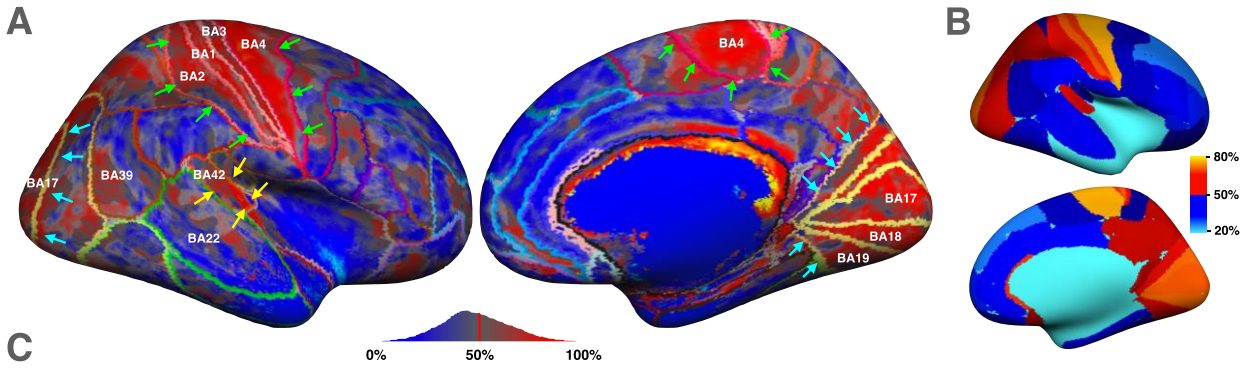

BA	1	2	3	4	5	6	7	8	9	10	17	18	19	22	23	24	29	30	31	32	39	40	41	42	43	44	45	46	47
mean [%]	67	59	63	74	50	46	53	30	30	37	67	68	58	42	54	38	55	52	55	40	46	38	47	57	41	46	43	42	37
SD_Subject [%]	7	4	13	3	9	3	5	6	8	6	5	6	3	5	8	8	16	6	5	6	4	4	8	10	7	5	11	7	6
SD_Area [%]	11	12	15	15	9	11	11	10	12	13	13	11	12	13	19	17	11	13	11	15	11	8	7	17	8	11	7	10	13
COV_Subject	0.1	0.06	0.2	0.04	0.18	0.06	0.09	0.2	0.26	0.16	0.07	0.08	0.05	0.11	0.14	0.21	0.29	0.11	0.09	0.15	0.08	0.1	0.17	0.17	0.17	0.1	0.25	0.16	0.16
COV_Area	0.36	0.2	0.23	0.2	0.18	0.23	0.2	0.33	0.4	0.35	0.19	0.16	0.2	0.3	0.35	0.44	0.2	0.25	0.2	0.37	0.23	0.21	0.14	0.29	0.19	0.23	0.16	0.23	0.35

Figure 4-9**. (A)** CME map with an overlay of the PALS-B12 Brodmann Areas (BA). This figure shows a fair adequation between variations of CME and BA borders, for instance in BA1, BA2, BA3 and BA4 (primary motor and primary somatosensory cortex, green arrows), in BA17, BA18, BA19 (visual cortex, blue arrows) and in BA42 (auditory cortex, yellow arrow). **(B)** CME map averaged within each BA. **(C)** Mean BA values, as well as the inter-subject SD and the intra-area SD. In comparison with the SD across the entire cortex (26.5%), the intra-area SD is fairly low (in average 11.9%).

Figure 10 shows bar graphs representing mean and intersubject SD values of the different metrics used in the model (CME, MTR, ME_MTR, T_2*, ME_T_2*) within Brodmann regions. This graph shows the inter-hemispheric differences across (CME, MTR, ME_MTR, T_2* and ME_T_2*). Overall, we observe a fairly good right-left reproducibility, except in some regions as described hereafter. The CME map shows significant hemispheric differences in BA4 and BA31 (more myelin estimated in RH, $p<0.05$) and in BA17 and BA23 (more myelin estimated in LH, respectively $p<0.05$ and $p<0.01$).

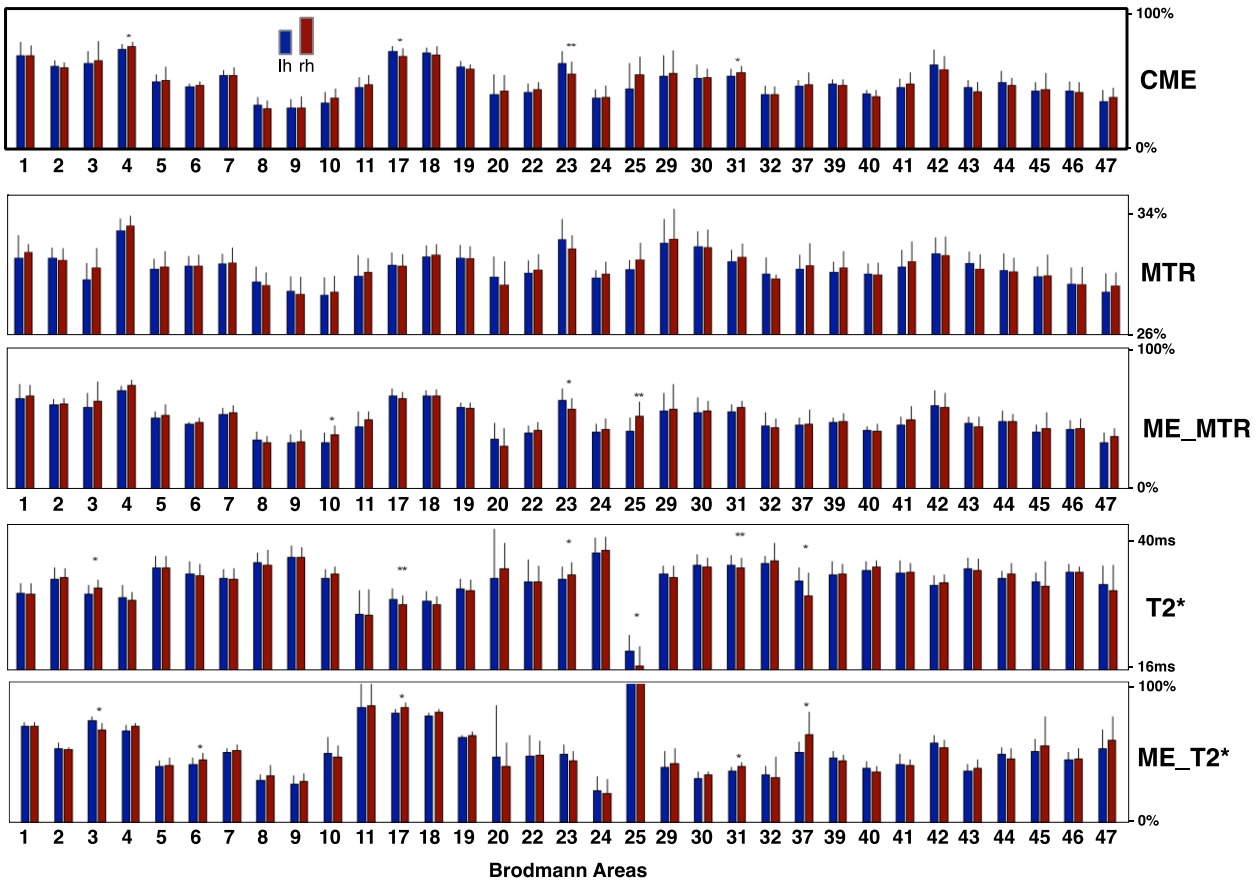

Figure 4-10**.** Bar graphs representing mean and inter-subject SD values of the different metrics used in the MMEM (CME, MTR, ME_MTR, T_2*, ME_T_2*) within Brodmann regions. Overall, we observe a fairly good right-left reproducibility. The CME map shows significant hemispheric differences in BA4 and BA31 (more myelin estimated in rh, $p<0.05$) and in BA17 and BA23 (more myelin estimated in lh, respectively $p<0.05$ and $p<0.01$).

4.5 Discussion

This study presented a novel approach to combine MTR and T_2* in the *in vivo* human cortex, with the goal of studying cortical myeloarchitecture. We proposed to use a multivariate model to extract myelin-related information shared by both metrics. The model takes into account cortical thickness and B_0 orientation and is flexible, i.e., other metrics such as T_1 and diffusion data can be added. In the following, we discuss the sensitivity and specificity of MTR and T_2* to detect myelin content, the multivariate model and ICA decomposition for combining MTR and T_2* and the resulting maps, limitations and perspectives.

4.5.1 Sensitivity and specificity of MTR and T_2* for quantifying myelin content

MT reflects the relative density of macromolecules, such as lipids or proteins. Since myelin has a lipid-protein structure (~80% lipids and ~20% protein), MT is able to provide indirect measure of myelin content. The MT phenomenon is complex and some of its underlying physical mechanisms are still unknown (Kim and Cercignani, 2014). Overall, the MT effect induces reduction of signal in tissues with large amount of MT, such as those with high concentration in macromolecules (e.g., lipids). For example, MT ratio (MTR) was shown to correlate well with myelin content in the white matter (Schmierer et al., 2004). Recently, MTR was shown to be sensitive to cortical demyelination in multiple sclerosis patients (Chen et al., 2013; Derakhshan et al., 2014). However, MTR is only a semi-quantitative metric and has several confounds. Firstly, B1 inhomogeneities related to RF transmission induce variabilities on the MT pulse power, which affect MTR measures. Secondly, MTR values depend on the sequence parameters (Berry et al., 1999). Thirdly, MTR values are affected by T_1 relaxation (Pike Bruce, 1996). Despite the longer acquisition time, quantitative MT (Levesque and Pike, 2009) provides more accurate estimation of myelin content.

T_2* is the effective transverse relaxation time and is therefore affected by (i) mesoscopic field inhomogeneities, which result from susceptibility differences between tissues (parenchyma, deoxygenated blood, bone, cartilage, etc.) and (ii) macroscopic field inhomogeneities, which arise from magnetic field imperfections, air–tissue boundaries, or ferromagnetic objects (e.g., metal clips, implants, dental prosthesis). The latter are characterized by large-scale gradients that cause enhanced signal decay in gradient echo images and thus apparent decrease in T_2* that can confound the underlying biology. Furthermore, the specificity of T_2* contrast to myelin content is hampered by fiber orientation in the white matter (Lee et al., 2011) and in the cortex (Cohen-Adad et al., 2012), tissue iron level (Lee et al., 2012; Stüber et al., 2014), blood vessels (Spees et al., 2001), blood oxygen level (Li et al., 1998). Note that in this study, the effect of blood vessel was minimized by excluding large blood vessels using manual masks. Also, capillary blood should only contribute minimally to the T_2* contrast, as reported by Lee et al. (Lee et al., 2012).

4.5.2 Combining MTR and T_2* using ICA

The main goal of this study was to gain specificity in myelin mapping by combining T_2* and MTR. Here, ICA decomposition was chosen to extract shared information between MTR and T_2* that represents myelin content. The ICA offers the advantage of recovering sources of interest (here: myelin content) from observed mixtures, making it well suited for the brain data analysis because of the multifaceted origin of MTR and T_2* contrasts. Here we used the fast-fixed point algorithm presented by Hyvärinen et al (Bingham and Hyvärinen, 2000). This algorithm transforms the observed data to the linear combination of source signals (or independent components) which are non-gaussian and mutually independent. The output of the ICA is a separating matrix, which is represented by two vectors defining a new basis of independent components. Results of the ICA on our MTR and T_2* data showed a fairly low inter-subject variability of the directions of the first vector (58±4°), which is assumed to represent myelin content. This low variability suggests stability of the decomposition process with respect to the spatial distribution of myelin-related source. Note that the current ICA framework is modular and the model would benefit from complementary sources of contrast sensitive to myelin content, such as T_1 (Bock et al., 2009; Dinse et al., 2013; Sereno, 1991), T_1w/T2w (Glasser and Van Essen, 2011), phase images (He and Yablonskiy, 2009) and diffusion data. While adding more metrics will likely increase the sensitivity and specificity to myelin, it is important to keep in mind that some metrics can share variance due to a shared MR contrast mechanism and/or artifactual contribution. For example, MTR contrast is partly driven by T_1. In this study we chose to acquire T_2* and MTR. The rationale behind acquiring these two contrasts was to show a proof-of-concept for combining two myelin mapping techniques with very different biophysical properties: susceptibility-related effect for T_2* and macromolecular-related magnetization transfer effect for MTR.

4.5.3 Interpretations of the combined myelin estimation (CME) maps

The CME exhibited high values (>70%) in the primary motor cortex (BA4), in the primary somatosensory cortex (BA1, BA2 and BA3), in the visual cortex (BA17 & BA18) and in the auditory cortex (BA42). Contrariwise, the insula, the frontal and prefrontal cortex (BA8, BA9 & BA10) and the anterior cingulate cortex (BA24 & BA32) have low CME values (<30%). Seen as an indicator of myelin content, this pattern of CME across the cortex is in concordance with previous cortical myelin-oriented studies (Annese et al., 2004; Glasser and Van Essen, 2011;

Glasser et al., 2014; Laule et al., 2008; Nieuwenhuys, 2013; Vogt, 1911). Moreover, the intra-regional standard deviation of the CME is low in comparison to that across the whole cortex. This suggests a fairly homogenous myelin estimate inside the putative cortical areas. This observation is consistent with previous studies showing homogeneous myeloarchitecture within functionally-defined areas. (Abdollahi et al., 2014; Bock et al., 2009; Geyer and Turner, 2013; Glasser and Van Essen, 2011; Glasser et al., 2014; Nieuwenhuys, 2013; Sereno, 1991).

The CME map was compared with existing myelin-related maps from the literature. The MR longitudinal relaxation time T_1 has been shown to be closely related to myelin content in vivo (Dick et al., 2012; Koenig et al., 1990; Sigalovsky et al., 2006) and ex vivo (Mottershead et al., 2003; Schmierer et al., 2008, 2004) showing for example high correlation ($r = 0.89$) between T_1 relaxation time and myelin content in fixed brain (Schmierer et al., 2008). Recently, (Sereno et al., 2013) have computed high resolution quantitative R1 (inverse of T_1) maps from PDw and T_1w images according to the formalism developed by Helms et al. (2008) and including a correction for imperfect RF spoiling (Preibisch and Deichmann, 2009) in order to obtain an accurate estimation of the cortical myelin content. Moreover, the ratio between T_1w and T2w images has been shown to be an accurate estimate of the relative myelin content across cortex (Glasser and Van Essen, 2011; Glasser et al., 2014). Glasser et al. (2014) have demonstrated that T_1w/T2w maps reveals an observer-independent map of the area boundaries for dozens of cortical areas in a population-average analysis. Figure 11 shows a side-by-side comparison between our CME maps and the cortical myelin estimations based on T_1w/T2w from Glasser et al. (Glasser and Van Essen, 2011; Glasser et al., 2014) and R1 (inverse of T_1) contrast from Sereno et al. (Sereno et al., 2013). Strong similarities are observed across maps, notably high myelin indices in the motor, visual and auditory cortices and low myelin indices in the anterior frontal cortex and in the temporal cortex. Small details are also shared by all contrasts, for example the middle-high spot located in the frontal lobe of the left hemisphere (green circle), the middle-high spot in the superior temporal cortex of the right hemisphere (green circle) and the bright spot in the lateral occipital cortex (near BA19). More interestingly, some discrepancies are observed for the CME map (red circles), i.e. regions of strong contrast previously not seen in other metrics. For example, we can observe a stronger signal in CME maps than in R1 or T_1w/T2w maps in the pars triangularis area (dashed-red circle, near BA47) and in the superior parietal area (red circle, near BA7). Further work is needed to validate these findings with histology.

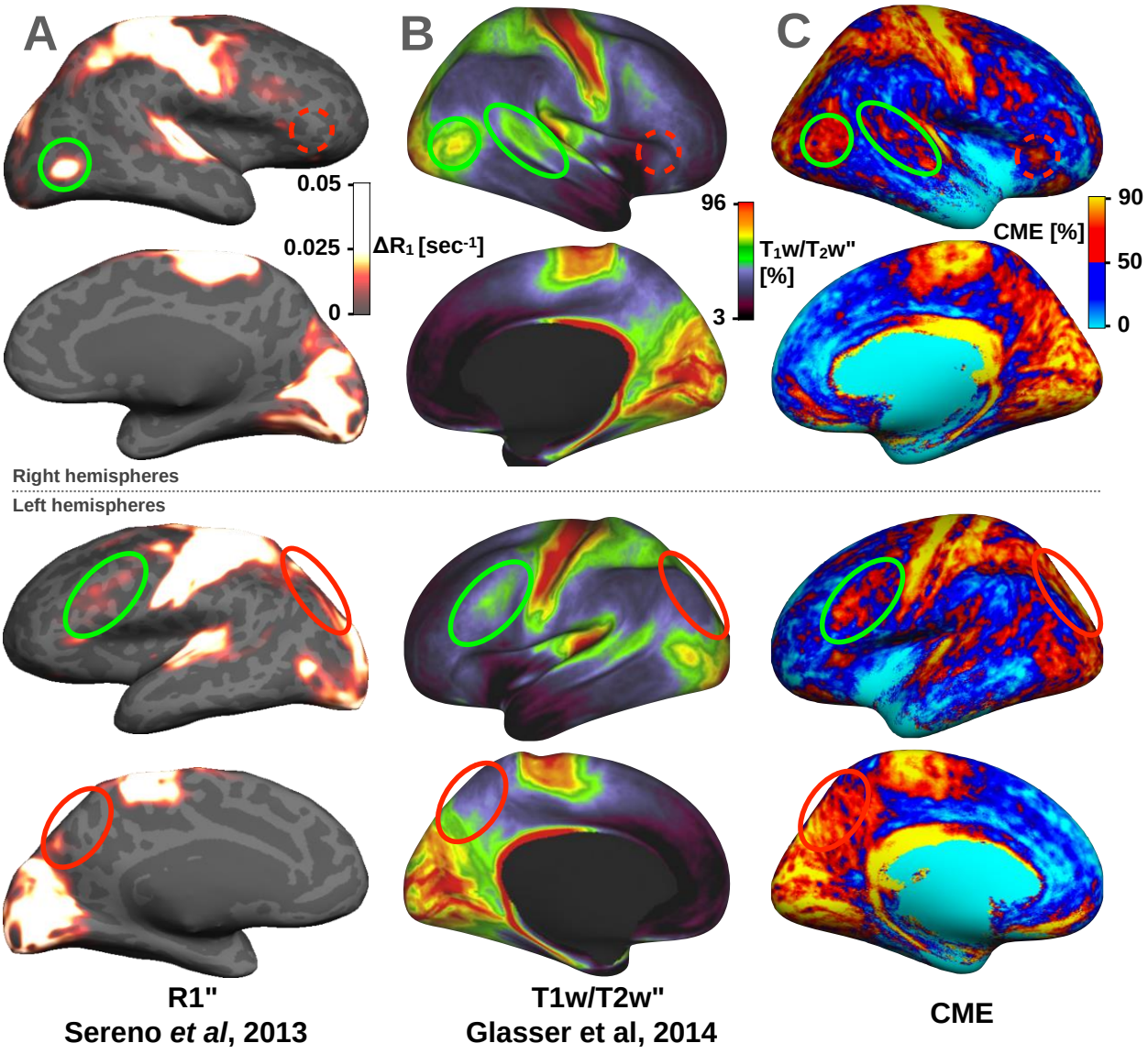

Figure 4-11**.** Comparison with recent in vivo studies showing different contrasts sensitive to cortical myelin content in healthy adults. (A) quantitative R_1 maps averaged across 6 control subjects (Sereno et al., 2013). ΔR_1 is the difference between the mean R_1 (across the cortex) and the R_1 in a specific vertex. **(B)** T_1w/T_2w maps averaged across 69 subjects (Glasser and Van Essen, 2011). **(C)** CME maps averaged across 6 subjects, unsmoothed. Green circles show similarities between CME maps and R_1 or T_1w/T_2w. Red circles show differences.

We chose to analyse our data with respect to cortical parcellation offered by the PALS-B12 atlas, which aims at representing homogeneous cytoarchitecture within the human cortex as proposed by Brodmann (Brodmann, 1909). Borders of these regions are defined by the variation

of the cells organization and structure of the cortex and are thought to represent functional units (Barbier et al., 2002; Jacot-Descombes et al., 2012; Lanzilotto et al., 2013). In analogy to the present study, we observe that regions representing specific functions of the human body (primary motor, auditory, visual) overlap with regions where CME was high. However, there is not necessarily a direct correspondence between myelo- and cyto-architecture (Geyer et al., 2011). Other atlases are available in the literature, notably the myeloarchitectonic atlas of Nieuwenhuys et al. (Nieuwenhuys et al. 2014), which divides the cortex into 180 myeloarchitectonic areas. A qualitative side-by-side comparison revealed some similarities between this atlas and the CME map. For example, in the pars triangularis region the bright spot visible in CME map only (dashed-red circle in Figure 11C) seems to overlap with area 57-58 in the Nieuwenhuys atlas (red circle in Supplementary material S3). We notice that this bright spot is in accordance with a previous ex vivo monkey histology (Cruz-Rizzolo et al., 2011). Moreover, the motor cortex in the CME map exhibits a multiple-line pattern along the central sulcus, which is also visible in the Nieuwenhuys atlas. Moreover, the motor cortex in the CME map exhibits a multiple-line pattern along the central sulcus, which is also visible in the Nieuwenhuys atlas.

It should be noted that CME is currently not calibrated on true myelin values. CME's limits (0% to 100%) were defined based on regions with qualitatively low and high myelin content (Annese et al., 2004; Glasser and Van Essen, 2011; Glasser et al., 2014; Laule et al., 2008; Nieuwenhuys, 2013; Vogt, 1911). Such a calibration procedure is challenging because ex vivo measures of myelin content may not be accurate for in vivo assessment. Histology and immunohistochemistry techniques may suffer from non-uniformity (Cruz-Rizzolo et al., 2011; Culling, 2013). Moreover, optical density measurements of the stain do not provide an accurate measure of myelin density because it does not probe the quantity of myelin in a slice (Culling, 2013). (Stüber et al., 2014) introduced the PIXE technique recently using complex experimental setup. Furthermore, MR parameters change post mortem due to fixation. For instance, the correlation of MTR with myelin content is much stronger before fixation (Schmierer et al., 2008). Moreover, image registration is not easy in such studies, and spatial sampling is limited. Finally, more knowledge is required about the relationship between CME and true myelin content. For example, here we assumed linearity, but this has to be verified before calibration procedure.

Concerning the fiber orientation dependency, we are aware that various models have been proposed in the literature. For example, (Bender and Klose, 2010; Denk et al., 2011) have shown

that the fiber orientation dependence can be well described using the term sin(theta)^2. We have therefore compared our model with the sin(theta)^2 model. Results were similar, with a square difference (averaged across all vertices) of 0.32 %2 for ME_MTR and 0.11 %2 for ME_T_2*.

The correlations with histological work of Braitenberg (Braitenberg, 1962) suggest that CME is a more specific marker for cortical myelin content compared to ME_MTR or ME_T_2* taken separately. We have also shown that ME_MTR and ME_T_2* are more specific markers of myelin than MTR and T_2* (see Figure 8). This type of comparison is however limited by several factors. Firstly, the Braitenberg dataset was only limited to a few regions. Secondly, the study of Braitenberg was hampered by imperfect tissue fixation and staining, which added potential biases in the measures.

4.5.4 Limitations and futures studies

T_2* volumes were acquired with anisotropic voxels in order to maintain a high in-plane resolution (0.3x0.3 mm). Anisotropic voxels are subject to more inhomogeneous partial volume effect during the cortical sampling. In the future, EPI-Based multi-echo measurements (Zwanenburg et al., 2011) may sufficiently accelerate acquisition to allow use of isotropic voxels. MTR volumes were acquired with isotropic voxels, despite a somewhat low resolution (1.2mm) in comparison with the thickness of the cortex. Future studies could benefit from MT-prepared multi-echo EPI (Helms and Hagberg, 2005) in order to acquire faster MT-weighted images and potentially increase the spatial resolution thanks to the higher SNR efficiency of EPI sequences. However it is important to keep in mind that EPI measurement suffers from geometric distortions, which are difficult to perfectly correct using standard approaches (fieldmap-based or non-rigid alignment). Residual distortions would lead to imperfect registration to the cortical surface and hence lead to potentially wrong values when sampling along the cortical ribbon.

The MMEM used a normalization procedure based on regions that are known to be highly and poorly myelinated. Thus, the output of the MMEM does not give an absolute measure of myelin content, but rather an indicator of relative level of myelin compared to other brain areas. Furthermore, it could be argued the choice of regions for normalization purpose was not adequate, however the robustness of the resulting MMEM coefficients was fairly high. For example, when using only BA4 (high myelin) and BA9 (low myelin), the resulting coefficients were less than 1% different compared to the results presented in this study.

Validation is essential to these types of MRI studies. Although CME maps showed remarkably high spatial correspondence with previous *in vivo* and postmortem studies (Annese et al., 2004; Glasser and Van Essen, 2011; Glasser et al., 2014; Laule et al., 2008; Nieuwenhuys, 2013; Vogt, 1911) it remains essential to further compare MRI maps with full cortex histology samples stained for myelin. However, limitations exist with histological staining, as it does not necessarily represent quantitative measure of myelin content and is hampered by the attachment properties of the tissue (depends on preparation, fixation, etc.) (Jain et al., 1998; Pistorio et al., 2006).

The multivariate myelin estimation model has the potential to be useful in assessing early cortical changes in myelin in patients with neurodegenerative diseases such as multiple sclerosis.

4.6 Acknowledgements

We thank Benjamin De Leener, Tanguy Duval, Simon Lévy, Blanche Perraud, Nikola Stikov and Yves Goussard (Polytechnique Montreal), Pierre Bellec (Université de Montréal), Céline Louapre and Costanza Giannì (A. A. Martinos Center, Boston), Gaëlle Seret (Polytechnique Paris) and Jérémie Pilon (Danone Research) for helpful discussions. This work was supported by the National Multiple Sclerosis Society [FG 1892A1/1, 4281-RG-A-1], by the National Center for Research Resources [P41-RR14075], the Fonds de Recherche du Québec - Santé (FRQS), the Fonds de Recherche du Québec - Nature et Technologies (2015-PR-182754), the Quebec BioImaging Network (QBIN), the Natural Sciences and Engineering Research Council of Canada (NSERC) and the Polytechnique MEDITIS program.

4.7 References

Abdollahi, R.O., Kolster, H., Glasser, M.F., Robinson, E.C., Coalson, T.S., Dierker, D., Jenkinson, M., Van Essen, D.C., Orban, G.A., 2014. Correspondences between retinotopic areas and myelin maps in human visual cortex. Neuroimage 99, 509–524.

Annese, J., Pitiot, A., Dinov, I.D., Toga, A.W., 2004. A myelo-architectonic method for the structural classification of cortical areas. Neuroimage 21, 15–26.

Barbier, E.L., Marrett, S., Danek, A., Vortmeyer, A., van Gelderen, P., Duyn, J., Bandettini, P., Grafman,

J., Koretsky, A.P., 2002. Imaging cortical anatomy by high-resolution MR at 3.0T: detection of the stripe of Gennari in visual area 17. Magn. Reson. Med. 48, 735–738.

Bender, B., Klose, U., 2010. The in vivo influence of white matter fiber orientation towards B_0 on T_2* in the human brain. NMR Biomed. 23, 1071–1076.

Berry, I., Barker, G.J., Barkhof, F., Campi, A., Dousset, V., Franconi, J.M., Gass, A., Schreiber, W., Miller, D.H., Tofts, P.S., 1999. A multicenter measurement of magnetization transfer ratio in normal white matter. J. Magn. Reson. Imaging 9, 441–446.

Bingham, E., Hyvärinen, A., 2000. A fast fixed-point algorithm for independent component analysis of complex valued signals. Int. J. Neural Syst. 10, 1–8.

Bock, N.A., Kocharyan, A., Liu, J.V., Silva, A.C., 2009. Visualizing the entire cortical myelination pattern in marmosets with magnetic resonance imaging. J. Neurosci. Methods 185, 15–22.

Braitenberg, V., 1962. A note on myeloarchitectonics. J. Comp. Neurol. 118:141–156.

Brodmann, K., 1909. BRODMANN'S Localisation in the Cerebral Cortex. Springer.

Chen, J.T.-H., Easley, K., Schneider, C., Nakamura, K., Kidd, G.J., Chang, A., Staugaitis, S.M., Fox, R.J., Fisher, E., Arnold, D.L., Trapp, B.D., 2013. Clinically feasible MTR is sensitive to cortical demyelination in MS. Neurology 80, 246–252.

Clarkson, M.J., Cardoso, M.J., Ridgway, G.R., Modat, M., Leung, K.K., Rohrer, J.D., Fox, N.C., Ourselin, S., 2011. A comparison of voxel and surface based cortical thickness estimation methods. Neuroimage 57, 856–865.

Cohen-Adad, J., 2014. What can we learn from T_2* maps of the cortex? Neuroimage 93 Pt 2, 189–200.

Cohen-Adad, J., Benner, T., Greve, D., Kinkel, R.P., Radding, A., Fischl, B., Rosen, B.R., Mainero, C., 2011. In vivo evidence of disseminated subpial T_2* signal changes in multiple sclerosis at 7 T: a surface-based analysis. Neuroimage 57, 55–62.

Cohen-Adad, J., Polimeni, J.R., Helmer, K.G., Benner, T., McNab, J.A., Wald, L.L., Rosen, B.R., Mainero, C., 2012. T_2* mapping and B_0 orientation-dependence at 7 T reveal cyto- and myeloarchitecture organization of the human cortex. Neuroimage 60, 1006–1014.

Cruz-Rizzolo, R.J., De Lima, M.A.X., Ervolino, E., de Oliveira, J.A., Casatti, C.A., 2011. Cyto-, myelo- and chemoarchitecture of the prefrontal cortex of the Cebus monkey. BMC Neurosci. 12, 6.

Culling, C.F.A., 2013. Handbook of Histopathological and Histochemical Techniques Including Museum Techniques, 3rd ed. ed. Burlington Elsevier.

Dale, A.M., Fischl, B., Sereno, M.I., 1999. I. Segmentation and Surface Reconstruction. Neuroimage 9, 179–194.

Deistung, A., Schäfer, A., Schweser, F., Biedermann, U., Turner, R., Reichenbach, J.R., 2013. Toward in vivo histology: a comparison of quantitative susceptibility mapping (QSM) with magnitude-, phase-, and R2*-imaging at ultra-high magnetic field strength. Neuroimage 65, 299–314.

Denk, C., Hernandez Torres, E., MacKay, A., Rauscher, A., 2011. The influence of white matter fibre orientation on MR signal phase and decay. NMR Biomed. 24, 246–252.

Derakhshan, M., Caramanos, Z., Narayanan, S., Arnold, D.L., Louis Collins, D., 2014. Surface-based analysis reveals regions of reduced cortical magnetization transfer ratio in patients with multiple sclerosis: a proposed method for imaging subpial demyelination. Hum. Brain Mapp. 35, 3402–3413.

Dick, F., Tierney, A.T., Lutti, A., Josephs, O., Sereno, M.I., Weiskopf, N., 2012. In vivo functional and myeloarchitectonic mapping of human primary auditory areas. J. Neurosci. 32, 16095–16105.

Dinse, J., Waehnert, M., Tardif, C.L., Schäfer, A., Geyer, S., Turner, R., Bazin, P.L., 2013. A Histology-Based Model of Quantitative T_1 Contrast for In-vivo Cortical Parcellation of High-Resolution 7 Tesla Brain MR Images, in: Springer (Ed.), Medical Image Computing and Computer-Assisted Intervention - 2013. pp. 51–58.

Duyn, J.H., van Gelderen, P., Li, T.-Q., de Zwart, J.A., Koretsky, A.P., Fukunaga, M., 2007. High-field MRI of brain cortical substructure based on signal phase. Proc. Natl. Acad. Sci. U. S. A. 104, 11796–11801.

Fischl, B., 2012. FreeSurfer. Neuroimage 62, 774–781.

Fischl, B., Sereno, M.I., Dale, A.M., 1999. II: Inflation, Flattening, and a Surface-Based Coordinate System. Neuroimage 9, 195–207.

Flechsig, P.E., 1920. Anatomie des menschlichen Gehirns und Rückenmarks auf myelogenetischer Grundlage. Thieme.

Fukunaga, M., Li, T.-Q., van Gelderen, P., de Zwart, J.A., Shmueli, K., Yao, B., Lee, J., Maric, D., Aronova, M.A., Zhang, G., Leapman, R.D., Schenck, J.F., Merkle, H., Duyn, J.H., 2010. Layer-specific variation of iron content in cerebral cortex as a source of MRI contrast. Proc. Natl. Acad. Sci. U. S. A. 107, 3834–3839.

Geyer, S., Turner, R., 2013. Microstructural parcellation of the human cerebral cortex from Brodmann's post-mortem map to in vivo mapping with high-field magnetic resonance imaging. Berlin ; New York : Springer, c2013.

Geyer, S., Weiss, M., Reimann, K., Lohmann, G., Turner, R., 2011. Microstructural Parcellation of the Human Cerebral Cortex - From Brodmann's Post-Mortem Map to in vivo Mapping with High-Field Magnetic Resonance Imaging. Front. Hum. Neurosci. 5, 19.

Glasser, M.F., Goyal, M.S., Preuss, T.M., Raichle, M.E., Van Essen, D.C., 2014. Trends and properties of human cerebral cortex: correlations with cortical myelin content. Neuroimage 93 Pt 2, 165–175.

Glasser, M.F., Van Essen, D.C., 2011. Mapping human cortical areas in vivo based on myelin content as revealed by T_1- and T2-weighted MRI. J. Neurosci. 31, 11597–11616.

Govindarajan, S.T., Cohen-Adad, J., Sormani, M.P., Fan, A.P., Louapre, C., Mainero, C., 2014. Reproducibility of T_2* mapping in the human cerebral cortex in vivo at 7 Tesla MRI. J. Magn. Reson. Imaging.

Greve, D.N., Fischl, B., 2009. Accurate and robust brain image alignment using boundary-based registration. Neuroimage 48, 63–72.

Helms, G., Hagberg, G.E., 2005. Quantification of magnetization transfer and relaxation rates by MT-prepared multi-echo EPI. P r o c . I nt l . S o c . M a g . R e s o n . M e d. 13, 2221.

Henkelman, R.M., Stanisz, G.J., Graham, S.J., 2001. Magnetization transfer in MRI: a review. NMR Biomed. 14, 57–64.

Hernando, D., Vigen, K.K., Shimakawa, A., Reeder, S.B., 2012. R 2* mapping in the presence of macroscopic B_0 field variations. Magn. Reson. Med. 68, 830–840.

Hwang, D., Kim, D.-H., Du, Y.P., 2010. In vivo multi-slice mapping of myelin water content using T_2* decay. Neuroimage 52, 198–204.

Hyvärinen, A., Oja, E., 2000. Independent component analysis: algorithms and applications. Neural Netw. 13, 411–430.

Jacot-Descombes, S., Uppal, N., Wicinski, B., Santos, M., Schmeidler, J., Giannakopoulos, P., Heinsen, H., Heinsein, H., Schmitz, C., Hof, P.R., 2012. Decreased pyramidal neuron size in Brodmann areas 44 and 45 in patients with autism. Acta Neuropathol. 124, 67–79.

Jain, N., Catania, K., Kaas, J., 1998. A histologically visible representation of the fingers and palm in primate area 3b and its immutability following long- term deafferentations. Cereb Cortex 8(3):227–36.

Kim, M., Cercignani, M., 2014. Chapter 3.4 - Magnetization Transfer, in: Wheeler-Kingshott, J.C.-A.A.M. (Ed.), Quantitative MRI of the Spinal Cord. Academic Press, San Diego, pp. 164–180.

Koenig, S.H., Brown, R.D., 3rd, Spiller, M., Lundbom, N., 1990. Relaxometry of brain: why white matter appears bright in MRI. Magn. Reson. Med. 14, 482–495.

Lanzilotto, M., Perciavalle, V., Lucchetti, C., 2013. Auditory and visual systems organization in Brodmann Area 8 for gaze-shift control: where we do not see, we can hear. Front. Behav. Neurosci. 7, 198.

Laule, C., Kozlowski, P., Leung, E., Li, D.K.B., Mackay, A.L., Moore, G.R.W., 2008. Myelin water imaging of multiple sclerosis at 7 T: correlations with histopathology. Neuroimage 40, 1575–1580.

Lee, J., Shmueli, K., Kang, B.-T., Yao, B., Fukunaga, M., van Gelderen, P., Palumbo, S., Bosetti, F., Silva, A.C., Duyn, J.H., 2012. The contribution of myelin to magnetic susceptibility-weighted contrasts in high-field MRI of the brain. Neuroimage 59, 3967–3975.

Lee, J., van Gelderen, P., Kuo, L.-W., Merkle, H., Silva, A.C., Duyn, J.H., 2011. T_2*-based fiber orientation mapping. Neuroimage 57, 225–234.

Levesque, I.R., Pike, G.B., 2009. Characterizing healthy and diseased white matter using quantitative magnetization transfer and multicomponent T2 relaxometry: A unified view via a four-pool model. Magn. Reson. Med. 62, 1487–1496.

Li, D., Wang, Y., Waight, D.J., 1998. Blood oxygen saturation assessment in vivo using T_2* estimation. Magn. Reson. Med. 39, 685–690.

Li, T.-Q., van Gelderen, P., Merkle, H., Talagala, L., Koretsky, A.P., Duyn, J., 2006. Extensive heterogeneity in white matter intensity in high-resolution T_2*-weighted MRI of the human brain at 7.0 T. Neuroimage 32, 1032–1040.

Li, T.-Q., Yao, B., van Gelderen, P., Merkle, H., Dodd, S., Talagala, L., Koretsky, A.P., Duyn, J., 2009. Characterization of T_2* heterogeneity in human brain white matter. Magn. Reson. Med. 62, 1652–1657.

Mainero, C., Govindarajan, S.T., Kinkel, P.R., Nielsen, A.S., Cohen-Adad, J., 2012. A gradient in cortical T_2* relaxation decay changes at 7 Tesla MRI in patients with multiple sclerosis, in: ISMRM. p. 6158.

Mottershead, J.P., Schmierer, K., Clemence, M., Thornton, J.S., Scaravilli, F., Barker, G.J., Tofts, P.S., Newcombe, J., Cuzner, M.L., Ordidge, R.J., McDonald, W.I., Miller, D.H., 2003. High field MRI correlates of myelin content and axonal density in multiple sclerosis. J. Neurol. 250, 1293–1301.

Nieuwenhuys, R., 2013. The myeloarchitectonic studies on the human cerebral cortex of the Vogt-Vogt school, and their significance for the interpretation of functional neuroimaging data. Brain Struct. Funct. 218, 303–352.

Pike Bruce, G., 1996. Pulsed Magnetization Transfer Contrast in Gradient Echo Imaging: Two-Pool Analytic Description of Signal Response. Magn Reson Med.

Pistorio, A.L., Hendry, S.H., Wang, X., 2006. A modified technique for high-resolution staining of myelin. J. Neurosci. Methods 153, 135–146.

Pitt, D., Boster, A., Pei, W., Bs, E.W., Bs, A.J., Zachariah BS, C.R., Rammohan, K., Knopp, M.V., Schmalbrock, P., 2010. Imaging Cortical Lesions in Multiple Sclerosis With Ultra–High-Field Magnetic Resonance Imaging. Arch Neurol, 812–818.

Postelnicu, G., Zollei, L., Fischl, B., 2009. Combined volumetric and surface registration. IEEE Trans. Med. Imaging 28, 508–522.

Preibisch, C., Deichmann, R., 2009. Influence of RF spoiling on the stability and accuracy of T_1 mapping based on spoiled FLASH with varying flip angles. Magn. Reson. Med. 61, 125–135.

Reuter, M., Rosas, H.D., Fischl, B., 2010. Highly accurate inverse consistent registration: a robust approach. Neuroimage 53, 1181–1196.

Sati, P., Silva, A.C., van Gelderen, P., Gaitan, M.I., Wohler, J.E., Jacobson, S., Duyn, J.H., Reich, D.S., 2012. In vivo quantification of T_2* anisotropy in white matter fibers in marmoset monkeys. Neuroimage 59, 979–985.

Schmierer, K., Scaravilli, F., Altmann, D.R., Barker, G.J., Miller, D.H., 2004. Magnetization transfer ratio and myelin in postmortem multiple sclerosis brain. Ann. Neurol. 56, 407–415.

Schmierer, K., Tozer, D.J., Scaravilli, F., Altmann, D.R., Barker, G.J., Tofts, P.S., Miller, D.H., 2007. Quantitative magnetization transfer imaging in postmortem multiple sclerosis brain. J. Magn. Reson. Imaging 26, 41–51.

Schmierer, K., Wheeler-Kingshott, C.A.M., Tozer, D.J., Boulby, P.A., Parkes, H.G., Yousry, T.A., Scaravilli, F., Barker, G.J., Tofts, P.S., Miller, D.H., 2008. Quantitative magnetic resonance of postmortem multiple sclerosis brain before and after fixation. Magn. Reson. Med. 59, 268–277.

Sereno, M.I., 1991. Language And The Primate Brain, in: Proceedings Thirteenth Annual Conference of the Cognitive Science Society.

Sereno, M.I., Lutti, A., Weiskopf, N., Dick, F., 2013. Mapping the human cortical surface by combining quantitative T(1) with retinotopy. Cereb. Cortex 23, 2261–2268.

Sigalovsky, I.S., Fischl, B., Melcher, J.R., 2006. Mapping an intrinsic MR property of gray matter in

auditory cortex of living humans: a possible marker for primary cortex and hemispheric differences. Neuroimage 32, 1524–1537.

Spees, W.M., Yablonskiy, D.A., Oswood, M.C., Ackerman, J.J.H., 2001. Water Proton MR Properties of Human Blood at 1.5 Tesla: Magnetic Susceptibility, T_1, T2, T*2, and Non- Lorentzian Signal Behavior. Magn. Reson. Med. 45, 533–542.

Stüber, C., Morawski, M., Schäfer, A., Labadie, C., Wähnert, M., Leuze, C., Streicher, M., Barapatre, N., Reimann, K., Geyer, S., Spemann, D., Turner, R., 2014. Myelin and iron concentration in the human brain: a quantitative study of MRI contrast. Neuroimage 93 Pt 1, 95–106.

Tardif, C.L., Bedell, B.J., Eskildsen, S.F., Collins, D.L., Pike, G.B., 2012. Quantitative magnetic resonance imaging of cortical multiple sclerosis pathology. Mult. Scler. Int. 2012, 742018.

Van der Kouwe, A.J.W., Benner, T., Salat, D.H., Fischl, B., 2008. Brain morphometry with multiecho MPRAGE. Neuroimage 40, 559–569.

Van Essen, D.C., 2005. A Population-Average, Landmark- and Surface-based (PALS) atlas of human cerebral cortex. Neuroimage 28, 635–662.

Vogt, O., 1911. Die Myeloarchitectonik des Isocortex parietalis. Journal für Psychologie und Neurologie 18, 379–390.

Xie, L., Wu, J., 2006. Global optimal ICA and its application in MEG data analysis. Neurocomputing 69, 2438–2442.

Zwanenburg, J.J.M., Versluis, M.J., Luijten, P.R., Petridou, N., 2011. Fast high resolution whole brain T_2* weighted imaging using echo planar imaging at 7T. Neuroimage 56, 1902–1907.

CHAPTER 5 SUPPLEMENTARY METHODOLOGICAL INFORMATION

5.1 Comparison between 7T T_2* and 3T MTR in the in vivo human cortex, ISMRM 2014.

This section presents the abstract of a poster presentation investigating the feasibility to combine 7T T_2* and MTR in the cortex, it has been published in June 2014, at the conference ISMRM. (before the Article 1). Please note that the Tables and Figures will have the suffix 5- (i,.e. CHAPTER 5) before their actual number, because the document formmating had to be respected.

Authors

Gabriel MangeaT_1, Sindhuja T. Govindarajan[2], Caterina Mainero[2], and Julien Cohen-Adad[1]

Affiliations

[1]Biomedical institute, Ecole Polytechnique de Montreal, Montreal, Qc., Canada,

[2]A.A. Martinos Center for Biomedical Imaging, MGH, Harvard Medical School, MA, United States

5.1.1 Purpose

Characterization of cortical myelo-architecture with MRI is an active field of research[1], which can give insights on the structural and functional organization of the brain. It is however challenging to image the cortex due to its convoluted and thin geometry (2- 4mm). Recently, ultra-high field MRI (7T) combined with T_2* was shown to reveal features of myelin density[2]. However, several confounds hamper the specificity of T_2* measures such as iron content and blood vessels[3]. An independent measure with different contrast mechanisms would increase the specificity to myelin. Magnetization Transfer Ratio (MTR) imaging at 3T was shown to be sensitive to myelin content4 and thus would be an excellent complementary measure. The goal of this study was to

evaluate the relationship between T_2* at 7T and MTR at 3T, and show their respective sensitivity and specificity to myelin content.

5.1.2 Methods

5.1.2.1 Data acquisition.

Healthy subjects (N=6, age = 36 +/- 5 years) were recruited and scanned with a 7T whole-body scanner (Siemens Healthcare, Erlangen, Germany) to measure T_2* and with a 3T scanner (Siemens TIM Trio) to measure MTR. Both scanners were equipped with a 32-channel coil. Parameters at 7T were: TR = 2020ms, TE = 6.34+3.2n [n=1...12], resolution = 0.33x0.33x1mm3. Parameters at 3T were: 3D FLASH, TR/TE = 30/2.49ms, matrix = 192x192, resolution=1.2x1.2x1.2 mm3, with and without Gaussian MT pulse (7:45min each).

5.1.2.2 Data processing.

T_2* and MTR data were registered to individual cortical surfaces, sampled at the mid-cortical distance and registered to a common template surface5. Data were first averaged in the common space and SD maps were computed to assess inter-subject variability. A linear regression between the mean T_2* and MTR maps was performed for each hemisphere, as well as within Brodmann regions with different myelin content.

5.1.3 Results

Average and SD maps of T_2* and MTR are shown in **Fig. 1**. SD map of T_2* show high variability in the lower brain, likely due to poor shimming in this region. Conversely, SD of MTR shows fairly good reproducibility (mean SD = **1.59%**). **Fig. 2** shows the relationship between T_2* and MTR. Strong correlations in the right (r=-0.77) and left (r=- 0.75) hemispheres were detected. To verify if partial volume effect affected our measures, cortical thickness was correlated with these measures and showed low effect (r=0.14 and r=-0.09 for T_2* and MTR, respectively). **Fig. 3** shows the mean values of T_2* and MTR for the Brodmann regions (B1, B2, B3, B4, B43 and B44), sorted by T_2* values. Once again, T_2* and MTR are highly anti-correlated.

Fig. 4 is a supplementary figure from the poster, it shows the map of Pearson's correlation coefficients between MTR andT_2* calculated within Brodmann areas, as well as the behiviour of MTR and T_2* in various Brodmann areas.

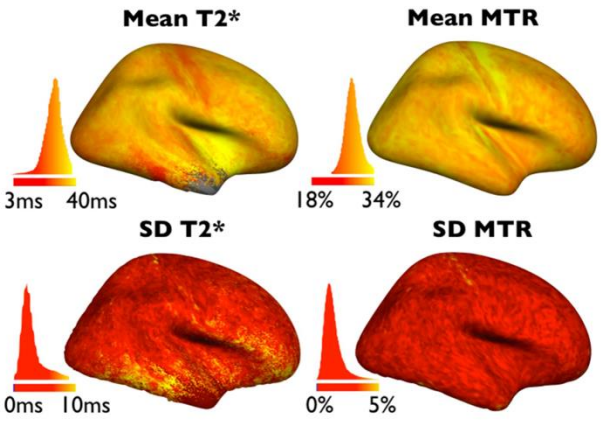

Figure 5-1**.** Mean and SD maps between the six controls for the T_2* metric (left) and the MTR values (right). Mean maps (top) shows an increase in MTR and a decrease in T_2* in the central sulcus.

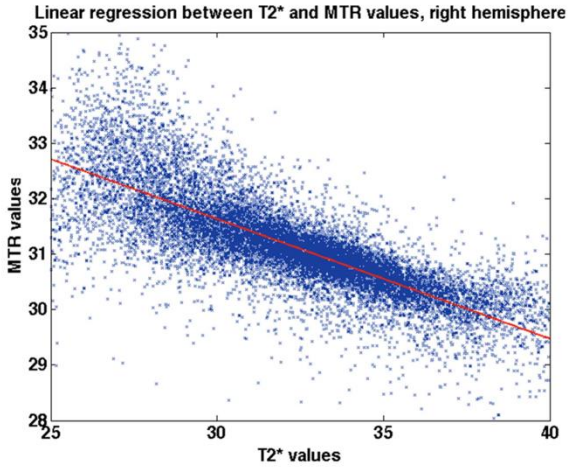

Figure 5-2. Linear regression between T_2* and MTR vertices values. The Pearson's correlation coefficient for this regression is r=-0.77.

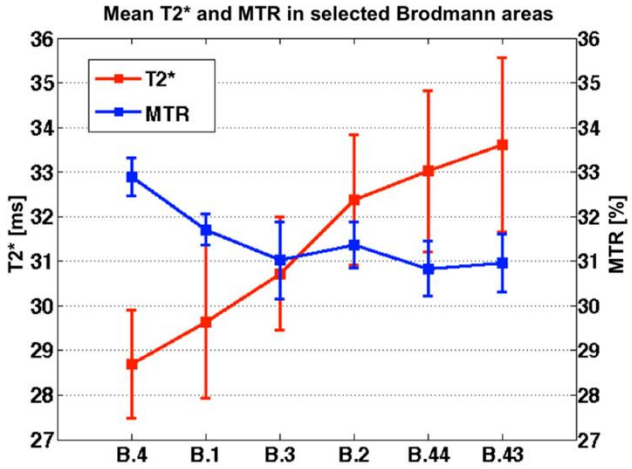

Figure 5-3. Mean values of T_2* and MTR across Brodmann regions with different myelin content. Data are averaged between the six controls. Error bars represent SD across subjects.

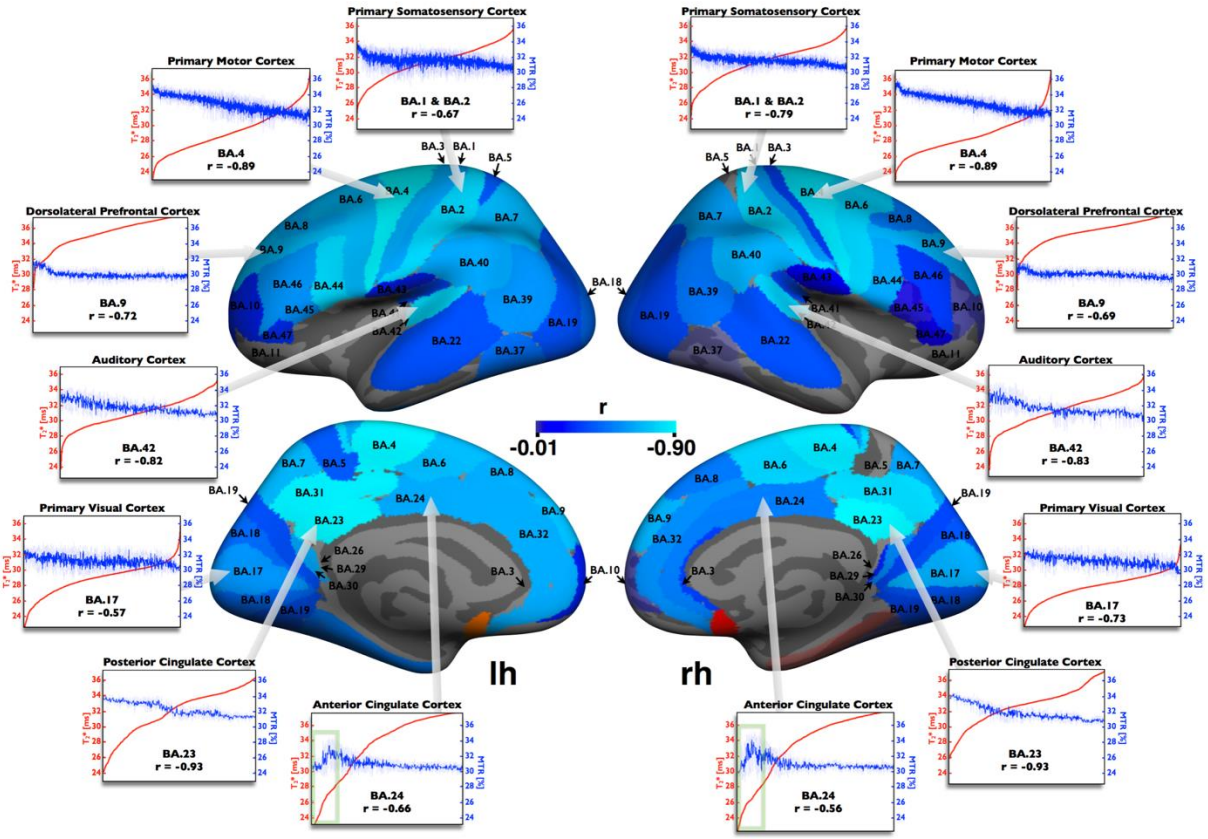

Figure 5-4. Map of Pearson's correlation coefficients between MTR andT_2* calculated within Brodmann areas. Repartition graphs are shown for selected regions. Once again, the right-left reproducibility is high, however we note that correlations are slightly higher on the left hemisphere. Overall, we note that correlations are negative, meaning that MTR increases where T_2* decreases.

Regions with high correlations (BA.2, BA.4, BA.6, BA.23 and BA.43) are known to be highly myelinated. However, the repartition graphs show slight differences amongst them, which could be attributed by specific features of myeloarchitecture. For example the repartition graphs for the *anterior cingulate cortex* show distinctive features, i.e., part of the *anterior cingulate cortex* shows MTR and T_2* that co-vary (instead of being anticorrelated, see green square). This might be due to the level of tissue iron that T_2* is sensitive to [1].

5.1.4 Discussion

Our results show within the same subjects an increase of T_2* and a decrease of MTR, in regions that are known to be heavily myelinated (e.g., B4, B1). These trends were expected given the sensitivity of T_2* and MTR to myelin content. However, this is the first time these two metrics are combined within the same subjects, providing a framework to isolate confounding parameters affecting T_2* (iron, issue orientation, poor shimming) and MTR (B1 inhomogeneities, T_1). Combining other metrics (quantitative T_1, diffusion, T2w/T_1w) within the same methodological framework could potentially bring more insight into cyto- and myeloarchitecture than if these metrics were studies separately.

5.1.5 References

1. J. Lee, et al. The contribution of myelin to magnetic susceptibility-weighted contrasts in high-field MRI of the brain. Neuroimage. *2012;* vol. 59, pp. 3967-75.

2. J. Cohen-Adad, et al. T_2* mapping and B_0 orientation-dependence at 7 T reveal cyto- and myeloarchitecture organization of the human cortex. NeuroImage. 2012. 1006-1014.

3. M. Fukunaga et al. Layer Aspecific variation of iron content in cerebral cortex as a source of MRI contrast. PNAS. 2010; USA 107, 3834A3839

4. I.R. Levesque and G.B. Pike, Characterizing healthy and diseased white matter using quantitative magnetization transfer and multicomponent T(2) relaxometry: A unified view via a four-pool model. *Magn Reson Med.* 2009; vol. 62, pp. 1487-96.

5. J. Cohen-Adad, What can we learn from T_2* maps of the cortex? NeuroImage. 2013.

5.1.6 Acknowledgments

This work was supported by the National Multiple Sclerosis Society [FG 1892A1/1, 4281-RG-A-1], by the National Center for Research Resources [P41-RR14075], by the Fonds de Recherche du Québec - Santé (FRQS), by the Quebec BioImaging Network (QBIN) and by the Natural Sciences and Engineering Research Council of Canada (NSERC) and by the Polytechnique MEDITIS program.

CHAPTER 6 SUPPLEMENTARY PUBLISHED WORK : APPLICATIONS IN MULTIPLE SCLEROSIS

6.1 Multivariate combination of magnetization transfer ratio and quantitative T_2* to detect subpial demyelination in multiple sclerosis, ISMRM 2015

This section presents the abstract of an oral presentation investigating the ability of the combined contrast to detect cortical changes in MS patients, it has been presented in June 2015, at the conference ISMRM (after the Article 1). This presentaion won an ISMRM Mertit Award: *Magna Cum Laude.* Please note that the Tables and Figures will have the suffix 6- (i,.e. CHAPTER 6) before their actual number, because the document formmating had to be respected.

Authors

G. Mangeat [1], S. T. Govindarajan [3], R. P. Kinkel[5], C. Mainero [3,4], J. Cohen-Adad [1,2]

Affiliations

[1] Institute of Biomedical Engineering, Polytechnique Montreal, Montreal, QC, Canada

[2] Functional Neuroimaging Unit, CRIUGM, Université de Montréal, Montreal, QC, Canada

[3] Athinoula A. Martinos Center for Biomedical Imaging, MGH, Charlestown, MA, USA

[4] Harvard Medical School, Boston, MA, USA 5 Beth Israel Deaconess Medical Center, Boston, MA, USA

Synopsis

We introduce a multivariate statistical framework for combining cortical sampling of MTR and T_2* to gain specificity for mapping cortical myelin content. (i) We sampled cortical MTR and T_2* from *Freesurfer* segmentation. (ii) we normalized MTR and T_2* maps and corrected them for partial volume effect and B_0 orientation. (iii) we extracted the shared myelin information using a

spatial independent component analysis. We demonstrate the benefits of this framework for separating healthy controls from subject with multiple sclerosis on the basis of cortical pathology.

6.1.1 Target audience

Scientists and clinicians interested to the cortex mapping related to the myelin content and applied to the subpial demyelination in multiple sclerosis.

6.1.2 Purpose

The ability to assess in vivo subpial demyelination in multiple sclerosis (MS) is motivated by improved correlation with functional deficits and for understanding the pathophysiology of the disease [1,2]. In vivo detection of cortical subpial lesions, however, is challenging due to the thin aspect of the cortex (2-4 mm) and to the low contrast using standard clinical MR contrasts. Recently, T_2* at 7 Tesla was shown to be a sensitive biomarker of pathology and disease progression associated with demyelination in the cortex of MS patients[1,3]. However, several physiological and technical confounds (i.e. iron content, blood vessels and poor shimming) may hamper the specificity of T_2* measures. Magnetization Transfer Ratio (MTR) imaging was demonstrated to be sensitive to myelin content4 and cortical myelin changes in MS[5,6], potentially being an excellent complementary measure to T_2* estimation even more given that its underlying contrast mechanisms are different than those from T_2*. Additional confounds exist that can affect cortical mapping studies, including (i) the effect of cortical thickness, which can introduce variable amount of partial volume effect, and (ii) the angle between coherently-oriented myelinated fibers in the cortex and the direction of the main magnetic field (B_0)[7]. The goal of this study was to use multivariate statistics to combine cortical MTR (from 3T) and T_2* (from 7T) measurements, cortical thickness, and B_0 orientation dependency measure using a surface-based analysis framework in order to gain specificity to subpial demyelination in MS.

6.1.3 Methods

Data acquisition. We recruited 6 healthy subjects (mean age=36 +/- 5 years, 3 females) and 11 MS patients (mean age 46 +/- 12 years, 8 females). Subjects were scanned with a 7T whole-body Siemens scanner to measure T_2* and on a 3T scanner (Siemens TIM Trio) to measure MTR. MTR was not acquired at 7T due to difficulties in obtaining homogeneous B1 profile and SAR

limitations. Both scanners were equipped with a 32- channel coil. Parameters at 7T were: TR = 2020 ms, TE = 6.34+3.2n [n=0,...,11] ms, resolution = 0.33x0.33x1 mm^3. Parameters at 3T were: 3D FLASH, TR/TE = 30/2.49 ms, matrix = 192x192, resolution = 1.2x1.2x1.2 mm^3, with and without Gaussian MT pulse (7:45 min each). *Data processing.* T_2* and MTR data were (*i*) registered to individual cortical surfaces (extracted from 3 T T_1-weighted anatomical scans), (*ii*) sampled along the cortical ribbon at the mid distance between the pial surface and the white matter surface and (*iii*) registered to a common template surface (*fsaverage*). Cortical thickness and B_0 orientation maps were computed from the cortical surface of each subject as previously detailed7. *Multivariate combination.* First, multilinear regressions were performed using predictors of myelin content (MTR and T_2*) and potentially confounding covariates (cortical thickness and B_0 orientation). The outputs of this step were 2 normalized maps representing the myelin-related information contained in MTR and T_2*, and corrected for partial volume effect and B_0 orientation. A spatial independent component analysis (ICA)[8] was subsequently used to extract the shared myelin-related signal

between MTR and T_2*. The result was a Combined Myelin Estimation (CME) map that reflected the cortical myelin content of each subject with more specificity than MTR or T_2* maps taken separately. All steps are summarized in **Figure 1**. *Statistical analysis.* General Linear Models (GLM) were run on a vertex-by-vertex basis to assess regions of significant differences ($p<0.05$) between controls and MS patients, for each of the following metric: MTR, T_2* and CME. The following regressors were used: age, gender and mean cortical thickness. *Specificity/Sensitivity assessment using Receiver Operating Characteristics (ROC) curves.* Cortical regions that are known to be preferentially affected by subpial demyelination in MS[1,2,6] were selected out of the V1 atlas[9]: primary motor cortex (BA4a and BA4p), somatosensory cortex (BA1 and BA2), and pre-motor cortex (BA6). Then, from the inter-group distributions of each metric (MTR, T_2* and CME), the ROC curves were computed.

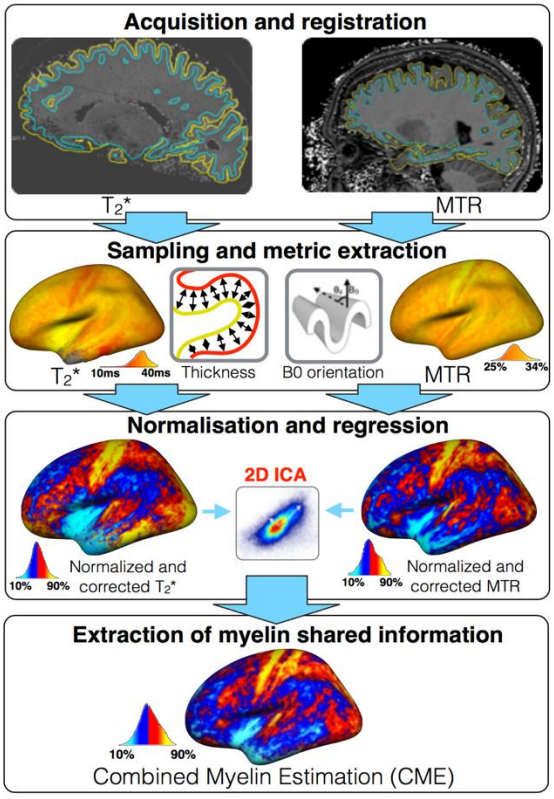

Figure 6-1. Processing steps applied to combine the cortical information of 7T T_2*, 3T MTR and B_0 orientation in order to extract a metric more specific to myelin than other metric taken separately.

6.1.4 Results

Figure 2A shows the results of the GLM performed for T_2*, MTR and CME. Significant differences ($p<0.05$, not corrected) between both groups were detected in the motor cortex and in the frontal lobe. **Figure 2B** shows a zoom in the posterior primary motor cortex: BA4p (regions selected for the ROC analysis), illustrating the greater z-score for the CME metric (other regions exhibited similar large z-score in the CME map). **Figure 2C** represents the distributions of the metrics in BA4p for the controls group (blue) and the MS group (red). **Figure 2D** shows the resulting ROC curve for each metric, suggesting a potential gain in specificity and sensitivity for the CME map. For example, for a given sensitivity of 60%, the specificity of pathological-related change in this cortical region is 53%, 40% and 66% for MTR, T_2* and CME, respectively. **Figure 3** shows the gain in specificity for other cortical regions.

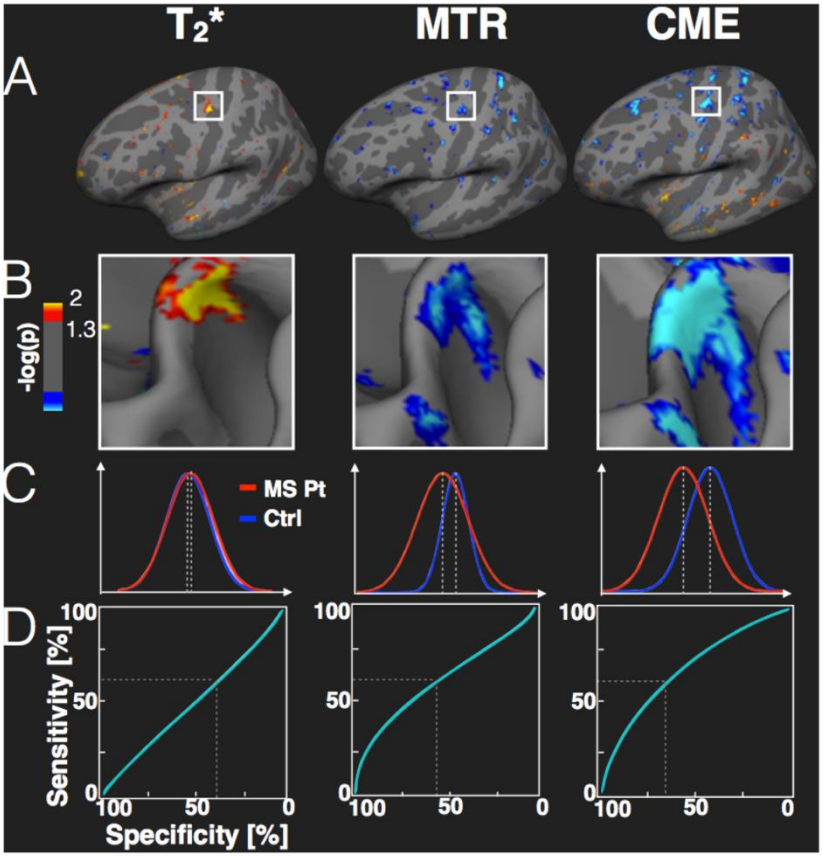

Figure 6-2. A. Overlay f the GLM significance maps averaged on the mid-cortical surface. B. Zoom in the lower precentral gyrus (part of BA4). C. Distribution of both control and MS patient groups in BA4p. D. ROC curves of the distributions in C.

	T2*	MTR	CME		T2*	MTR	CME
BA4a	40%	53%	62%	**BA1**	40%	54%	60%
BA2	40%	59%	61%	**BA6**	40%	57%	60%

Figure 6-3. Specificity of the subject classification from the assessment of the subpial demyelination in the selected cortical regions, assuming a sensitivity of 60%.

Figure 4 and Figure 5 are supplementary figures from the actual presentation. **Figure 4** shows MTR map, T_2* map and CME map, averaged across controls. And **Figure 5** shows the result of a HC *vs* MS GLM performed on BA basis and using the regressors: gender, age and mean cortical thickness.

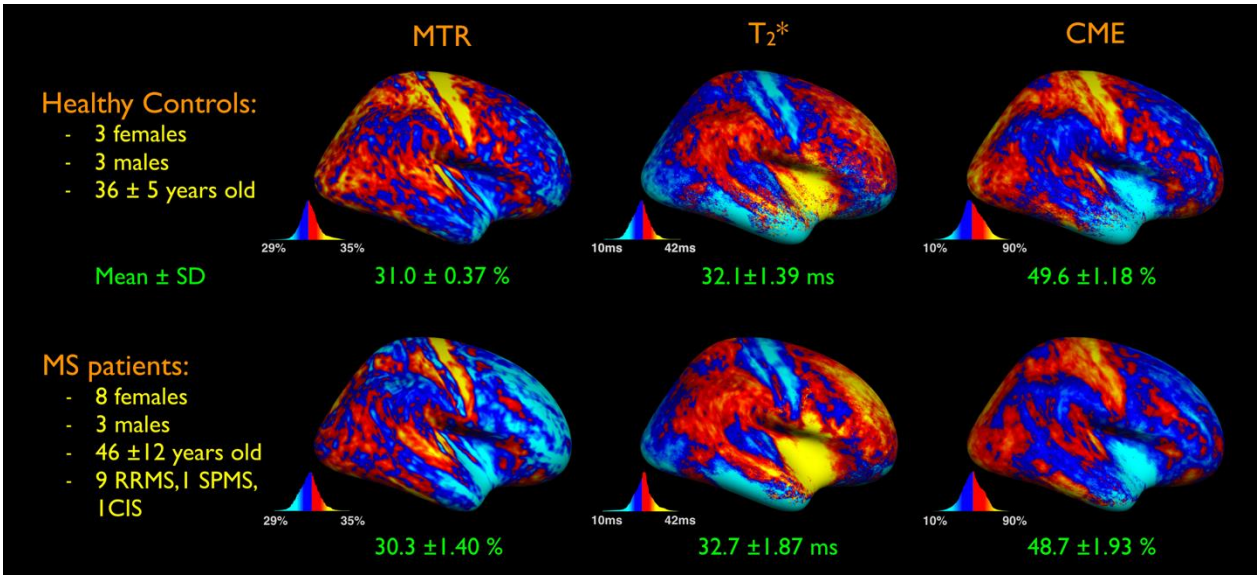

Figure 6-4. MTR map, T_2* map and CME map, averaged across controls. An average decrease of signal between both MTR group maps is observed, which is consistent with a cortical demylination because MTR is proportional to myelin content. T_2* is inversely proportional to myelin content, and as expected we observe an increase if signal. CME should be proportional to the amount of myelin, and again, as expected we observe a decrease of signal. All these results suggest subpial demyelination, but, are the observed variations significant?

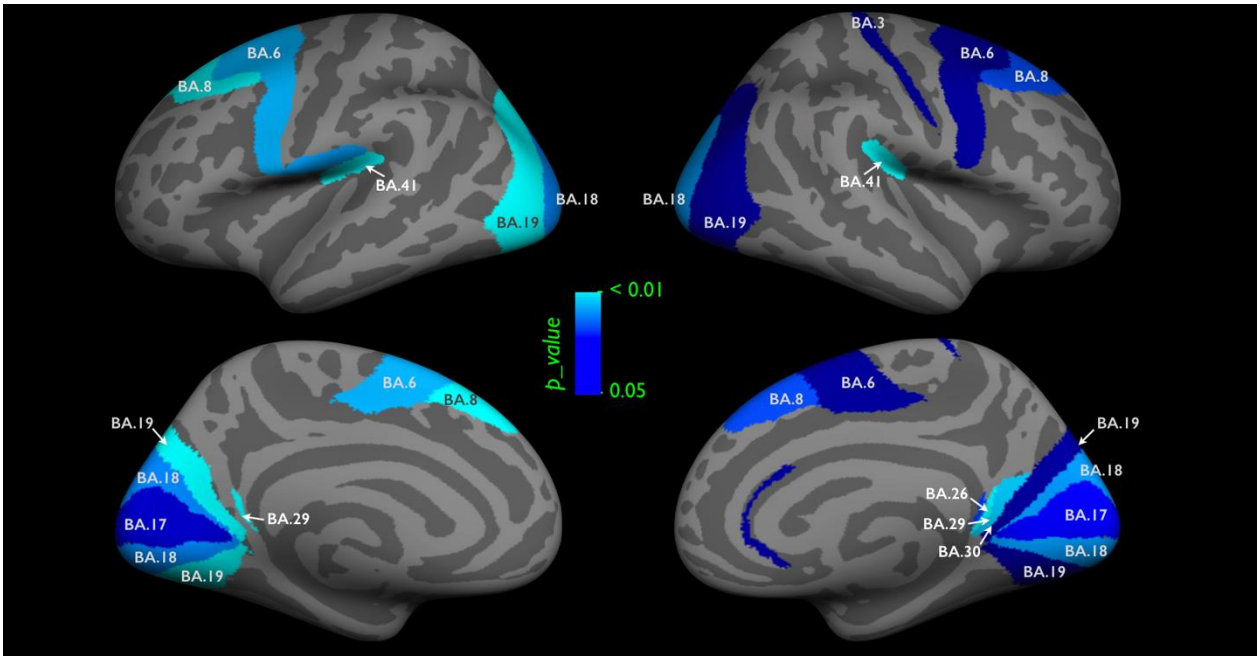

Figure 6-5. Result of a HC *vs* MS GLM performed on BA basis and using the regressors: gender, age and mean cortical thickness. Some significant differences in prefrontal and motor, visual and auditory cortices are observed. We also notice a higher level of significance in LH.

6.1.5 Discussion

We introduced a multivariate statistical framework for combining MTR and T_2* measures in order to gain specificity to myelin content. We demonstrate its benefits for separating healthy controls from MS patients on the basis of cortical pathology. The framework is adaptable in that other relevant metrics such as T_1 and diffusion-weighted measures can be added to the model.

6.1.6 References

[1]Cohen-Adad, *Neuroimage*, 2011; [2]Kutzelnigg, *Brain*, 2005; [3]Mainero, *Neurology*, 2009; [4]Schmierer, *Ann Neurol*, 2004; [5]Chen, *Neurology*, 2013; [6]Deraksan, *Hum Brain Mapp*, 2014; [7]Cohen- Adad, *Neuroimage*, 2012; [8]Hyvärinen, *Int J Neural Syst*, 2000; [9]Fischl, *Cereb Cortex*, 2008;

6.1.7 Acknowledgements

This work was supported by the National Multiple Sclerosis Society [FG 1892A1/1, 4281-RG-A-1], by the National Center for Research Resources [P41-RR14075], by the Fonds de

Recherche du Québec - Santé (FRQS), by the Quebec BioImaging Network (QBIN) and by the Natural Sciences and Engineering Research Council of Canada (NSERC) and by the Polytechnique MEDITIS program.

6.2 Multivariate combination of quantitative T_2* and T_1 at 7T MRI detects in vivo subpial demyelination in the early stages of MS, ECTRIMS 2015

This section presents the abstract of a poster presentation investigating the ability of the combined contrast to detect cortical changes a cohort of early MS patients (disease duration <3 years), it has been published in October 2015, at the conference ECTRIMS.

Authors

G. MangeaT_1,[2], C. Louapre[2,3], E. Herranz[2,3], C.A. Treaba[2,3], R. Ouellette[2], J.A. Sloane[3,4], E.C. Klawiter[2,3,5], J. Cohen-Adad[1,6], C. Mainero[2,3]

Affiliations

[1]Institute of Biomedical Engineering, Polytechnique Montreal, Montreal, QC, Canada,

[2]A. A. Martinos Center for Biomedical Imaging, MGH, Charlestown,

[3]Harvard Medical School,

[4]Beth Israel Deaconess Medical Center,

[5]Department of Neurology, MGH, Boston, MA, United States,

[6]Functional Neuroimaging Unit, CRIUGM, Université de Montréal, Montreal, QC, Canada

6.2.1 Background and goals

Subpial demyelination occurs early in the course of multiple sclerosis (MS), but *in vivo* detection is challenging due to low contrast at conventional field strengths. Quantitative mapping

of T_2* and T_1 relaxation rates at 7T MRI was shown to be sensitive to cortical myelin content, and to cortical MS demyelination associated with clinical measures. Given that several confounds hamper the specificity of both metrics, we used multivariate statistics to combine cortical T_1 and T_2* maps to gain specificity to subpial demyelination in early MS. This approach has shown improved sensitivity to cortical myelin content in healthy subjects.

6.2.2 Methods

Acquisition: In 5 healthy controls (HC, 34±12 years, 3 females) and 10 early MS patients (37±9 years; 8 females; disease duration≤3 years, median =1, range Expanded Disability Status Scale score = 0-3) we obtained 7T high resolution quantitative T_2* (0.5x0.5x0.5mm3) and T_1 (0.75x0.75x0.75mm3) maps. For each subject, T_1 and T_2* were sampled at 25%, 50% and 75% depth from the pial surface. Scan parameters were: TR/ TE=3680/3.12+3.32*[1..6]ms for T_2* and MP2RAGE sequence, double inversion gradient echo, TR/TE/TI=5000/2.93/[900 3200]ms for T_1.

Processing: For each subject, T_1 and T_2* were sampled at 25%, 50% and 75% depth along the cortex (Pial = 0%;WM = 100%)**.** Then, we applied a first order correction for partial volume effect to both metrics and a spatial Independent Component Analysis was used to extract the shared myelin related signal in T_1 and T_2* maps thus creating the Combined Myelin Estimation (CME), a new metric more specific to myelin than T_1 or T_2* separately, as previously done in.

Statistics: A General Linear Model (GLM), including age and gender as adjustment factors, was used to compare T_1, T_2* and CME in MS patients vs healthy controls in whole cortex and in selected Brodmann areas (BA).

6.2.3 Results

In the whole cortex, CME was increased while T_1 and T_2* were decreased in MS vs HC (CME=47±0.8% vs 49±1.3%; T_1=1727±56 vs 1654±70 ms; T_2*=34.0±1.2 vs 33.0±1.1 ms). Whole cortex GLM of CME showed significant loss of myelin ($p< 0.05$), though variations of T_2* and T_1 were not significant. The GLM of CME within BAs showed significant loss of myelin in sensory, motor (BA3, BA4, BA6) and prefrontal (BA10) areas ($p< 0.05$). A significant higher T_1 was observed in frontal cortex (BA45, $p< 0.05$). No regions were significantly different using T_2*.

Figure 6-6 and Figure 6-7 are supplementary figures from the actual poster. Figure 6-6 shows CME maps averaged across groups (HC and MS). Figure 6-7 shows the result of the GLM comparing HC *vs* MS, performed on BA basis, and using the regressors: gender, age and mean cortical thickness.

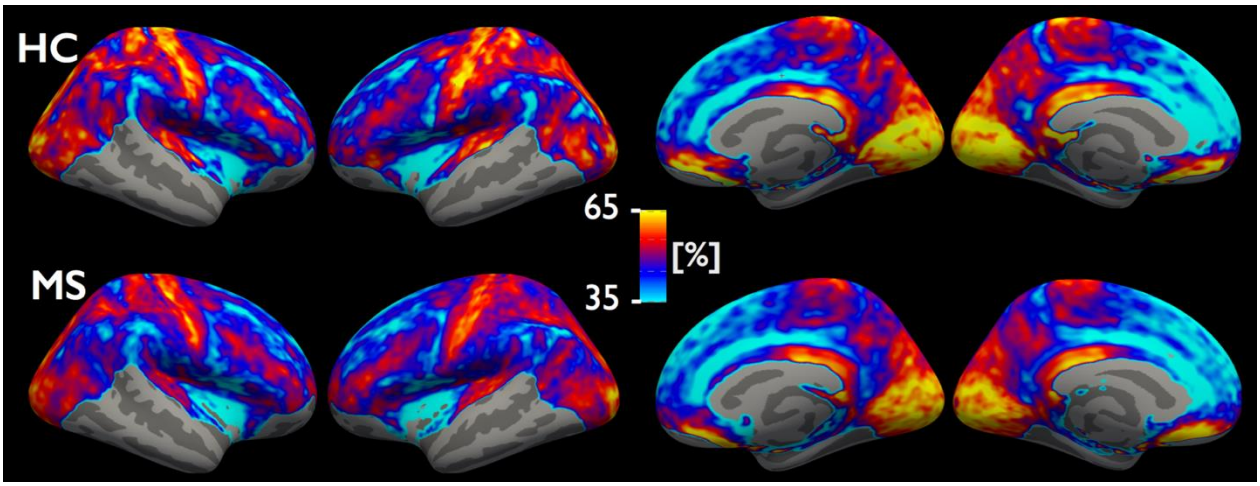

Figure 6-6. Myelin estimated maps averaged across HC and MS groups. We can visually observe a qualitative loss of myelin around the motor, visual and auditory cortices. Quantitatively, in the whole cortex, CME was decreased while T_1 and T_2* were increased in MS vs HC: CME=47±0.8% vs 49±1.3%; T_1=1727±56ms vs 1654±70ms; T_2*=34.0±1.2ms vs 33.0±1.1ms).

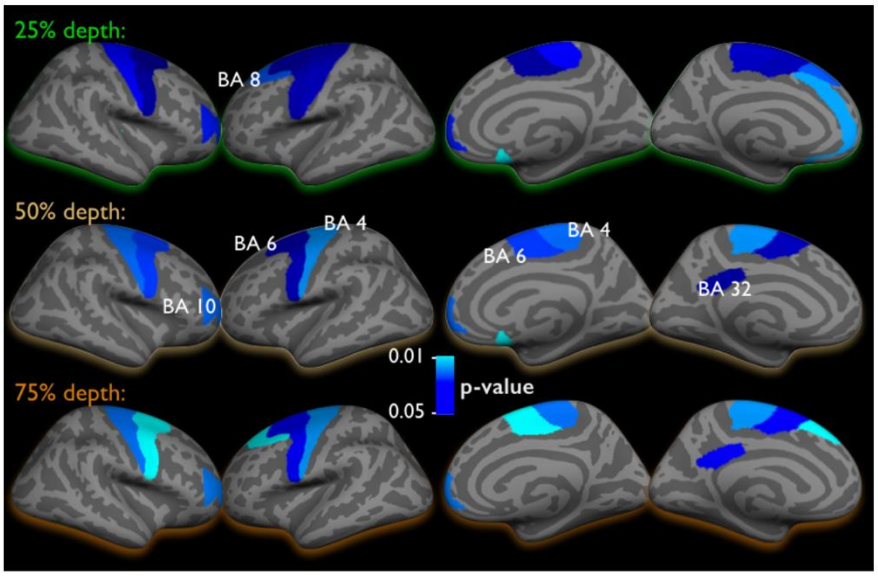

Figure 6-7. Result of the GLM comparing HC *vs* MS, performed on BA basis, at three cortical depths. Significant loss of myelin in sensory, motor (BA3, BA4, BA6) and prefrontal (BA10) areas

($p< 0.05$). Significantly higher T_1 was observed in frontal cortex (BA45, $p< 0.05$). No regions were significantly different using T_2*.

6.2.4 Discussion

CME, a multivariate statistical framework combining quantitative T_1 and T_2* from ultra high resolution 7T scans, i) shows increased specificity to detect changes in early MS compared to HC, ii) supports subpial demyelination as an early event in MS, even in the presence of mild neurological disability.

6.2.5 Disclosure

The study was funded by R01 NS078322-03 - **G. Mangeat:** nothing to disclose. - **C. Louapre:** has received a fellowship from ARSEP foundation. - **E. Harranz:** nothing to disclose. - **C. A. Treaba:** nothing to disclose. - **R. Ouellette:** nothing to disclose. - **J. A. Sloane:** nothing to disclose. - **E. C. Klawiter:** has received consulting fees from Biogen Idec and Mallinckrodt Pharmaceuticals and research funding from Roche and Atlas5d. - **J. Cohen-Adad:** nothing to disclose. - **C. Mainero:** nothing to disclose.

CHAPTER 7 GENERAL DISCUSSION

This work presented a novel approach to combine several MRI modalities sensitive to myelin in the *in-vivo* human cortex. The combination framework is based on the principle of signal decomposition using minimisation of gaussianity. The framework pre-processing includes a normalisation, a first order correction of partial volume effects and a correction to tissue orientation with respect with B_0. The extracted components are then de-normalized in order to be able to perform group statistics amongst them. The gain in myelin specificity of the extracted components has been validated using simulations and previous histology works. The method was then applied on MS patients in order to study their cortical variations of myeloarchitecture. So far, two groups of MS patients have been studied with the above method. A *classic* cohort and an *early* cohort (disease duration < 3years), MS vs HC numbers were respectively 6 HC vs 11 MS and 5 HC vs 10 MS. In both cases the combined myelin maps leads to detect significant demyelination areas in various cortical regions while standard metrics couldn't.

The choice of the MR modalities to be combined was first based on previous literature review demonstrating the potential of both metrics to image myelin in the cortex. Then, a deeper analysis of i) the mechanisms of both modalities, ii) their respective behaviour in the cortex iii) their mutual interplay in various cortical areas, was performed to ensure the quality of the future combination. This preliminary work led to a presentation of a poster at the conference ISMRM 2014. This poster was entitled: *Comparison between 7T* T_2* *and 3T MTR in the in vivo human cortex.* , presented in CHAPTER 5.

Once the relevance of the combination was demonstrated, several ideas and algorithms were tested to effectively extract the main information of myelin contained in both modalities. An ICA-based algorithm was revealed to be the best compromise between robustness, reproducibility and calculus time. Following the development of the combination framework, and its validations, a scientific article was published in the journal *NeuroImage*: *Multivariate combination of magnetization transfer,* T_2* *and* B_0 *orientation to study the myelo-architecture of the in vivo human cortex.* , presented in CHAPTER 4. This new tool being available, its application to study MS patients could start. A first study comparing the ability of the combined metric to detect cortical demyelination relatively to standard metrics was performed. It resulted in a presentation at the conference ISMRM 2015: *Multivariate combination of magnetization transfer ratio and*

quantitative T_2* *to detect subpial demyelination in multiple sclerosis.* , presented in CHAPTER 6. As this study revealed the benefits of the combined metric to study MS patients, a second study was performed in a cohort of early MS patients, for whom the cortical demyelination is more subtle. This study was presented at the conference ECTRIMS 2015: *Multivariate combination of quantitative* T_2* *and* T_1 *at 7T MRI detects in vivo subpial demyelination in the early stages of MS. , presented in CHAPTER 6.*

However, while these studies have demonstrated cogent improvements, they come with some limitations and points to be ideally improved. The Article 1's discussion relates mainly of the interpretation and topology of the resulting myeloarchitectural map, the choice of the combined contrasts and the comparison with similar studies. In this section, the limitations will be pointed out and potential improvements will be suggested. Points below are ordered by their potential impact on the results.

7.1 Choice of Atlas.

In this study we chose to use the atlas PALS-12 (Van Essen 2005) delineating the cortex in Brodmann Areas (BAs). Firstly, the methodology used to obtain this atlas is effecient, but it is based on only 12 normal young adults. Due to the high inter-subject variability of the cortex topology, it would have been preferable to have more subjects in order to derive a probabilistic mapping of cortical parcellation. Secondly, The PALS-12 atlas is based on structural T_1-w images. The choice of a more quantitative metric might have helped to improve the accuracy of the parcellation (Lutti et al. 2014; Sereno et al. 2013). Thirdly, BAs are by definition delineated by different cortical organization across cortical layers (Brodmann 1909). This method classifies the Brodmann Atlas in the cytoarchitectural atlases, which is close, but different than the myeloarchitectural atlases. Some work about the myeloarchitectural parcellation of the cortex exist in the literature (Vogt 1911; Nieuwenhuys et al. 2014) but no quantitative atlas of the full cortex is provided. A solution to fix these three limitations would be to create our own atlas of the cortical myeloarchitecture based on the CME metric computed on several subjects. The parcellation method would need to be determined. An online version of such an atlas in the MNI space as well as in the FreeSurfer space would be beneficial for the MR community.

7.2 Histological validation

Our results were compared with previous histological works performed by Braitenberg (1962). Despite a significant similarity, it would be relevant to perform *ex-vivo* histology and CME calculation in the same brain tissue (e.g. using myelin staining or CARS microscopy). Such a study would give more insight on the accuracy of the CME metric and the combination model. Also, it would help to calibrate the CME metric and thus associate an absolute myelin content value to the CME. Ultimately, a histological study conducted with *ex-vivo* MS tissue would give information on the sensitivity of CME to MS cortical lesions.

7.3 HC and MS matching

In both studies performed with MS patients, HC and MS group presented a mean age difference of 5 to 10 years. These differences are taken into account when the GLM statistics are performed. However, a linear dependence is assumed, which is not necessarily true. Having more HC and MS would firstly increase the statistical power of the group tests and secondly allow to better match the MS group.

7.4 Limitations of the surface-based analysis

All the combination framework is implemented using cortical surfaces. As seen previously, surface-based analysis (SBA) presents many advantages, for example the partial volume effect can be minimized by taking the mid-cortical surface, the surface visualisation is fast and clear, or the diffuse pathology is easy to compute and represent. However, SBA also carries some limitations. First, when surfaces are noisy, it is quite difficult to determine the source of the noise. Does it come from a misregistration, from partial volume effect or from sources images? Once sampled, it is not obvious to assess the quality of a surface. Secondly, it is difficult to visually detect small focal lesions on cortical surfaces. Indeed, surfaces are often noisy and a detailed observation is not trivial. Thirdly, a great part of MS cortical studies are not using SBA, which makes it more difficult to compare results on surface space. A relatively simple way to improve these points would be to extend the combination framework to volumetric inputs. Thus, both surface-based and volume-based results could be compute. As proposed earlier, CME computed in the volume space could be relevant to study focal cortical (and WM) lesions. The ability (sensitivity & specificity) of CME to detect focal lesions could thus be compared to others metrics. Moreover, the behaviour of CME

relatively to the various MS pathological components (demyelination, inflammation, oedema) could be assessed. The bigger challenge in computing CME in the volume space is that the high fraction of cortical voxels subject to partial volume effect could bias the result of the ICA decomposition.

7.5 The choice of an ICA-based combination

The choice of an ICA based algorithm was motivated by the good compromise between robustness, calculus time, simplicity of implementation and relevance of the concept. Similar techniques, (e.g. PCA-based) have been tested but shown as less robust and conceptually less satisfying. However, others combining techniques were not considered because of their complexity of implementation, for example non linear ICA based algorithms or Bayesian statistics. Such method could be interesting to investigate if the needs and opportunity comes.

7.6 Glial cells and MRI

Glials cells account for 72% of the cortical volume and contribute to the MRI signal. However, the impact of glial cells variation on MRI images is still vague in the literature. The emphasis is often put on the contribution of neurons and myelin rather than glia. For example, macrophages activation could potentially be responsible of a hyperintense halo on T_2* lesions (Pitt et al. 2010), but the mechanisms of such signal variations are still poorly understood. It would be of interest to better understand why does myelin is responsible for the greater part of the signal and so to understand why the signal drops or rises in demyelination areas. A possible option would be to simulate the MRI signal from a given cell composition. Challenges would be to infer the MRI signal from the chemical composition and the 3D structure of a tissue. But the great interest would be to test different hypotheses about cells interaction in lesions and thus being able to validate them by studying the actual MR signal.

7.7 P-values…

P-value is often seen as the ultimate marker of success (or fail) of a result. Indeed, it is a widely accepted practice to chose a p-value of 0.05 to test a null-hypothesis and classify the result as *"Scientifically proven"* if the observed p-value is below this threshold. However, an abusing use and misinterpretation of p-values lead to serious issues of reproducibility and replicability of

scientific conclusions, as recently reported by the American Statistical Association (ASA) (Wasserstein & Lazar 2016). An example of p-value misuse is to consider it as a measure of the probability that the studied hypothesis is true, e.g. *"the probability that random chance produced the observed data is 0.05, so my hypothesis is 95% true.*". However, p-values only indicates how incompatible the data are with a specified model, but give no information on how compatible the data are with a specified model. Moreover, using the value of a p-value to measure the size of an effect or the importance of a result is not a good practice. ASA remembers that p-values are very sensitives to outliers or noisy data: "*Any effect, no matter how tiny, can produce a small p-value if the sample size or measurement precision is high enough, and large effects may produce unimpressive p-values if the sample size is small or measurements are imprecise*". Next, the selective reporting of p-values also largely contributes to science irreproducibility. Indeed, conducting multiple analyses of the data and reporting only those with certain p-values renders the reported p-value un-interpretable. ASA warns that *"such techniques leads to suspicious excess of statically significant results in the literature and should be vigorously avoid"*. Finally, it is important to keep in mind that a p-value does not provide a good evidence regarding a model or hypothesis, and a scientific conclusion should not end based only on whether a p-value passed a threshold or not. For these reasons, some editors (e.g. those of *Basic and Applied Social Psychology*) chose to ban p-values because of constant doubts on results only validated by p-values (Trafimow & Marks 2015). Alternatives proposed by ASA are, for example, to emphasize estimation over testing, such as confidence, credibility or prediction intervals. Also, Bayesian methods or false discovery rates could be better tools to assess the size of an effect or whether an hypothesis is correct.

As seen above, statistics offers powerful tools to analyse and interpret the data; however, to maintain scientific credibility, it is important to remember that *"with great power comes great responsibility"*.

CHAPTER 8 CONCLUSION AND RECOMMENDATIONS

The goal of this work was to develop a novel approach to combine several MRI modalities sensitive to myelin in the *in-vivo* human cortex. The rationale was to extract the shared source of signal, assumed to be an indicator of myelin content. The framework developed is based on the principle of signal decomposition using minimisation of gaussianity. The gain in myelin specificity of the extracted components has been validated using simulations and previous histology works. Thereafter, the method was applied on MS patients in order to study their cortical variations of myeloarchitecture. Two groups of MS patients have been studied. A *classic* cohort and an *early* cohort (disease duration < 3years). In both cases the combined myelin maps detected significant demyelination areas in various cortical regions, better than conventional metrics.

Until now, many studies or conferences speakers have suggested the idea to combine several MR modalities, because they saw the potential benefits. However, the literature presented a lack of actual combination framework, applied to structural MR modalities. Some "tricks" already existed, such as dividing T_1-w by T2-w, but their relevance was questioned. Moreover, a more specific tool was needed to study the fine details of cortical disease progression in MS patients. Hence, this work has a double impact: improving studies related with in-vivo cortical myeloarchitecture, and suggesting a novel combination approach adaptable to various others MR modalities.

My contribution to this work is expressed by the framework development, the study of feasibility and analysis of the results. I also developed the scripts to pre-process MTR data and I conducted the analyses involving groups of MS patients. While I have been involved in subject scanning, scheduling, surfaces reconstruction and T_2* pre-processing, the greater part has been performed by collaborators.

Compromises between time, complexity and relevance had to be taken. Hence, improvements could be done on various aspects of the methodology. My recommendations, ordered by relevance, are: choosing or building an accurate atlas of the cortical myeloarchitecture, validate and calibrate CME values with histological measurements (e.g. staining or CARS microscopy), investigate the relevance of the combination in volume-based analysis, investigate the potential benefits of a bayesian approach, and be careful with the statistics.

In addition to technical improvements of the method, future work investigating the hypothetic interplay between GM and WM pathological features of MS would be of great interest. The last study I have been working on explores MS in this direction, by using tractography methods to assess the connections between cortical areas and the CNS. One of the main reasons I am excited to pursue this study is because it will give me a chance to work with a broad range of scientific topics, including diffusion MRI and graph analysis. I hope that by making my research more interdisciplinary I will be able make a significant contribution to science.

BIBLIOGRAPHY

Anderson, J.M. et al., 2008. Abnormally phosphorylated tau is associated with neuronal and axonal loss in experimental autoimmune encephalomyelitis and multiple sclerosis. *Brain: a journal of neurology*, 131(Pt 7), pp.1736–1748.

Anon, AFSEP Foundation. *Association Francaise des Sclérosé En Plaques*. Available at: www.afsep.fr.

Anon, MS Society of Canada. Available at: https://mssociety.ca/about-ms [Accessed 2016b].

Azevedo, F.A.C. et al., 2009. Equal numbers of neuronal and nonneuronal cells make the human brain an isometrically scaled-up primate brain. *The Journal of comparative neurology*, 513(5), pp.532–541.

Barbier, E.L. et al., 2002. Imaging cortical anatomy by high-resolution MR at 3.0T: detection of the stripe of Gennari in visual area 17. *Magnetic resonance in medicine: official journal of the Society of Magnetic Resonance in Medicine / Society of Magnetic Resonance in Medicine*, 48(4), pp.735–738.

Barkhof, F. & van Walderveen, M., 1999. Characterization of tissue damage in multiple sclerosis by nuclear magnetic resonance. *Philosophical transactions of the Royal Society of London. Series B, Biological sciences*, 354(1390), pp.1675–1686.

Berry, I. et al., 1999. A multicenter measurement of magnetization transfer ratio in normal white matter. *Journal of magnetic resonance imaging: JMRI*, 9(3), pp.441–446.

Bingham, E. & Hyvärinen, A., 2000. A fast fixed-point algorithm for independent component analysis of complex valued signals. *International journal of neural systems*, 10(1), pp.1–8.

Bø, L. et al., 2003. Subpial demyelination in the cerebral cortex of multiple sclerosis patients. *Journal of neuropathology and experimental neurology*, 62(7), pp.723–732.

Braitenberg, V., 1962. A note on myeloarchitectonics. *The Journal of comparative neurology*, pp.118:141–156.

Brodmann, K., 1909. *BRODMANN'S Localisation in the Cerebral Cortex* L. J. Garey, ed., Springer.

Brownell, B. & Hughes, J.T., 1962. The distribution of plaques in the cerebrum in multiple sclerosis. *Journal of neurology, neurosurgery, and psychiatry*, 25, pp.315–320.

Calabrese, M. et al., 2010. A 3-year magnetic resonance imaging study of cortical lesions in relapse-onset multiple sclerosis. *Annals of neurology*, 67(3), pp.376–383.

Calabrese, M. et al., 2009. Cortical lesions and atrophy associated with cognitive impairment in relapsing-remitting multiple sclerosis. *Archives of neurology*, 66(9), pp.1144–1150.

Chavhan, G.B. et al., 2009. Principles, techniques, and applications of T_2*-based MR imaging and its special applications. *Radiographics: a review publication of the Radiological Society of North America, Inc*, 29(5), pp.1433–1449.

Chen, J.T.-H. et al., 2013. Clinically feasible MTR is sensitive to cortical demyelination in MS. *Neurology*, 80(3), pp.246–252.

Chen, W. et al., 2014. Quantitative susceptibility mapping of multiple sclerosis lesions at various ages. *Radiology*, 271(1), pp.183–192.

Cohen-Adad, J. et al., 2011. In vivo evidence of disseminated subpial T_2* signal changes in multiple sclerosis at 7 T: a surface-based analysis. *NeuroImage*, 57(1), pp.55–62.

Cohen-Adad, J. et al., 2012. T_2* mapping and B_0 orientation-dependence at 7 T reveal cyto- and myeloarchitecture organization of the human cortex. *NeuroImage*, 60(2), pp.1006–1014.

Cohen-Adad, J., 2014. What can we learn from T_2* maps of the cortex? *NeuroImage*, 93 Pt 2, pp.189–200.

Compston, A. & Coles, A., 2008. Multiple sclerosis. *The Lancet*, 372(9648), pp.1502–1517.

Dawson, J.W., 1916. XVIII.—The Histology of Disseminated Sclerosis. *Transactions of the Royal Society of Edinburgh*, 50(03), pp.517–740.

Deistung, A. et al., 2013. Toward in vivo histology: a comparison of quantitative susceptibility mapping (QSM) with magnitude-, phase-, and R2*-imaging at ultra-high magnetic field strength. *NeuroImage*, 65, pp.299–314.

Derakhshan, M. et al., 2014. Surface-based analysis reveals regions of reduced cortical magnetization transfer ratio in patients with multiple sclerosis: a proposed method for imaging subpial demyelination. *Human brain mapping*, 35(7), pp.3402–3413.

Desikan, R.S. et al., 2006. An automated labeling system for subdividing the human cerebral cortex on MRI scans into gyral based regions of interest. *NeuroImage*, 31(3), pp.968–980.

Faria, D. de P. et al., 2014. PET imaging in multiple sclerosis. *Journal of neuroimmune pharmacology: the official journal of the Society on NeuroImmune Pharmacology*, 9(4), pp.468–482.

Fischl, B. et al., 2004. Automatically Parcellating the Human Cerebral Cortex. *Cerebral Cortex*, 14, pp.11–22.

Fukunaga, M. et al., 2010. Layer-specific variation of iron content in cerebral cortex as a source of MRI contrast. *Proceedings of the National Academy of Sciences of the United States of America*, 107(8), pp.3834–3839.

Geurts, J.J.G. et al., 2005. Cortical lesions in multiple sclerosis: combined postmortem MR imaging and histopathology. *AJNR. American journal of neuroradiology*, 26(3), pp.572–577.

Geurts, J.J.G. & Barkhof, F., 2008. Grey matter pathology in multiple sclerosis. *Lancet neurology*, 7(9), pp.841–851.

Geyer, S. et al., 2011. Microstructural Parcellation of the Human Cerebral Cortex - From Brodmann's Post-Mortem Map to in vivo Mapping with High-Field Magnetic Resonance Imaging. *Frontiers in human neuroscience*, 5, p.19.

Glasser, M.F. & Van Essen, D.C., 2011. Mapping human cortical areas in vivo based on myelin content as revealed by T_1- and T2-weighted MRI. *The Journal of neuroscience: the official journal of the Society for Neuroscience*, 31(32), pp.11597–11616.

Govindarajan, S.T. et al., 2014. Reproducibility of T2 * mapping in the human cerebral cortex in vivo at 7 tesla MRI. *Journal of magnetic resonance imaging: JMRI*. Available at: http://dx.doi.org/10.1002/jmri.24789.

de Graaf, W.L. et al., 2012. Lesion detection at seven Tesla in multiple sclerosis using magnetisation prepared 3D-FLAIR and 3D-DIR. *European radiology*, 22(1), pp.221–231.

Gray, H. & Standring, S., 2008. *Gray's anatomy: the anatomical basis of clinical practice*, Elsevier/Churchill Livingstone.

Haacke, E.M. et al., 2005. Imaging iron stores in the brain using magnetic resonance imaging. *Magnetic resonance imaging*, 23(1), pp.1–25.

Harrison, D.M. et al., 2016. Lesion Heterogeneity on High-Field Susceptibility MRI Is Associated with Multiple Sclerosis Severity. *AJNR. American journal of neuroradiology*. Available at: http://dx.doi.org/10.3174/ajnr.A4726.

Hartung, D.M. et al., 2015. The cost of multiple sclerosis drugs in the US and the pharmaceutical industry: Too big to fail? *Neurology*, 84(21), pp.2185–2192.

He, J. et al., 2001. Enhancing patterns in multiple sclerosis: evolution and persistence. *AJNR. American journal of neuroradiology*, 22(4), pp.664–669.

Henkelman, R.M., Stanisz, G.J. & Graham, S.J., 2001. Magnetization transfer in MRI: a review. *NMR in biomedicine*, 14(2), pp.57–64.

Huber, P.J., 1985. Projection Pursuit. *Annals of statistics*, 13(2), pp.435–475.

Hwang, D., Kim, D.-H. & Du, Y.P., 2010. In vivo multi-slice mapping of myelin water content using T_2* decay. *NeuroImage*, 52(1), pp.198–204.

Hyvärinen, A. & Oja, E., 2000. Independent component analysis: algorithms and applications. *Neural networks: the official journal of the International Neural Network Society*, 13(4-5), pp.411–430.

Hyvärinen, A. & Oja, E., 1999. Independent Component Analysis: A Tutorial. *Neural Networks*.

Karampampa, K. et al., 2012. TREATMENT EXPERIENCE, BURDEN, AND UNMET NEEDS (TRIBUNE) IN MULTIPLE SCLEROSIS STUDY: THE COSTS AND UTILITIES OF MS PATIENTS IN CANADA. *J Popul Ther Clin Pharmacol*, 19(1), pp.11–25.

Kebir, H. et al., 2007. Human TH17 lymphocytes promote blood-brain barrier disruption and central nervous system inflammation. *Nature medicine*, 13(10), pp.1173–1175.

Kidd, D. et al., 1999. Cortical lesions in multiple sclerosis. *Brain: a journal of neurology*, 122 (Pt 1), pp.17–26.

Klein, A. & Tourville, J., 2012. 101 labeled brain images and a consistent human cortical labeling protocol. *Frontiers in neuroscience*, 6, p.171.

Kuhlmann, T. et al., 2002. Acute axonal damage in multiple sclerosis is most extensive in early disease stages and decreases over time. *Brain: a journal of neurology*, 125(Pt 10), pp.2202–2212.

Kutzelnigg, A. et al., 2005. Cortical demyelination and diffuse white matter injury in multiple sclerosis. *Brain: a journal of neurology*, 128(Pt 11), pp.2705–2712.

Lang, H.L.E. et al., 2002. A functional and structural basis for TCR cross-reactivity in multiple sclerosis. *Nature immunology*, 3(10), pp.940–943.

Lanzilotto, M., Perciavalle, V. & Lucchetti, C., 2013. Auditory and visual systems organization in Brodmann Area 8 for gaze-shift control: where we do not see, we can hear. *Frontiers in behavioral neuroscience*, 7, p.198.

Lee, J. et al., 2011. T_2*-based fiber orientation mapping. *NeuroImage*, 57(1), pp.225–234.

Lee, J. et al., 2012. The contribution of myelin to magnetic susceptibility-weighted contrasts in high-field MRI of the brain. *NeuroImage*, 59(4), pp.3967–3975.

Levesque, I.R. & Pike, G.B., 2009. Characterizing healthy and diseased white matter using quantitative magnetization transfer and multicomponent T2 relaxometry: A unified view via a four-pool model. *Magnetic resonance in medicine: official journal of the Society of Magnetic Resonance in Medicine / Society of Magnetic Resonance in Medicine*, 62(6), pp.1487–1496.

Levin, L.I. et al., 2010. Primary infection with the Epstein-Barr virus and risk of multiple sclerosis. *Annals of neurology*, 67(6), pp.824–830.

Lhermitte, J., 1924. Les troubles psychiques dans la SEP. *Paris medical*.

Li, D., Wang, Y. & Waight, D.J., 1998. Blood oxygen saturation assessment in vivo using T_2* estimation. *Magnetic resonance in medicine: official journal of the Society of Magnetic Resonance in Medicine / Society of Magnetic Resonance in Medicine*, 39(5), pp.685–690.

Li, X. et al., 2015. Detection of demyelination in multiple sclerosis by analysis of relaxation at 7 T. *NeuroImage: Clinical*, 7, pp.709–714.

Lutti, A. et al., 2014. Using high-resolution quantitative mapping of R1 as an index of cortical myelination. *NeuroImage*, 93 Pt 2, pp.176–188.

Mainero, C. et al., 2015. A gradient in cortical pathology in multiple sclerosis by in vivo quantitative 7 T imaging. *Brain: a journal of neurology*, 138(Pt 4), pp.932–945.

Mainero, C. et al., 2009. In vivo imaging of cortical pathology in multiple sclerosis using ultra-high field MRI. *Neurology*, 73(12), pp.941–948.

Mangeat, G. et al., 2016. Association between cortical demyelination and structural connectomics in early multiple sclerosis. In *ISMRM*.

Mangeat, G. et al., 2014. Comparison between 7T T_2* and 3T MTR in the in vivo human cortex. In *ISMRM*.

Mangeat, G. et al., 2015. Multivariate combination of magnetization transfer ratio and quantitative T_2* to detect subpial demyelination in multiple sclerosis. In *ISMRM*.

Mangeat, G., Govindarajan, S.T., et al., 2015. Multivariate combination of magnetization transfer, T_2* and B_0 orientation to study the myelo-architecture of the in vivo human cortex. *NeuroImage*, 119, pp.89–102.

Mangeat, G., Louapre, C., et al., 2015. Multivariate combination of quantitative T_2* and T_1 at 7T MRI detects in vivo subpial demyelination in the early stages of MS. In *Mult Scler*. ECTRIMS. p. 485.

Marrie, R.A., 2004. Environmental risk factors in multiple sclerosis aetiology. *Lancet neurology*, 3(12), pp.709–718.

Mottershead, J.P. et al., 2003. High field MRI correlates of myelin content and axonal density in multiple sclerosis. *Journal of neurology*, 250(11), pp.1293–1301.

Nieuwenhuys, R., 2013. The myeloarchitectonic studies on the human cerebral cortex of the Vogt-Vogt school, and their significance for the interpretation of functional neuroimaging data. *Brain structure & function*, 218(2), pp.303–352.

Nieuwenhuys, R., Broere, C.A.J. & Cerliani, L., 2014. A new myeloarchitectonic map of the human neocortex based on data from the Vogt-Vogt school. *Brain structure & function*. Available at: http://dx.doi.org/10.1007/s00429-014-0806-9.

Orton, S.-M. et al., 2006. Sex ratio of multiple sclerosis in Canada: a longitudinal study. *Lancet neurology*, 5(11), pp.932–936.

Peterson, J.W. et al., 2001. Transected neurites, apoptotic neurons, and reduced inflammation in cortical multiple sclerosis lesions. *Annals of neurology*, 50(3), pp.389–400.

Pike Bruce, G., 1996. Pulsed Magnetization Transfer Contrast in Gradient Echo Imaging: Two-Pool Analytic Description of Signal Response. *Magn Reson Med*, 36, pp.95–103.

Pike, G.B., 1997. Magnetization transfer imaging of multiple sclerosis. *Italian journal of neurological sciences*, 18(6), pp.359–365.

Pitt, D. et al., 2010. Imaging Cortical Lesions in Multiple Sclerosis With Ultra–High-Field Magnetic Resonance Imaging. *Arch Neurol*, pp."812–818."

Reichenbach, J.R. et al., 2015. Quantitative Susceptibility Mapping: Concepts and Applications. *Clinical neuroradiology*, 25 Suppl 2, pp.225–230.

Roosendaal, S.D. et al., 2009. Accumulation of cortical lesions in MS: relation with cognitive impairment. *Multiple sclerosis* , 15(6), pp.708–714.

Sahraian, M.A. et al., 2010. Black holes in multiple sclerosis: definition, evolution, and clinical correlations. *Acta neurologica Scandinavica*, 122(1), pp.1–8.

Schmierer, K. et al., 2004. Magnetization transfer ratio and myelin in postmortem multiple sclerosis brain. *Annals of neurology*, 56(3), pp.407–415.

Schmierer, K. et al., 2008. Quantitative magnetic resonance of postmortem multiple sclerosis brain before and after fixation. *Magnetic resonance in medicine: official journal of the Society of Magnetic Resonance in Medicine / Society of Magnetic Resonance in Medicine*, 59(2), pp.268–277.

Schmierer, K. et al., 2007. Quantitative magnetization transfer imaging in postmortem multiple sclerosis brain. *Journal of magnetic resonance imaging: JMRI*, 26(1), pp.41–51.

Schrödinger, E., 1967. *What is Life? the Physical Aspect of the Living Cell & Mind and Matter*, University P.

Seewann, A. et al., 2011. Imaging the tip of the iceberg: visualization of cortical lesions in multiple sclerosis. *Multiple sclerosis* , 17(10), pp.1202–1210.

Seewann, A. et al., 2012. Postmortem verification of MS cortical lesion detection with 3D DIR. *Neurology*, 78(5), pp.302–308.

Sereno, M.I. et al., 2013. Mapping the human cortical surface by combining quantitative T(1) with retinotopy. *Cerebral cortex* , 23(9), pp.2261–2268.

Shu, N. et al., 2011. Diffusion tensor tractography reveals disrupted topological efficiency in white matter structural networks in multiple sclerosis. *Cerebral cortex* , 21(11), pp.2565–2577.

Spees, W.M. et al., 2001. Water Proton MR Properties of Human Blood at 1.5 Tesla: Magnetic Susceptibility, T_1, T2, T*2, and Non- Lorentzian Signal Behavior. *Magnetic resonance in medicine: official journal of the Society of Magnetic Resonance in Medicine / Society of Magnetic Resonance in Medicine*, 45, pp.533–542.

Stüber, C. et al., 2014. Myelin and iron concentration in the human brain: a quantitative study of MRI contrast. *NeuroImage*, 93 Pt 1, pp.95–106.

Tanttu, J.I. et al., 1992. Synergistic enhancement of MRI with Gd-DTPA and magnetization transfer. *Journal of computer assisted tomography*, 16(1), pp.19–24.

Tardif, C.L. et al., 2012. Quantitative magnetic resonance imaging of cortical multiple sclerosis pathology. *Multiple sclerosis international*, 2012, p.742018.

Trafimow, D. & Marks, M., 2015. Editorial. *Basic and applied social psychology*, 37(1), pp.1–2.

Trapp, B.D. et al., 1998. Axonal transection in the lesions of multiple sclerosis. *The New England journal of medicine*, 338(5), pp.278–285.

Van Essen, D.C., 2005. A Population-Average, Landmark- and Surface-based (PALS) atlas of human cerebral cortex. *NeuroImage*, 28(3), pp.635–662.

Vargas, W.S. et al., 2015. Measuring longitudinal myelin water fraction in new multiple sclerosis lesions. *NeuroImage. Clinical*, 9, pp.369–375.

Viglietta, V. et al., 2004. Loss of functional suppression by CD4+CD25+ regulatory T cells in patients with multiple sclerosis. *The Journal of experimental medicine*, 199(7), pp.971–979.

Vogt, O., 1911. Die Myeloarchitectonik des Isocortex parietalis. *Journal für Psychologie und Neurologie*, 18, pp.“379–390.”

Wang, Y. et al., 2015. Differentiation and quantification of inflammation, demyelination and axon injury or loss in multiple sclerosis. *Brain: a journal of neurology*. Available at: http://dx.doi.org/10.1093/brain/awv046.

Wasserstein, R.L. & Lazar, N.A., 2016. The ASA's statement on p-values: context, process, and purpose. *The American statistician*, 0(ja), pp.00–00.

Wegner, C. et al., 2006. Neocortical neuronal, synaptic, and glial loss in multiple sclerosis. *Neurology*, 67(6), pp.960–967.

Widmaier, E. et al., 2013. *Vander's Human Physiology: 13th Edition*, McGraw-Hill Higher Education.

Willer, C.J. et al., 2003. Twin concordance and sibling recurrence rates in multiple sclerosis. *Proceedings of the National Academy of Sciences of the United States of America*, 100(22), pp.12877–12882.

Wolff, S.D. & Balaban, R.S., 1989. Magnetization transfer contrast (MTC) and tissue water proton relaxation in vivo. *Magnetic resonance in medicine: official journal of the Society of Magnetic Resonance in Medicine / Society of Magnetic Resonance in Medicine*, 10(1), pp.135–144.

Wyllys Taylor, E., 1894. Zur pathologischen Anatomie der multiplen Sklerose. *Journal of neurology*, 5(1), pp.1–26.

Zilles, K. & Amunts, K., 2010. Centenary of Brodmann's map--conception and fate. *Nature reviews. Neuroscience*, 11(2), pp.139–145.

APPENDIX A – ARTICLE 1 SUPPLEMENTARY MATERIALS

This appendix presents the supplementary materials of the ARTICLE 1 (CHAPTER 4).

S1: Mathematical derivation of the B_0 orientation model we used.
Starting from the model presented in (Cohen-Adad et al., 2012; Lee et al., 2011):

$$R_2^* = c_0 + c_1 sin(2\theta + \phi)$$

We can split the sin function as follows:

$$R_2^* = c_0 + c_1 sin(2\theta) cos(\phi) + c_1 sin(\phi) cos(2\theta)$$

Now we can define the new fitting variables: $\alpha_1 = c_1 cos(\phi)$ and $\alpha_2 = c_1 sin(\phi)$, which are mathematically orthogonal. We can now use the following function to fit the model:
$R_2^* = c_0 + \alpha_1 sin(2\theta) + \alpha_2 cos(2\theta)$, with c_0, α_1 and α_2 the fitting parameters.

To obtain a model as a function of T_2^*:

$$T_2^* = \frac{1}{R_2^*} = \frac{1}{c_0 + \alpha_1 sin(2\theta) + \alpha_2 cos(2\theta)}$$

$$\Leftrightarrow \quad T_2^* = \frac{1}{c_0}\left[\frac{1}{1-X}\right] \text{ With } X = -\alpha_1 sin(2\theta) - \alpha_2 cos(2\theta)$$

If we keep the first order of the Taylor series, we obtain:

$$T_2^* = \frac{1}{c_0}[1 + X]O(X^2)$$

$$\Leftrightarrow \quad T_2^* \simeq \frac{1}{c_0}[1 - \alpha_1 sin(2\theta) - \alpha_2 cos(2\theta)]$$

$$\Leftrightarrow \quad T_2^* \simeq a + d\ sin(2\theta) + e\ cos(2\theta) \text{ With } a, d \text{ and } e \text{ the fitting parameters.}$$

Hence, the B_0 orientation dependency rearranged in a linear form is a sum of both terms $d\ sin(2\theta)$and $e\ cos(2\theta)$. The sum of these terms, plus the constant term of the multilinear model, are considered as a first order correction of the fibers orientation effect.

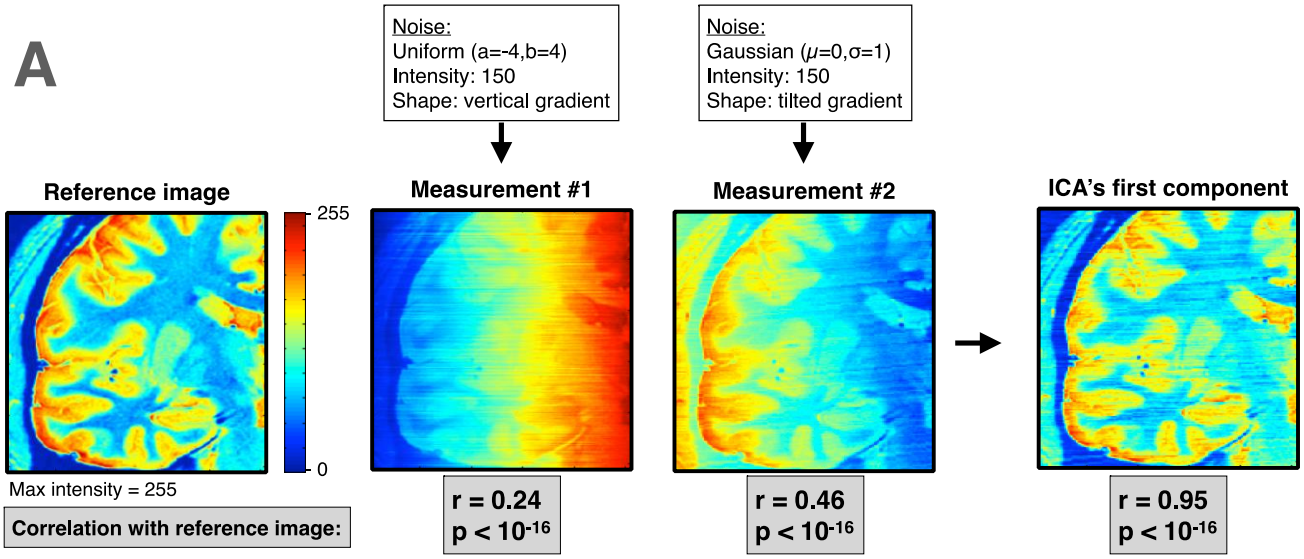

B

Noise in Mes. #1	Noise in Mes. #2	Corr. Mes.#1 vs Ref.	Corr. Mes.#1 vs Ref.	Corr. ICA. vs Ref.
Gaussian (μ=0,σ=1) Intensity: 100 Shape: vertical gradient	Gaussian (μ=0,σ=2) Intensity: 100 Shape: vertical gradient	**r = 0.36 p < 10**	**r = 0.36 p < 10**	**r = 0.61 p < 10**
Uniform (a=-4,b=4) Intensity: 150 Shape: tilted gradient	Uniform (a=-4,b=4) Intensity: 150 Shape: horizontal gradient	**r = 0.46 p < 10**	**r = 0.57 p < 10**	**r = 0.76 p < 10**
Gaussian (μ=0,σ=1) Intensity: 50 Shape: random	Gaussian (μ=0,σ=1) Intensity: 50 Shape: random	**r = 0.72 p < 10**	**r = 0.72 p < 10**	**r = 0.83 p < 10**
Gaussian (μ=0,σ=70) Intensity: 1 Shape: random	Gaussian (μ=0,σ=90) Intensity: 1 Shape: random	**r = 0.60 p < 10**	**r = 0.50 p < 10**	**r = 0.68 p < 10**
Poisson (λ=2) Intensity: 50 Shape: random	Poisson (λ=2) Intensity: 50 Shape: random	**r = 0.59 p < 10**	**r = 0.59 p < 10**	**r = 0.73 p < 10**

Mes. = Measurement; Ref. = Reference Image; ICA. = ICA's first component

S2 is a proof-of-concept of "shared information extraction" using an ICA. The goal is to extract the common information contained in two (or more) images, called here "Measurement". A measurement represent an actual metric that we may want to use in order to measure a physical entity (For example, we may want to acquire an MTR image in order to study the myelin content of the brain). A measurement is a combination of our physical entity and confounding factors (which can be physiological and/or due to the measurement device). Here, we started from a reference image (ground truth) and we added different distributions, intensity and shapes of noise in order to simulate different potential measurements. Then, we used an ICA algorithm in order to extract the shared information between both measurement, and then plot the final estimation of the reference image. We finally assessed the improvement by comparing the correlation between the ICA's result and the actual reference image and the correlation between the measurements and the reference image.

(A) shows an example of simulated measurements, made from the reference image and two different noise distribution; and the result of the ICA's estimation. **(B)** shows the improvement if the ICA's estimation for different types of noise distribution added to the measurements. Each experiment has been repeated 10,000 times.

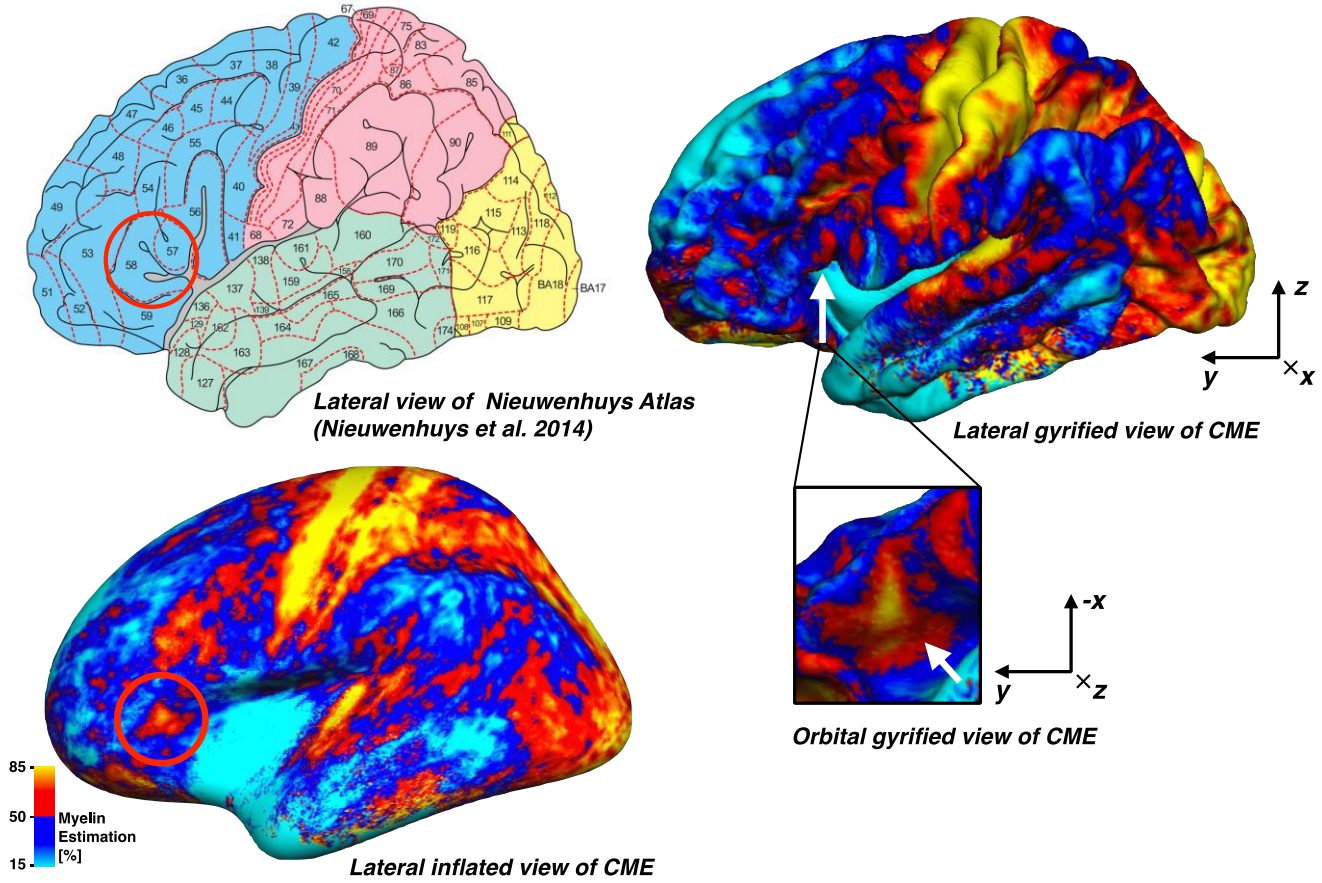

S3. Lateral view of the the myeloarchitectonic atlas of Nieuwenhuys et al. (Nieuwenhuys et al. 2014), as well as a lateral inflated and gyrified views of the mean CME map (left hemisphere).

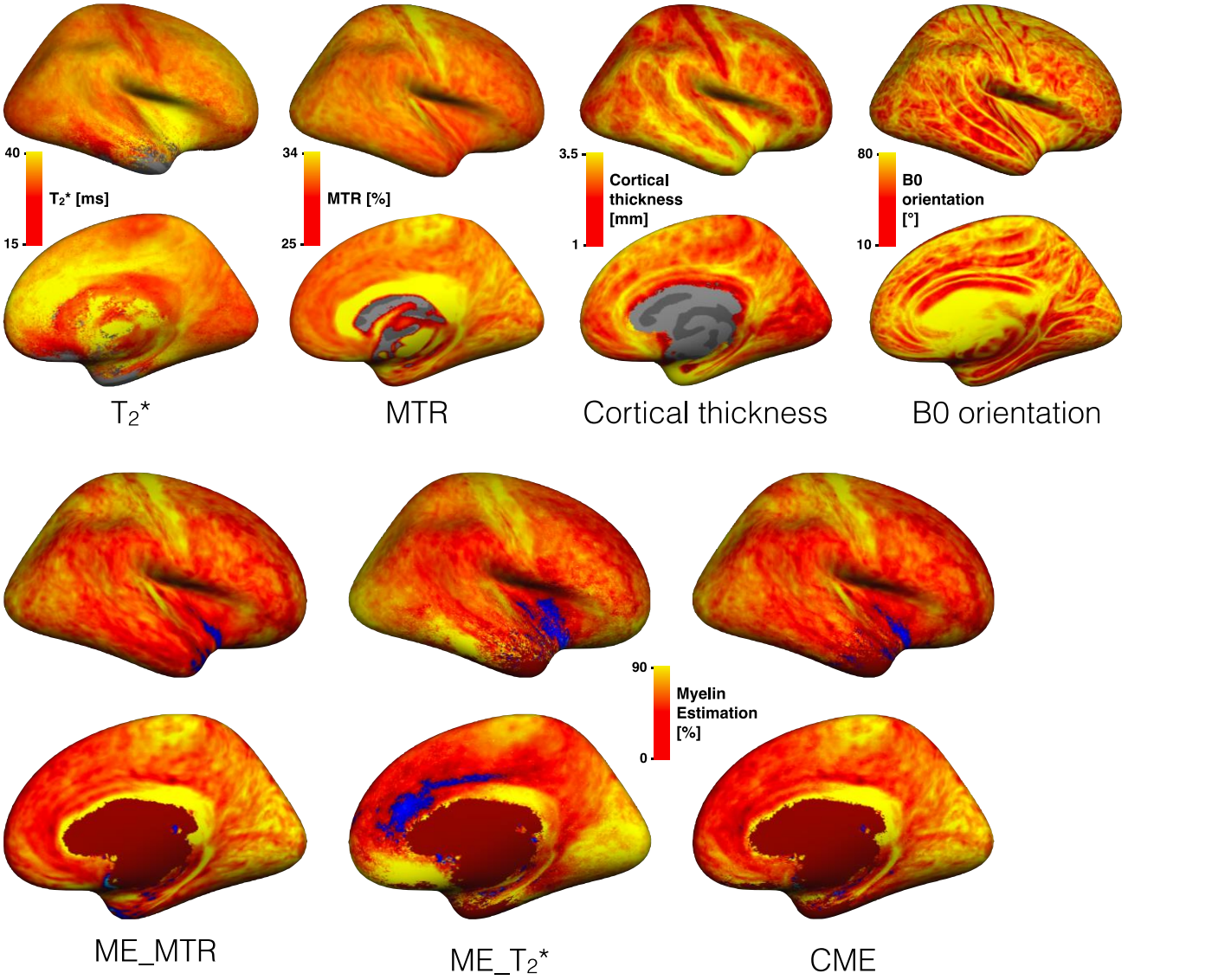

S4. Inflated medial and lateral view of T_2*, MTR, Cortical thickness, B_0 orientation, ME_MTR, ME_T_2* and CME maps plotted with a linear colormap. No positive threshold was applied. The blue color corresponds to negative values (i.e., extreme values that go beyond the range that was applied to normalize myelin values).

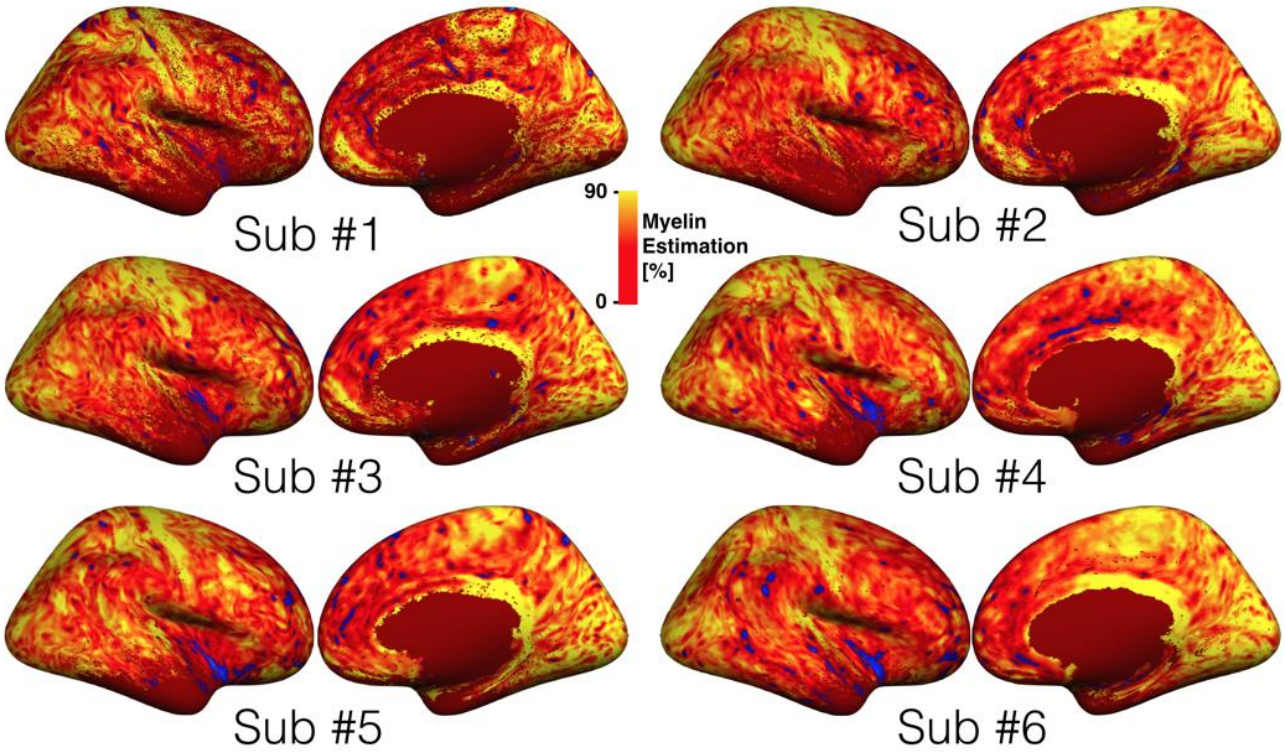

S5. Individual subject CME maps, plotted with a linear colormap in medial and lateral views. No positive threshold was applied. The blue color corresponds to negative values (i.e., extreme values that go beyond the range that was applied to normalize myelin values).